Chem Soc Rev

REVIEW ARTICLE

View Article Online
View Journal | View Issue

Cite this: *Chem. Soc. Rev.*, 2021, **50**, 3178

Insights into the deposition chemistry of Li ions in nonaqueous electrolyte for stable Li anodes

Zhenxing Wang,†[ab] Zhenhua Sun,†[ab] Juan Li,[ac] Ying Shi,[ab] Chengguo Sun,[d] Baigang An,[d] Hui-Ming Cheng[ae] and Feng Li*[ab]

Lithium (Li) is the lightest and most electronegative metallic element and has been considered the ultimate anode choice for energy storage systems with high energy density. However, uncontrollable dendrite formation caused by high ion transfer resistance and low Li atom diffusion, and dendrite growth with large volume expansion and high electronegative activity, result in severe safety concerns and poor coulombic efficiency. In this review, the latest progress is presented from the viewpoint of dendrite evolution (from dendrite formation to growth) as the main line to understand the factors that influence the deposition chemistry. For the dendrite formation, specific attention is focused on the four distinct but interdependent factors: (a) how the dielectric constant, donor number, viscosity and salt concentration affect the movement of solvated Li^+ in nonaqueous electrolyte. (b) The effect of non-polar solvents and anions with polar groups or high concentration on the Li^+ desolvation step. (c) The effect of the formation of solid electrolyte interphase (SEI), along with its specific adsorption and solvated structure, and its physical structure, chemical composition and growth thickness on Li^+ diffusion. (d) The effect of the diffusion coefficient of the host material on Li atom migration. After dendrite formation, the attention is focused on two detrimental factors together with dendrite growth: (e) low coulombic efficiency; (f) large volume expansion. Correspondingly, the emphasis is placed on reducing the side reactions and minimizing the volume expansion. Conclusions and perspectives on the current limitations and future research directions are recommended. It is anticipated that the dynamic dendrite evolution can provide fresh insight into similar electrochemical reaction processes of other anode chemistries in nonaqueous electrolytes, ranging from a conversion-reaction metal anode (Li, Na, Al) and an alloying anode ($LiAl_x$, $NaAl_x$) to an intercalation-based anode (graphite, TiS_2), as well as aqueous, ionic liquid and flow redox battery systems.

Received 27th September 2020

DOI: 10.1039/d0cs01017k

rsc.li/chem-soc-rev

1. Introduction

Since the successful commercialization of lithium-ion batteries (LIBs) with lithium cobalt oxide ($LiCoO_2$) cathode and carbon anode by the Sony company in 1991, LIBs in portable electronics have greatly reshaped our life.[1] To recognize their significant contributions to the development of LIBs, the 2019 Nobel Prize in Chemistry was awarded to John B. Goodenough, M. Stanley Whittingham, and Akira Yoshino.[2] However, with increasing demands for high-capacity energy storage to support personal electronics, new devices such as unmanned aerial vehicles and the commercialization of electric vehicles, rocking-chair LIBs based on intercalation mechanism are approaching their fundamental limits.[3,4] Taking the intercalation reaction of $LiCoO_2\|$ graphite as an example, the average discharge voltage is 3.7 V (*vs.* Li^+/Li). Based on eqn (1):

$$C = F \times n \times \frac{1}{3.6M} \quad (1)$$

the theoretical capacities of graphite and $LiCoO_2$ are calculated to be 372 mA h g^{-1} and 137 mA h g^{-1} ($Li_{0.5}CoO_2$), where F is the Faraday constant, n is the charge number, M is the relative molar mass and C is the theoretical capacity. To compensate for the consumed anode during solid electrolyte interphase (SEI)

[a] *Shenyang National Laboratory for Materials Science, Institute of Metal Research, Chinese Academy of Sciences, Shenyang 110016, China. E-mail: fli@imr.ac.cn*
[b] *School of Materials Science and Engineering, University of Science and Technology of China, Shenyang 110016, China*
[c] *College of Physics, Jilin University, Changchun 130012, China*
[d] *School of Chemical Engineering, University of Science and Technology Liaoning, Anshan 114051, China*
[e] *Shenzhen Geim Graphene Center, Tsinghua-Berkeley Shenzhen Institute, Tsinghua University, Shenzhen 518055, China*
† These authors contributed equally to this work.

formation and avoid Li dendrite formation, the mass ratio of anode to cathode is normally set as 1.1 : 1.[5,6] When the weights of the separator, electrolyte and packaging materials are negligible, the energy density of a $LiCoO_2$‖graphite system is about 370 W h kg^{-1}, far below the value needed to meet the requirements of electric vehicles 500 W h kg^{-1}.[7,8] To overcome this problem, Li metal, with the highest theoretical specific capacity (3860 mA h g^{-1}) and the lowest electrochemical potential (−3.04 V *vs.* standard hydrogen electrode), has been considered the ultimate anode choice, giving an energy density of about 536 W h kg^{-1} in a $LiCoO_2$‖Li system.[9]

Notably, due to the most electronegative nature, the aqueous solvent is unstable with Li because of the active protons.[10] Since the 1950s, nonaqueous solvents, with the formation of the passivation layer to avoid the sustained reactions between Li and the electrolyte, have become the main medium in Li metal batteries.[11] However, due to its uncontrollable Li dendrite electrodeposition, it not only gives rise to poor Li coulombic efficiency (CE), but the dendrites pierce the separator and cause short-circuiting of the cells with associated safety concerns.[12] In contrast to other high-redox-potential metals, Li has the lowest electrochemical potential among all the electrode materials. Owing to this intrinsic feature, Li is inevitable to react with all polar-aprotic solvents and salt anions to form an electronically insulating but ionically conductive SEI film. Such SEI is usually not chemically stable or mechanically strong enough to prevent parasitic reactions between Li and electrolyte, resulting in an

Zhenxing Wang

Zhenxing Wang is currently a PhD student at the Institute of Metal Research, Chinese Academy of Sciences. He obtained his BS (2015) in Materials Science and Engineering from Jilin University in China. His research is focused on rational design of fluorinated interface for stable lithium metal anodes.

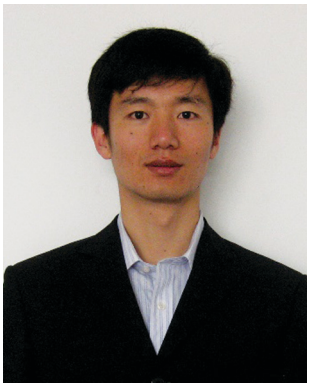

Zhenhua Sun

Dr Zhenhua Sun received his BS and PhD degrees in inorganic chemistry from Jilin University in 2001 and 2006, respectively. Then he was a Postdoctoral Research Fellow in the Chinese University of Hong Kong from 2007 to 2009. He is currently a professor at Institute of Metal Research, Chinese Academy of Sciences. His current research interests mainly focused on the synthesis and application of nano-carbon materials and carbon-based composite materials for electrochemical energy storage. He has published more than 80 papers in peer-reviewing journals including Nature Communications, Advanced Materials, etc. with 5500 citations (H-index 35).

Hui-Ming Cheng

Dr Hui-Ming Cheng is Professor and Director of both Advanced Carbon Research Division of Shenyang National Laboratory for Materials Science, Institute of Metal Research, Chinese Academy of Sciences, and the Low-Dimensional Material and Device Laboratory of the Tsinghua-Berkeley Shenzhen Institute, Tsinghua University. His research activities focus on carbon nanotubes, graphene, other 2D materials, energy storage materials, photocatalytic semiconducting materials, and bulk carbon materials. He is recognized as a Highly Cited Researcher in both materials science and chemistry fields by Thomson Reuters. He is the founding Editor-in-Chief of Energy Storage Materials and the Associate Editor of Science China Materials.

Feng Li

Dr Feng Li is a professor in Institute of Metal Research, Chinese Academy of Sciences (IMR, CAS). He received his PhD in materials science at IMR, CAS. He mainly works on nanomaterials for energy applications, such as for lithium ion batteries, lithium–sulfur batteries and electrochemical capacitors. He has published more 250 papers on peer-reviewed journals, such as Energy & Environmental Science, Adv. Mater., etc. with more 30 000 citations and H-index about 80. He obtained the award of National Science Fund for Distinguished Young Scholars by National Foundation of Science, China and Highly Cited Researcher at Materials and Chemistry by Clarivate Analytics.

excessive consumption of active material and electrolyte, subsequently draining the electrolyte and invalidating the battery. After repeated cycling, a thick SEI with large interfacial resistance forms and may totally block the ion transport with broken circuit. The irreversible Li depletion also brings about low CE and gives rise to an obstacle for practical application of Li anode. In addition, different with the intercalated electrode with controllable volume expansion (10% for graphite and 400% for Si),[13] the direct Li plating/stripping without matrix induces virtually infinite volume expansion. From a practical perspective, the areal capacity of a single-sided commercial electrode needs to reach 4 mA h cm^{-2}, equivalent to a volume expansion about 20 μm. Along with the dendrite growth, the large volume expansion easily fractures the SEI and exposes fresh Li to the electrolyte. This process occurs over and over again during the dendrite growth, and induces non-uniform SEI film for dendrite formation in advance of Sand's time.

Extensive efforts have been devoted to investigating the Li formation behavior, reducing the side reactions and suppressing the large volume expansion.[14–17] It is demonstrated that the dendrite formation can be suppressed by facilitating Li^+ diffusion and Li atom migration in bulk base, reducing the concentration gradient and homogenizing the composition of SEI. To prevent the dendrite growth, three-dimensional (3D) host with controllable volume change is developed to ensure safe cycling of Li metal batteries. Since the reviving of Li metal anode in nonaqueous electrolyte, there are a number of reviews summarizing the knowledge from various perspectives. Because Li contacts directly with the nonaqueous electrolyte during the operation, attention has always been focused on the Li electrode architecture, the interface between Li and electrolyte, the advancements of electrolyte, the characterization techniques, and the comprehensive reviews covering the above contents. However, the dynamic dendrite evolution (dendrite formation to growth) from Li^+ to Li atom, as the core factor to determine the final deposition morphology, anode CE and volume expansion, has not been systematically discussed as the main line in any dedicated reviews.

Therefore, this review places the emphasis on the dendrite evolution (from dendrite formation to growth), including the progress on the regulation of Li deposition kinetics, such as liquid-state diffusion-limited kinetics, solid-state diffusion-limited kinetics and bulk Li atom migration kinetics for suppressing dendrite formation, and the efforts on minimizing the side reactions and suppressing volume expansion for dense dendrite growth. Before being reduced to Li atom, Li^+ has to go through five steps in nonaqueous electrolyte: (1) the Li^+ solvation sheath moves from the electrolyte to the SEI/electrolyte interface; (2) Li^+ sheds the solvation sheath at the SEI/electrolyte interface; (3) Li^+ diffuses through the SEI film; (4) subsequent Li plating ($Li^+ + e^- = Li$); (5) Li atom migrates in the bulk base. During Li deposition, when the diffusion rate of Li^+ ions or atoms cannot keep up with the depletion rate (the fourth step: $Li^+ + e^- = Li$), the scarcity of Li^+ under the SEI induces fast dendritic formation. In this regard, the first three steps and the last step are the rate-determining steps during dendrite formation.[18,19] After dendrite formation, the attention is focused on two detrimental factors together with dendrite growth: (1) side reactions between Li and electrolyte, resulting in high overpotential and low CE. Correspondingly, the emphasis is placed on minimizing the side reactions by manipulation of the structure stability (electrolyte-derived SEI) and mechanical strength (artificial SEI) of SEI. (2) Large volume expansion as the increased deposition capacity during repeated cycling, resulting in safety concerns. Accordingly, the key points are focused on minimizing the volume expansion by 3D host with controllable structure. In the stripping process, Li atoms go through the reverse steps to become solvated Li^+ ions. In the last section, we will highlight the promising strategies proposed during the past few years so as to outline current trends and future perspectives in this field, which not only deepen the understanding of the dynamic dendrite evolution in this field, but propel significant breakthroughs in developing state-of-the-art electrochemical processes for the nonaqueous anode chemistries.

2. Mechanisms of dendrite formation and growth

2.1 Dendrite formation

For the present, several modes have been proposed to describe the dendrite formation, including space charge model, SEI-induced nucleating model and surface nucleating and diffusion model.

2.1.1 Space charge model. The Chazalviel model is the most widely accepted theory to describe the dendrite formation.[20] It is demonstrated that the ramified dendrite formation is a direct consequence of the space charge layer in dilute solutions. For metal anode at high charge rates in nonaqueous electrolytes, the cations are rapidly consumed and their concentration in the vicinity of the electrode drops to zero at time τ_s. Subsequently, the strong negative electric field electro-adsorbs and electroplates large number of cations in a short time, resulting in dendrite formation. This behavior is known as Sand's behavior and τ_s is called Sand's time:[12]

$$\tau_s = \pi D\left(\frac{Ce}{2Jt}\right)^2 \quad (2)$$

where t is the transport number for anions and e is the elementary positive charge, C is the initial cation concentration, J is the applied current density, D is the ambipolar diffusion coefficient $D = (\mu_a D_c + \mu_c D_a)/(\mu_a + \mu_c)$, where D_c and D_a are cation and anion diffusion coefficients, and μ_a and μ_c are anion and cation mobilities. The Sand's equation provides a quantitative method to estimate the dendrite formation time and indicates that the time is proportional to J^{-2}.

Sand's equation has been well predicted the Cu electrodeposition in an aqueous electrolyte, which dendrite growth is controlled by the long-range diffusion-limited process.[21] For the Li anode, based on the boundary condition as the change of distance L between two electrodes, the critical current density J_{lim} can be calculated:

$$J_{lim} = \frac{2eCD}{tL} \quad (3)$$

In the case of applied current density $J > J_{lim}$, the Li^+ concentration in the vicinity of the negative electrode drops to zero at Sand's time, which results in local space charge accompanying with a large electric field. After Sand' time, the dendrite starts to form and grow quickly. When the applied current density $J < J_{lim}$, the Li^+ concentration near the negative electrode does not go to zero, but remains the value close to the initial concentration. Below this current density J_{lim}, the dendrite will not form. The direct *in situ* observation of Li dendritic deposition has been performed in symmetrical Li‖Li cells using polymer electrolyte of polyethylene oxide (PEO)–lithium bistrifluoromethanesulfonimide (LiTFSI).[22] In this experiment, the initial salt concentration is 6×10^{20} cm^{-3}, the anionic transport number t is 0.8, the Li^+ diffusion constant D is 9×10^{-8} cm^2 s^{-1}, the distance L is 1.2 mm, the J_{lim} is calculated about 0.18 mA cm^{-2}. Nevertheless, the real distance of cathode to anode in cell is about 100 μm, the J_{lim} is calculated to be about 2.16 mA cm^{-2}. However, under the circumstances of current density below 2 mA cm^{-2}, the dendrite is still observed.[23] Considering the high surface area of the dendritic Li, the true areal current density is even lower than the applied one, and may never lead to dendritic Li deposition. This phenomenon indicates that some uncertain causes are neglected, except the influencing factor of diffusion-limited mechanism.

2.1.2 SEI-induced nucleating model. Compared with Cu metal electrode without SEI film during deposition, it can be inferred that the interfacial chemistry of Li has not been taken into consideration. Li metal, with the lowest electrochemical potential of −3.04 V *vs.* standard hydrogen electrode, is inevitable to react with all polar-aprotic solvents and salt anions to form an electronically insulating but ionically conductive SEI film. Due to the high ionic conductivity and electrical conductivity, the SEI is produced prior to Li metal nucleation.[24] After SEI formation, the Li deposition process is triggered, accompanying with limited short-range solid-state transport through the SEI film, rather than long-range liquid-state diffusion. Notably, the volume expansion always accompanies the increased deposition time or capacity. Owing to the fragile and brittle features, the SEI film is not chemically stable or mechanically strong enough to prevent the Li dendrite growth. Along with the dendrite growth, the large volume expansion easily fractures the SEI and exposes fresh Li to the electrolyte. This process occurs over and over again during the dendrite growth, and induces non-uniform SEI film for dendrite formation in advance of Sand's time. Since Li^+ has to diffuse across the thickening SEI before transforming to Li atom, the SEI resistance plays a great role in determining the deposition morphology by the deposition overpotential. At the initial Li deposition with small overpotential, the thin SEI with rapid Li^+ diffusion renders surface growth pattern with macroscopically compact morphology. The Li deposits growth with no preferential direction. As the polarization increases as the formation of thicker SEI, Li^+ diffusion in the SEI becomes the rate-determining step during Li deposition. As a result, Li deposits grow in length rather than in diameter, resulting in the dendrite formation.

This model is verified by ramified moss-like deposits at an extreme low current density of 10 μA cm^{-2}, indicating that

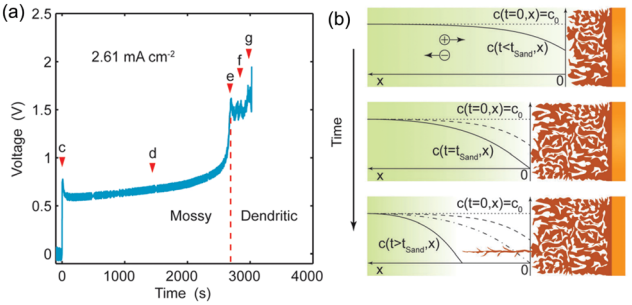

Fig. 1 (a) Voltage responses of the capillary cell at deposition current density of 2.61 mA cm^{-2}. (b) Theoretical interpretation of the growth mechanisms of Li electrodeposition during concentration polarization. Reproduced with permission from ref. 25. Copyright 2016. The Royal Society of Chemistry.

there is a morphology transition.[26] The mossy-like morphology has proved to be difficult to penetrate through the separator, contrast to the dendritic Li that easily penetrates the separator and induces safety issues. To uncover the mysterious interaction between mossy and dendritic Li with the applied current density, the electrolyte 1 M lithium hexafluorophosphate ($LiPF_6$)–ethylene carbonate (EC)/dimethyl carbonate (DMC) (1 : 1 by volume) is conducted in capillary cell.[25] The result reveals that the relatively dense mossy Li growth is reaction-limited and changes to fractal dendritic Li in the case of diffusion limitation. Under the current density of 2.61 mA cm^{-2}, the Sand's time is about 2700 s and changes from mossy to dendritic Li (Fig. 1a). The differences in the deposited morphology indicates a transition from reaction-limited to diffusion-limited growth. In the early stages of electrodeposition at 1 mA cm^{-2}, the mossy-like Li composed of whiskers firstly grows, which is typical of reaction-limited deposition. After increasing the deposited time or deposited capacity, the mossy Li changes to dendritic pattern (Fig. 1b). However, the capillary cell is distinctly different from the normal coin or pouch cell, the absolute current density is different. In addition, the *in situ* images are captured by optical microscope with low resolution and easily miss the early dendrite formation. An *in situ* solid open cell in cryogenic transmission electron microscopy (cryo-TEM) is set up to capture the formation behavior of Li whisker.[27] It is found that sluggish surface ion transport is the main reason for dendritic formation. From the onset of nucleation, Li deposition starts with the formation of faceted Li particle of (110). This observation is ascribed to the lowest surface energy compared to other low-index surfaces of body-centered cubic structure. Based on the volume of Li particle, the deposition current is estimated to be about 10–30 mA cm^{-2} at the nucleation stage. Subsequently, the whisker sprouts out of the interface between the solid electrolyte and Li particle, forms whisker with the face of (112), which is one of the major crystallographic orientations of Li dendrite.[28] This deposited behavior is ascribed to the kinetically sluggish Li transport during the dendrite growth.

The initial fast deposition of Li particle depends on the diffusion rate of Li atom within the particle and the mass

transport by the SEI film. Since this SEI becomes thick and sluggish for transporting Li^+, Li^+ is preferentially reduced and locally deposited at the Li particle–SEI interface, leading to the sprouting of Li whisker. To further capture the initial stage of Li deposition, cryo-TEM is used to reveal the evolving nanostructure deposited at low current density of 0.1 mA cm^{-2}.[29] It is found that the disorder–order phase transition is the origin of dendrite formation. Most of the Li metals grown at 0.1 mA cm^{-2} have moss-like morphology and the planar size can be as large as several micrometers with amorphous state. In contrast, partially and highly crystalline of deposited Li is observed at 0.5 mA cm^{-2} and 2.5 mA cm^{-2}. The amorphous nucleation avoids epitaxial growth and enables 3D growth into large grains. Based on the present results, in the case of current density >0.1 mA cm^{-2}, the kinetics of liquid-limited (mass transfer kinetics) and solid-limited kinetics (Li^+ diffusion through SEI) are insufficient to keep pace with the reduction of Li^+ and results in dendrite formation.

2.1.3 Surface nucleating and diffusion model. In contrast to Mg that is preferable for dendrite-free morphology, Li metal easily grows dendritic shape based on thermodynamics. Definitely analyzing the difference between Li and Mg, it is found that Mg has a higher free energy difference between low-dimensional and high-dimensional phases than Li. With a comparative study of Li and Mg metal anode, the surface diffusion on Mg electrode is significantly more rapid than Li, suggesting that Mg^{2+} has a higher tendency to deposit on nearby sites rather than on lumped areas to form dendrites.[30] The diffusion coefficient of Mg atom in bulk Mg metal is around 10^{-8}–10^{-9} cm^2 s^{-1}, which is faster than that of Li atom in bulk Li metal (5.7×10^{-11} cm^2 s^{-1}).[31,32] The bulk diffusion can bring some fresh viewpoints to understand the Li electrochemical deposition and search for an effective strategy to suppress dendrite formation.

2.2 Dendrite growth

Compared to the challenging dendrite formation, the dendrite growth is more complex for the applications of Li metal batteries. It is generally accepted that large current density and long charge duration facilitate the dendrite growth. Over the repeated cycles, various kinds of morphologies, such as needle-like, whisker-like or branch-like structures, are formed with several to tens of mircometers.[33–35] These dendrites can pierce through the separator and induce short-circuiting of working battery. Such short-circuiting brings about thermal runaway and even causes spontaneous combustion or explosion. In addition, the spiny dendrite structures possess large specific surface areas and forwardly increase the side reactions between Li and electrolyte, accompanying with low CE. The side reactions consume the active Li/electrolyte and result in thick SEI layer with large ion diffusion resistance, which may give rise to broken circuit to totally block the ion diffusion. The severe reactions also drain the electrolyte and invalidate the battery. Volume expansion is another troublesome problem during dendrite growth. Different from the intercalated electrode with controllable volume expansion (10% for graphite and 400% for Si),[13] the direct Li plating/stripping without matrix induces

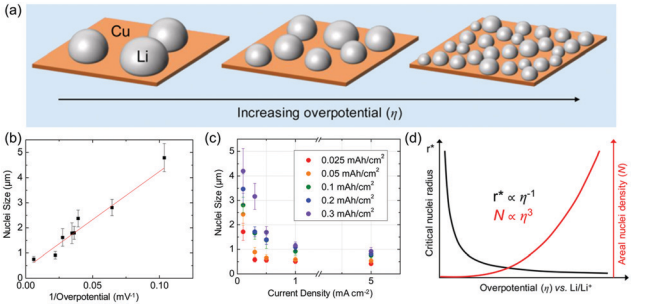

Fig. 2 (a) Schematic of the size and density of Li nuclei deposited on Cu at varying overpotentials. (b) Plot of Li particle size *versus* inverse overpotential of Li deposition. (c) Plot of Li particle *versus* applied areal current density for different amounts of Li deposition. (d) Schematic plot of the dependence of critical Li nuclei radius and areal nuclei density on the overpotential of Li deposition. Reproduced with permission from ref. 15. Copyright 2017, American Chemical Society.

virtually infinite volume expansion. From a practical perspective, the areal capacity of a single-sided commercial electrode needs to reach 4 mA h cm^{-2}, equivalent to a volume expansion about 20 μm. After repeated plating/stripping cycles, a large amount of porous deposits forms and induce additional volume expansion. Such large volume fluctuation can result in tremendous internal stress and trigger the fracture of SEI. Therefore, a fundamental understanding of dense dendrite growth, along with deposition morphology, low CE and volume expansion, is significant for the practical applications of Li metal batteries.

The classical grain growth theory works well on describing the change of grain size as the temperature varies. For electrodeposition, the growth size is highly dependent on the growth overpotential (Fig. 2a). Compared to Li deposited in carbonate-based electrolytes that are typically filamentary or wire-like and difficult to characterize, the Li growth particles in 1 M LiTFSI 1,3-dioxolane/1,2-dimethoxyethane (DOL/DME, 1 : 1 by volume) + 1 wt% $LiNO_3$ are uniform. Therefore, the interactions between the particle size and overpotential are investigated in DOL/DME electrolyte. The Li particles are measured for each combination of deposition capacity and current density. A linear relation appears when the particle size is plotted *versus* the inverse overpotential and inverse applied current density, indicating that low current density or low overpotential is beneficial for dense Li deposition (Fig. 2b and c). At low overpotential, the Li particles are sparsely spread out on the working electrode surface and expanded to form more densely packed arrangement as the increased deposition capacity, forming an island-like morphology. The particle density of Li particles is further measured with various amounts of deposition capacity. It is found that the number density of particle is proportional to the cubic power of overpotential (Fig. 2d). Based on this result, dense dendrite growth can be controlled by reducing the growth overpotential.

3. Suppression of dendrite formation

In general, it is widely accepted that high current density will give rise to accelerated dendrite formation. However, a distinct self-heating regime for dendrite evolution is proposed that

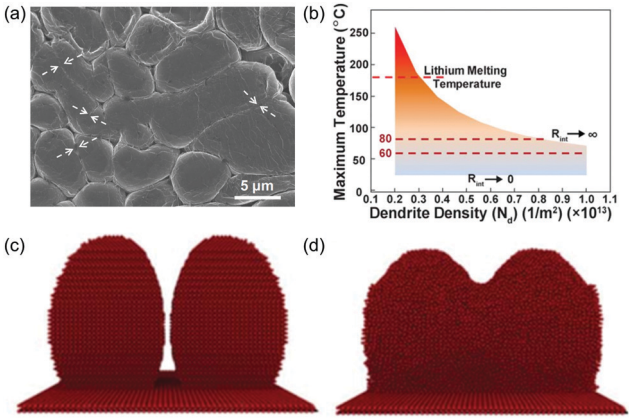

Fig. 3 (a) *Ex situ* SEM image of fusing dendrites at current density of 15 mA cm^{-2}. (b) For the typical range of interfacial thermal resistances, dendrite temperatures in the range of 60–80 °C are predicted. Screenshots of molecular modes in the (c) initial state and (d) 50 ps at 80 °C. Reproduced with permission from ref. 36. Copyright 2018, Science Publishing Group.

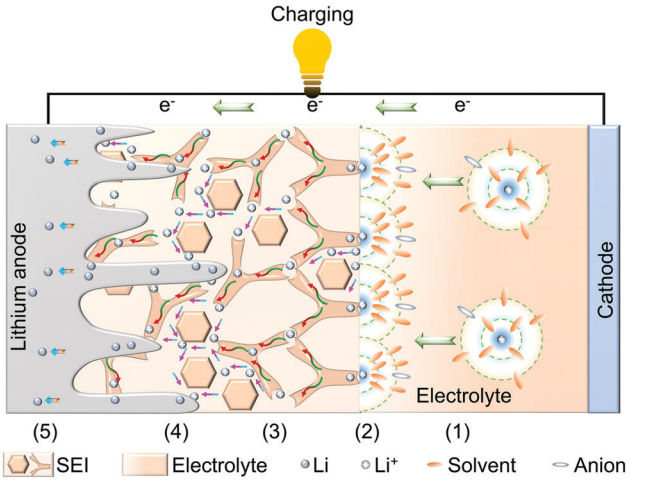

Fig. 4 Illustration of the Li deposition process from solvated Li^+ ions to Li atoms. (I) Movement of solvated Li^+ in the electrolyte. (II) Break up the Li^+ solvation sheath. (III) Li^+ ions diffuse through the SEI film. (IV) Li plating ($Li^+ + e^- = Li$). (V) Li atoms migrate in bulk base.

contradicts conventional cognition.[36] For the diffusion-limited mechanism, the surface diffusion of Li^+ is the essential for the dendrite formation. When the plating/stripping current density is improved above 9 mA cm^{-2}, the Joule heat generated by the electric current can trigger extensive surface diffusion of Li. The surface diffusion of Li is heavily temperature-dependent and increases quickly when the temperature is beyond 40 °C. Such extensive surface diffusion of Li enables closely packed dendrite particles (Fig. 3a). In addition, the electrochemical overpotential increases with the applied current density. The high overpotential can reduce the particle radius, increase the nucleation rate and nucleation density. The heat transfer simulations show that the melting point of Li (180.5 °C) can be decreased to 60 °C when the dendrite density reaches to 10^{13} m^{-2} (Fig. 3b). The Joule heat, high dendrite density and low particle size jointly merge and fuse the dendrite particle, resulting in a relatively smooth (film-like) morphology without dendritic features (Fig. 3c and d). As a matter of fact, these two theories are not contradictory. For dendrite formation at low current density, the diffusion-limited factors cannot keep up with the Li deposition rate, inducing dendrite formation. As the current density reaches 9 mA cm^{-2}, the generated Joule heat fuses the formed dendrite and merges the Li together with a smooth shape. However, such high current density will result in much more small dendrite particles with high surface areas, inducing low CE. To simultaneously address the dendrite formation and low CE, most of present work focuses on regulating the Li deposition chemistry at low current density, rather than the high current density >9 mA cm^{-2}. In consideration of this, the emphasis in this review is placed on the present strategies that regulates the Li deposition kinetics at low current density.

Based on the models of dendrite formation (Section 2.1, space charge model, SEI-induced nucleating model and surface nucleating and diffusion model), the Li deposition kinetics are crucial for suppressing dendrite formation at low current density (<9 mA cm^{-2}). Before being reduced to Li atoms, Li^+ ions have to go through five steps in nonaqueous electrolyte (Fig. 4): (I) the Li^+ solvation sheath moves from the electrolyte to the SEI/electrolyte interface; (II) Li^+ sheds the solvation sheath at the SEI/electrolyte interface; (III) Li^+ diffuses through the SEI film; (IV) subsequent Li plating ($Li^+ + e^- = Li$); (V) Li atom migrates in the bulk base. During Li deposition, when the diffusion rate of Li^+ ions or atoms cannot keep up with the depletion rate (the fourth step: $Li^+ + e^- = Li$), the scarcity of Li^+ under the SEI induces fast dendritic formation. In this regard, the first three steps and the last step are the rate-determining steps during Li nucleation.[18,19] For suppressing the dendrite formation, the deposition kinetics are taken as the main line to summarize recent progress and highlight the Li^+ solvation sheath chemistry associated with the Li^+ desolvation energy barriers, formation of SEI film, as well as Li^+ ions across the interface.

3.1 Movement of solvated Li^+ in the electrolyte

Based on the Chazalvier model,[20] the dendrite formation is determined by the mass transfer kinetics, which include the migration caused by the electric field, diffusion caused by the concentration gradient, and the convection in the electrolyte. In view of the slow convection rate in the vicinity of electrode, the effect of convection is neglected in this model. Hence, the diffusion caused by the concentration gradient and migration by the electric field are the main contributors for ion transport in the vicinity of electrode. On account of limited boundary conditions that the Li^+ concentration decreases to zero in the vicinity of the negative electrode, the diffusion caused by the concentration gradient is heavily related to the initial concentration C and Li^+ diffusion coefficient D. In general, the Li^+ diffusion coefficient is stable (about 10^{-10} m^2 s^{-1}).[37] Because the salt dissociation generates both cations and anions, the Li^+ transference number is defined as:[38,39]

$$t_+ = \frac{D_+}{D_+ + D_-} = \frac{\mu_+}{\mu_+ + \mu_-} \quad (4)$$

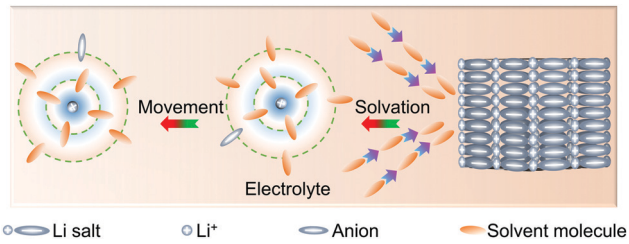

Fig. 5 Scheme of the solvation and movement of solvated Li^+ in the electrolyte.

where t_+ is the Li^+ transference number, D_+ is the Li^+ diffusion coefficient, D_- is the anion diffusion coefficient, μ_+ is the Li^+ mobility and μ_- is the anion mobility. The migration caused by the electric field is related to the initial concentration C (solvation degree, salt concentration) and the ionic mobility μ of cations and anions. The ionic mobility μ is inversely related to its solvation radius r and electrolyte viscosity η based on the Stokes–Einstein relation:[40,41]

$$\mu = \frac{1}{6\pi\eta r} \quad (5)$$

The electrolyte viscosity η has an effect on ionic mobility μ. The ionic conductivity σ is a parameter for quantifying the influence of the degree of salt dissociation and ion mobility in electrochemical systems:

$$\sigma = \sum_i n_i \mu_i Z_i e \quad (6)$$

where n_i is the number of free ions (cation or anion) from the solvation/dissociation process, μ_i the ion mobility, Z_i the valence order of ionic species i, and e the unit charge of electrons. The electrolyte with high ionic conductivity indicates fast ion migration and high salt dissociation degree that mainly benefits migration. Therefore, the two processes of diffusion caused by the concentration gradient and migration caused by the electric field are intertwined with each other and difficult to discuss separately.

In nonaqueous electrolytes, the movement of ions occurs through two steps: (1) the dissociation and solvation of the salt crystal by polar solvent molecules; (2) the free movement of solvated ions in the electrolyte (Fig. 5).[41] During solvation, the salt crystal is dissociated and forms ions surrounded by the coordinated solvents. The movement of ions is always accompanied by "solvation sheath", which consists of a number of oriented solvent molecules and anions.[42] The initial Li^+ concentration C is mainly determined by the solvent nature (dielectric constant or donor number) and the initial salt concentration in the electrolytes. The mobility μ of the solvation sheath depends on the electrolyte viscosity and the local salt concentration, which can regulate the anion transference number t. In a word, the typical variables, such as initial concentration, anions transference number and viscosity have great effects on both migration and diffusion processes: (1) the solvation and initial salt concentration determine the moving numbers of ions in the electrolyte; (2) the electrolyte viscosity can affect the migration by ion mobility and diffusion by the diffusion coefficient. Based on Sand's equation, the adequate and fast-moving Li^+ solvation sheath is critical for extending Sand's time to suppress dendrite growth.[43] For the sake of convenience, the influencing factors (C, t, η) of Sand's equation are placed as the center and the solvation process (donor number, dielectric constant) on the effect of initial concentration C, high-concentration or local high-concentration electrolyte on the effect of initial concentration C and anions transference number t, and the electrolyte viscosity η on the effect of ionic mobility μ, are summarized. Here, we used the term "movement" or "moving" to describe the global effect of these parameters on the diffusion-limited step. In this section, the factors that influence the formation of enough fast-moving Li^+ solvation sheaths, such as dielectric constant, donor number, salt concentration and viscosity, are briefly summarized.

3.1.1 Initial solvated Li^+ concentration. Since the 1960s, the electrolyte solvents from carbonates,[44] ethers,[45] sulfones[46,47] to phosphate esters[48] with high dielectric constant have been widely studied for Li metal batteries. However, it was realized that severe difficulties in terms of cycling life and safety cannot be addressed using the routine solvents, mainly because of the side reactions at the Li/electrolyte interface and irregular dendrite growth. The fluorinated additive, fluoroethylene carbonate (FEC), has been shown to produce a remarkable improvement in the Li anode, and gives rise to LiF-rich SEI for regulating the Li deposition/dissolution behavior.[49] The LiF-rich SEI film improves the cycling stability of the Li anode in three aspects: (1) it is a good electronic insulator (10^{-31} S cm^{-1}), preventing electron transport in the SEI film;[50] (2) it has high surface energy, causing uniform Li^+ deposition beneath the SEI film;[51] (3) it has low diffusion energy barrier, facilitating fast Li^+ diffusion.[52,53] Compared with Li_2O (38.70 meV $Å^{-2}$), Li_2CO_3 (59.22 meV $Å^{-2}$), Li_2S (19.01 meV $Å^{-2}$) and LiCl (37.55 meV $Å^{-2}$), LiF has the highest surface energy (73.28 meV $Å^{-2}$).[51] Such high surface energy suppresses the vertical dendrite growth into the SEI, but a horizontal growth along the interface. In general, interstitials and vacancies, knock-off and grain boundaries are main pathways for ion transport through the inorganics in SEI. On account of the strong bond energy between Li and F in LiF, bulk LiF hardly contributes to the diffusion of Li^+. First principles calculations show that Li^+ diffusion rate along the grain boundary is faster than in bulk, and the heterogeneous LiF/Li_2O grain boundary exhibits the fastest Li diffusion rate than LiF/LiF and Li_2O/Li_2O.[54] The analysis shows that the surface diffusion of Li^+ over a surface of LiF is lower by 0.09 eV.[55] This indicates that the rate of transport of Li^+ on LiF is more than 30 times faster than on Li_2CO_3 substrate. The columnar Li deposition morphology guided by LiF-rich initial surface proves that LiF can regulate the uniform Li deposition by fast surface diffusivity of Li^+.[52] Although there is lack of direct experimental evidence for Li^+ diffusion mechanism through LiF, it is reasonable to accept that the grain boundary is a dominate pathway for fast Li^+ diffusion. The details about the surface energy and diffusion barrier will be discussed in Section 3.3.2. Later, the development of organic solvents with different fluoride substitutions has been considered

Table 1 Dielectric constant, donor number, and viscosity of different solvents or anions[41,60–68]

Solvents	Dielectric constant (ε)	Donor number (kcal mol^{-1})	Viscosity (η, mPa s)
EC	89.8	16.4	1.9
PC	65	15	2.53
DEC	2.8	16	0.75
DMC	3.1	15.1	0.59
FEC	79.7	9.1	4.4
FEMC	7.2	—	—
HFE	6.2	1.9	—
DME	7.2	20	0.46
ES	41	15.3	2.056
EMC	3	—	0.65
Hx	1.9	0	0.294
TEP	20.6	23	—
TMS	42	14.8	—
GBL	—	18	—
$TFSI^-$	—	5.4	—
FSI^-	—	9	—
NO_3^-	—	21.1	—

EC: ethylene carbonate; PC: propylene carbonate; DEC: diethyl carbonate; DMC: dimethyl carbonate; FEC: fluoroethylene carbonate; FEMC: 3,3,3-fluoroethylmethyl carbonate; HFE: 1,1,2,2-tetrafluoroethyl-2′,2′,2′-trifluoroethyl ether; DME: 1,2-dimethoxyethane; ES: ethylene sulfite; EMC: ethyl methyl carbonate; Hx: hexane; TEP: triethyl phosphate; TMS: tetramethylene sulfone; GBL: γ-butyrolactone; $TFSI^-$: bis(trifluoromethane)sulfonimide; FSI^-: bis(fluorosulfonyl) imide. NO_3^-: nitrate.

an effective strategy for stabilizing the Li anode, since the decreased highest occupied molecular orbital (HOMO) and lowest unoccupied molecular orbital (LUMO) energies lead to high oxidation potential and form stable LiF-rich SEI film.[56] Nevertheless, the solvents with different fluorine substitutions decrease the dielectric constant and result in low solubility of the Li salt, along with high polarization.[57] Dielectric constant, the signature of the electronic polarizability of solvents, determines the ability to solvate Li^+ from the crystal lattice and the formation of the Li^+ solvation sheath.[58]

The development of advanced electrolyte formulations has become a promising strategy to produce solutions that have high dielectric constant and form stable SEI film. For example, the all-fluorinated electrolyte formulation has been developed, in which all the components (solvents and salts) are likely to contribute fluorine-rich interphase.[56] This electrolyte is 1 M $LiPF_6$ in mixture of FEC, 3,3,3-fluoroethylmethyl carbonate (FEMC), and 1,1,2,2-tetrafluoroethyl-2′,2′,2′-trifluoroethyl ether (HFE) (FEC : FEMC : HFE, 2 : 6 : 2 by weight). Based on density functional theory (DFT), FEMC and HFE molecules can easily produce LiF due to the high thermodynamic potential. While the low dielectric constants of the solvents (6.2 for HFE and 7.5 for FEMC, Table 1) limit the salt solubility and ionic conductivity, requiring the co-presence of FEC (dielectric constant: 79.7) as the main solvating agent to provide both adequate cation concentration and LiF-rich anode interface. This all-fluorinated electrolyte with moderate ionic conductivity (5.1×10^{-3} S cm^{-1}) produces dense and smooth Li deposition morphology. In addition to the fluorinated solvents, EC molecules combined with ethylene sulfite (ES) have been used to give both high salt dissociation and stable sulfurized SEI film.[59] With its high dielectric constant (89.8), the EC molecule effectively dissociates the Li salt for moderate ionic conductivity. The high content of sulfurized components (Li_2S and Li_2S_2) effectively promote the formation of a more compact sulfurized SEI to facilitate fast Li^+ diffusion.

However, the dielectric constant, which indicates the electronic polarizability of solvent, cannot completely explain all the salt dissociation.[71] For example, the $LiNO_3$ additive has a high solubility in ether-based electrolytes with low dielectric constant (such as DME for 7.2),[72] but negligible solubility in cyclic ester-based electrolytes with high dielectric constant (such as 65 for propylene carbonate (PC)).[68] Donor number is commonly-used parameter that reflects the Lewis basicity of solvent.[64] In brief, to dissociate salts in organic electrolytes, electron donation from the solvent molecule to the cation has to exceed the electronic interaction between the cation and anion. Solvents with high donor number can achieve high salt solubility due to the strong interactions between the solvents and hard Lewis acids, such as Li^+. As shown in Table 1, the donor number of cyclic carbonate (such as PC: 15) is lower than that of NO_3^- (21.1) and DME (20), which accounts for the low solubility of nitrate salt in carbonates, but its high solubility in ether-based electrolytes. The ether-type solvents generally suffer from poorer oxidative stability (<4 V *vs.* Li^+/Li) than ester solvents (4.5 V *vs.* Li^+/Li), which limit their use with high-voltage cathode materials, such as $LiCoO_2$ and $LiNi_{1/3}Mn_{1/3}Co_{1/3}O_2$.[68] Usually ester-based electrolytes produce severe Li dendrite growth, a low CE (<90%) and short cycling life of the Li anode, and it is significantly challenging to develop such electrolytes to address these shortcomings.

On the basis of the Gutmann donor number theory, carbonate-ether mixed electrolyte (1 M $LiPF_6$ in FEC/DMC/DME (3.5 : 3.5 : 3, by volume) with 1 wt% $LiNO_3$) was used to increase the solubility of $LiNO_3$.[73] Here, the FEC has three functions: (1) it improves the oxidation potential to widen the electrochemical stability window; (2) it dissociates $LiPF_6$ to favor more free Li^+; (3) it produces abundant LiF in the SEI film to protect the anode. DME with high donor number (20) accounts for the high solubility of $LiNO_3$ in this mixed electrolyte. With high oxidation potential of 4.2 V (*vs.* Li^+/Li), the coin cells of $LiFePO_4$‖Li retain 80.8% of their initial specific capacity after 1000 cycles. The solubility of the $LiNO_3$ additive in 1 M $LiPF_6$ EC/DEC electrolyte was increased to 5 wt% by the introduction of 0.5 wt% tin trifluoromethanesulfonate as solubilizer.[69] Sn^{2+} with appropriate Lewis acids can coordinate NO_3^- to form a Sn^{2+}–NO_3^- solvation structure for high $LiNO_3$ solubility (Fig. 6a). γ-Butyrolactone (GBL) with high donor number (18) has also been used as co-solvent to improve the solubility of $LiNO_3$ in ester electrolytes.[74] To evaluate the solvating ability, the mixture of $LiNO_3$ and $LiPF_6$ was co-dissolved in a variety of ester-based solvents (PC, FEC, DMC and GBL). It is found that $LiNO_3$ is insoluble in PC, FEC and DMC solvents when the concentration is below 0.1 M. In contrast, no precipitation has been observed even when the concentration of $LiNO_3$ is increased up to 0.5 M in GBL (Fig. 6b). In addition, triethyl phosphate (TEP) with high donor number (26) is used as

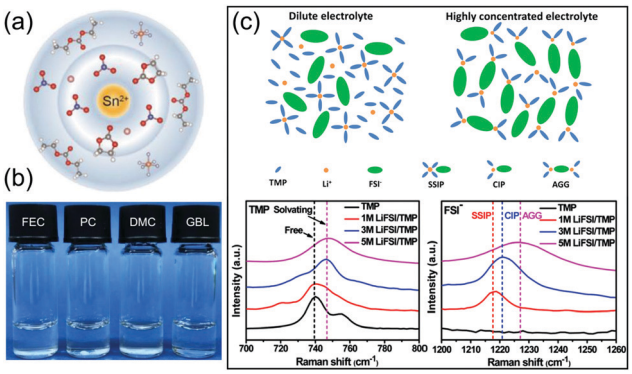

Fig. 6 (a) Schematic of the solvation structure in solubilizer-mediated carbonate electrolyte. Reproduced with permission from ref. 69. Copyright 2020, Wiley-VCH. (b) Solubility of $LiNO_3$ in different solvents. The molar concentration of $LiNO_3$ in PC, FEC and DMC are 0.1 M, 0.1 M and 0.5 M in GBL, respectively. PC: propylene carbonate, GBL: γ-butyrolactone. Reproduced with permission from ref. 68. Copyright 2020, Wiley-VCH. (c) Schematic of the solvation structure in dilute and highly concentrated electrolytes and Raman spectra of various LiFSI/TEP electrolytes. LiFSI: lithium bis(fluorosulfonyl)imide, TEP: triethyl phosphate. Reproduced with permission from ref. 70. Copyright 2018, Royal Society of Chemistry.

additive for ester-based electrolytes to increase the solubility of $LiNO_3$.[75]

Recently, highly concentrated salt electrolytes have been shown to contribute significantly to the performance of Li anode in three aspects. They have (1) high initial Li^+ concentration C to lengthen the Sand's time; (2) high ionic charge density and Li^+ transference number (fast ion mobility is beneficial for migration caused by the electric field) to give adequate Li^+ flux; (3) stable interface to produce high CE. For example, the nonflammable phosphate-based electrolyte has been developed with 5 M lithium bis(fluorosulfonyl) imide (LiFSI) in TEP solvent.[70] Although it has low ionic conductivity of 0.9×10^{-3} S cm^{-1}, this highly concentrated electrolyte achieves higher Li^+ transference number (0.42) than 1 M $LiPF_6$/EC–diethyl carbonate (DEC) (0.24). As the LiFSI concentration was increased, the amount of free FSI^- decreased because of strong interaction between the Li^+ and FSI^-, along with the formation of contact ion pairs (FSI^- coordinating to one Li^+) and aggregate clusters (FSI^- coordinating with two or more Li^+) (Fig. 6c). As a result, most anions combined with the small Li^+ move freely in the highly concentrated electrolyte, which gives rise to the increased Li^+ transference number. The unique solvation structure of the highly concentrated electrolyte was analyzed by Raman spectroscopy. In the 1 M LiFSI/TEP dilute electrolyte, most TEP molecules exist in the free state. When the LiFSI concentration increases to 3 M, the vibration bands (P–O–P) shift up to higher wavenumbers, suggesting that most TEP molecules are coordinating with Li^+. Similarly, with increasing LiFSI concentration, the amount of free FSI^- decreases. This unique solvation structure is responsible for the increased Li^+ transference number in the highly concentrated electrolyte. The highly concentrated electrolyte with 7 M LiFSI in FEC further increase the Li^+ transference number to 0.53.[76] The electrolyte showed stable cycling above 130 cycles with $LiNi_{0.5}MnO_4$ cathode at 0.36C. In addition, a new salt $Li(FSO_2)N(SO_2CF_3)$ was synthesized and dissolved in DOL/DME (1 : 1) with 4 M concentration,[77] because of its highly delocalized anion structure, it had higher Li^+ transference number (0.68) than other electrolytes (4 M $LiClO_4$: 0.46, 4 M $LiCF_3SO_3$: 0.53 and 4 M $LiC_2F_6NO_4S_2$: 0.67). By optimizing the type of anion, the concentration and the solvent, the unexpected high Li^+ transference number (0.73) is obtained in the class of "solvent-in-salt" electrolytes, which provides adequate Li^+ flux to improve the uniformity of Li deposition.[78] For a promising electrolyte, several key requirements must be simultaneously met:

(1) high dielectric constant or donor number to give high degree of salt dissociation; (2) high Li^+ transference number for fast ion movement in the electrolyte; (3) stable interphase ingredients for anode protection; (4) high oxidation potential to give wide electrochemical working window.

3.1.2 Li^+ mobility in the electrolyte. When solvated Li^+ moves in bulk electrolyte, the electrolyte viscosity η plays an important role in determining Li^+ mobility. To explore the effect of η, a series of linear ethers were chosen as solvents because the value of η could be controlled by the molecular length of the ether.[79] It is known that different molecular weights of solvents usually give rise to different viscosities. To screen the η on the effect of Li dendrites, the short-circuiting times, $T(h)$, of Li symmetric cells with 1 M LiTFSI in DME, tetraglyme or polyglyme electrolytes were measured. It was found that the DME-based electrolyte had the highest T, which confirmed that the solvent with smaller η effectively lowers the Li dendrite growth. However, the paradox is that the solvent with high dielectric constant always has high viscosity. For dilute electrolyte, the balance between dielectric constant and viscosity is critical for evaluating the contributions of the solvent on cation mobility. To address this issue, a new concept of "dielectric-fluidity" is proposed to evaluate the ion mobility:[80]

$$d = \varepsilon \cdot \eta^{-1} \quad (7)$$

where ε is the dielectric constant of the solvent. A series of fluorinated liquefied gas solvents, which have moderate dielectric constants (*ca.* $\varepsilon = 10 \approx 15$) and exceptionally lower room temperature viscosity than conventional liquid solvents, were studied. As a result, the liquefied gas solvents exhibit superior dielectric-fluidity, which allows high ion mobility at low temperatures (Table 2 and Fig. 7a). When 0.02 M tetrabutylammonium hexafluorophosphate is added to difluoromethane (DFM), high ionic conductivity of 2 mS cm^{-1} is obtained even at −60 °C. The deposited Li is highly uniform with micrometer-size grains and no dendrite growth. To address the low salt solubility in the liquefied gas electrolytes, an amount of tetrahydrofuran is added to the fluoromethane (FM).[81] The resulting electrolyte showed high ionic conductivity (2.8 mS cm^{-1} at −60 °C) and high Li^+ transference number (>0.79), leading to dramatic improvement of the cycling performance of Li anode. Acetonitrile (AN)/FM electrolyte containing 1.2 M LiTFSI is also developed,[82] and showed excellent ionic conductivity (>4 mS cm^{-1}) from −78 °C to 75 °C. The liquefied gas electrolyte also achieves excellent Li metal stability with an

Table 2 Physical properties of liquefied gas and liquid solvents[80]

Solvent	Melting temperature (°C)	Boiling temperature (°C)	Relative dielectric constant (ε)	Viscosity (mPa s)	$d = \varepsilon\eta^{-1}$ (mPa s)$^{-1}$
FM	−142	−78	9.7	0.085	114
DFM	−136	−52	14.2	0.120	118
FE	−143	−38	—	0.125	—
1,1-DFE	−117	−24	12.5	0.173	72
1,1,1,2-TFE	−101	−26	9.7	0.207	47
2-FP	−133	−9	—	—	—
AN	−45	81.6	35	0.3	117
DCM	−97	40	7	0.35	20
THF	−108	66	6	0.4	15

FM: fluoromethane; DFM: difluoromethane; FE: fluoroethane; 1,1-DFE: 1,1-difluoroethane; 1,1,1,2-TFE: 1,1,1,2-tetrafluoroethane; 2-FP: 2-fluoropropane; AN: acetonitrile; DCM: dichloromethane; THF: tetrahydrofuran.

average CE of 99.4% over 200 cycles in the extreme conditions of 3 mA cm^{-2} and 3 mA h cm^{-2}.

The ionic mobility of electrolyte not only depends on the solvent but on the salt concentration. Although highly concentrated electrolyte can achieve better performance than dilute electrolyte in terms of rate capability, a large number of anions with large volume hinder cation mobility due to their high viscosity.[83] For example, highly concentrated sulfone-based electrolytes are known for their strong oxidation resistance and high CE.[84] However, their high viscosity and poor wettability greatly limit their use in Li metal batteries.[41] In addition, the induced high viscosity also reduces the Li^+ diffusion coefficient.[85] To address this issue, the concentrated electrolyte is diluted with 1,1,2,2-tetrafluoroethyl-2,2,3,3-tetrafluoropropyl ether and forms localized high-concentration electrolyte.[86] The diluent is miscible with the electrolyte solvent molecules but does not dissolve any Li salt, and has low viscosity as well as wide electrochemical stability window. Recently, the fluorinated aromatic compound 1,2-difluorobenzene is used as diluent solvent in 2 M LiFSI–DMC/bis(2,2,2-trifluoroethyl)ether electrolyte (Fig. 7b).[87] This diluent is remarkable because it produces both low viscosity of the high-concentration electrolyte and LiF-rich SEI layer, as well as fast ion mobility.

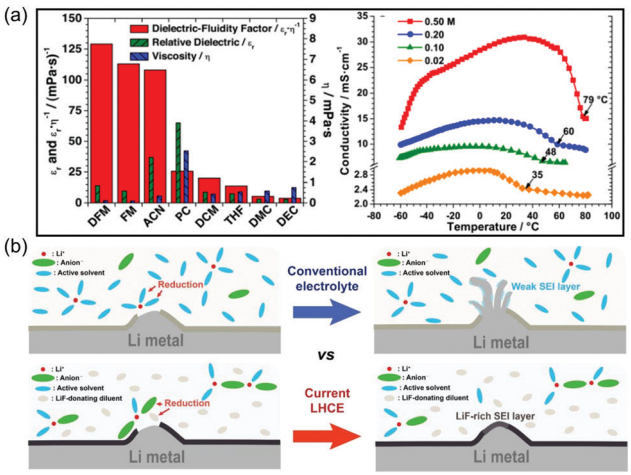

Fig. 7 (a) Relative dielectric constant, viscosity, and dielectric-fluidity values of various solvents and the ionic conductivity of different tetrabutylammonium hexafluorophosphate concentrations in difluoromethane. The solvents are: fluoromethane (FM), difluoromethane (DFM), acetonitrile (AN), dichloromethane (DCM), tetrahydrofuran (THF), PC (propylene carbonate), DMC (dimethyl carbonate), DEC (diethyl carbonate), with the first two being liquefied gas solvents. Reproduced with permission from ref. 80. Copyright 2017, Science Publishing Group. (b) Schematics of the mechanism of SEI layer formation in the conventional electrolyte and localized high-concentration electrolyte (LHCE in the figure). Reproduced with permission from ref. 87. Copyright 2020, Wiley-VCH.

3.2 Li^+ desolvation at the SEI/electrolyte interface

When the Li^+ solvation sheaths move to the region of the SEI/electrolyte interface, Li ions need to break up the solvation sheath for subsequent migration in the SEI (Fig. 8). Similar to the Li^+ desolvation process at the surface of graphite anode, it is believed that the most sluggish process occurs when the solvated Li^+ sheds its solvation sheath, rather than when the Li^+ diffuse through the SEI at the graphite anode.[88] This kinetically limited process is known as the "charge-transfer" component and has an energy barrier of 50–70 kJ mol^{-1}. This high activation energy is attributed to the small ionic radius of Li^+, which has strong coulombic attraction to solvent molecules in the Li^+ solvation sheath.[89] For conventional electrolyte, it is believed that a number of polar solvents, especially those containing polar groups, such as carbonyl (C═O), ether-linkage (O–O) and sulfonyl (S═O), tightly adhere to Li^+ and dominate the primary solvation sheath, along with a few anions that occupy the second or third solvation sheath.[41] In this section, the effect of the Li^+ solvation structure on the Li^+ desolvation energy is summarized, including the distinct solvent molecules and anions.

3.2.1 Effect of non-polar solvents on Li^+ solvation environment. To ensure high ionic conductivity, the solvents should have high dielectric constant or donor number to dissolve enough Li salt. However, this requirement brings about two physical or chemical characteristics that significantly limit the electrochemical performance of the cells. First, high dielectric

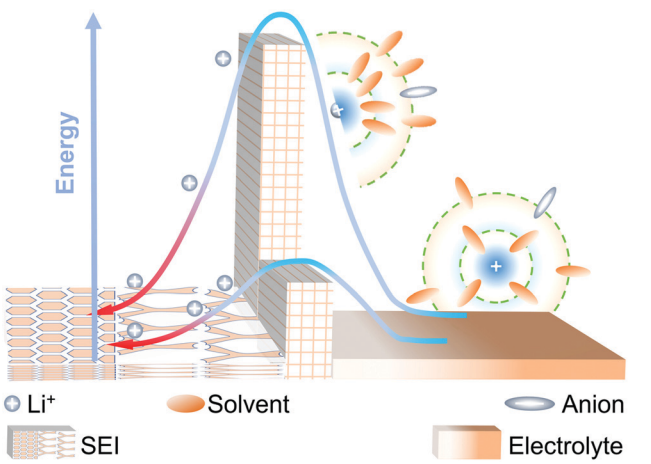

Fig. 8 Scheme of the Li^+ desolvation step at the SEI/electrolyte interface.

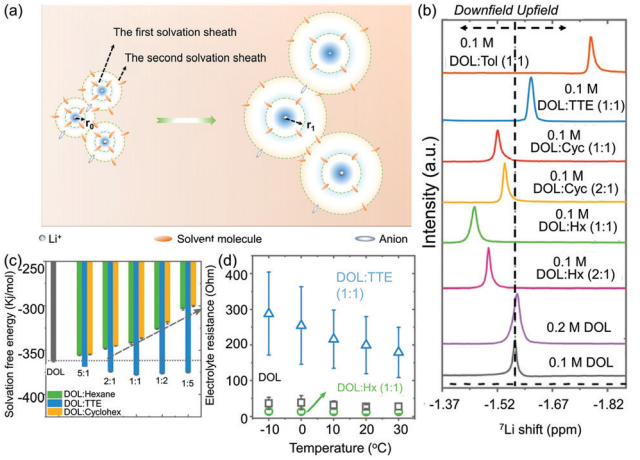

Fig. 9 (a) Scheme of easy Li^+ desolvation by the distance of Li^+ center to solvent dipole. (b) ^7Li NMR spectra of different electrolyte mixtures. (c) Li^+ solvation free energies in different electrolyte mixtures computed by molecular dynamics simulation. (d) Total electrolyte resistance (contact + bulk resistance) as function of temperature. DOL: 1,3-dioxolane, TTE: 1,1,2,2-tetrafluoroethyl 2,2,3,3-tetrafluoropropylether, Hx: hexane, Cyc: cyclohexane. Reproduced with permission from ref. 92. Copyright 2019, Wiley-VCH.

constant or donor number indicates strong binding affinity between Li^+ and the solvated solvent, which consumes a large amount of energy during the Li^+ desolvation process. Second, in conventional electrolytes, Li^+ are coordinated with solvents and form solvation sheath with large volume, which accounts for the low Li^+ transference number of 0.2–0.4.[41] The ion–solvent interaction in the Li^+ solvation sheath can be attributed to ion–dipole interaction. Based on the electrostatic forces, the distance of Li^+ center to the nearest polar group (such as C═O, –O–, $–SO_2–$) of solvent r has a very significant impact on the solvation/desolvation process:[90,91]

$$U_{\text{ion-dipole}} = -\frac{1}{4\pi\varepsilon}\frac{ze\mu\cos\theta}{r^2} \quad (8)$$

where ε is the dielectric constant, ze is the ion charge, μ is the dipole moment of the solvent, r is the distance between the Li^+ center and the nearest solvent dipole, and θ is the dipole angle relative to the line r joining the ion and the center of the dipole. Obviously, an increase in r reduces the interaction between Li^+ center and the solvent dipole, and produces low Li^+ desolvation energy barrier without influencing the Li^+ concentration (Fig. 9a).

Non-polar solvents have been added to electrolytes to reduce the solvation degree of the Li^+ solvation sheath. Such non-polar solvents must satisfy the following requirements: (1) be non-reactive with other components, such as Li metal, separator and solvents; (2) be insoluble with Li salt and not coordinate with Li^+ in the electrolyte; (3) be liquid over wide temperature range, which gives low resistance to ion diffusion; (4) be miscible with the solvated solvents, so that it dilutes the electrolyte. With its non-polar functional groups, mineral oil (long chain alkane) are susceptible to undesired redox reactions with the Li anode.[92] For example, hexane has been chosen as non-polar diluent in 0.1 M LiTFSI–DOL electrolyte. In this electrolyte, Li^+ ions are loosely solvated and move freely. In comparison, the addition of the fluorinated solvent, 1,1,2,2-tetrafluoroethyl-2,2,3,3-tetrafluoropropylether (TTE), increases the electron density cloud around Li^+, leading to an upshift in the Li nuclear magnetic resonance (NMR) spectrum (Fig. 9b), indicating stronger coordination. The solvation free energy of solvated Li^+ is computed using classical molecular dynamics, which shows that the free energy of the Li^+ solvation sheath greatly decreases when hexane or cyclohexane is added to the DOL solvent but increases when TTE is added (Fig. 9c). These results indicate that the dilute Li^+ coordination structure forms when using hexane or cyclohexane, in contrast to strong coordination with TTE. The decreased solvation free energy greatly reduces the charge-transfer resistance during cycling (Fig. 9d). The fluorinated non-polar solvents tetrafluoro-1-(2,2,2-trifluoroethoxy)ethane and methoxyperfluorobutane have been also investigated in highly concentrated electrolytes.[93] To discover the effects of different electrolytes, the Li^+ solvation/desolvation energies of the carbonate-based electrolyte and disassociated electrolyte were calculated by molecular dynamics. For 1 M $LiPF_6$–EC/DMC (3 : 1 molar) electrolyte, the solvation energy is about −9.05 kcal mol^{-1}. When the solvent blend changes to low-dielectric-constant FEC/FEMC or FEC/DEC (3 : 1), the respective solvation energy dramatically decreases to −1.26 and −0.33 kcal mol^{-1}. As the non-polar solvents tetrafluoro-1-(2,2,2-trifluoroethoxy)ethane or methoxyperfluorobutane are added to 1 M $LiPF_6$–FEC/FEMC or 1 M $LiPF_6$–FEC/DEC electrolytes, the solvation energy becomes positive, which indicates that the interaction is energetically unfavourable between Li^+ and the non-polar solvents. Low Li^+ desolvation energy effectively reduces the charge-transfer resistance and enables fast Li^+ desolvation.

3.2.2 Role of anions in the primary solvation sheath. The formation of Li^+ solvation sheath is the competition between cation–anion, cation–solvent and solvent–solvent interactions. Because the charge density is localized on small Li^+ (0.09 nm), the Li^+–solvent interaction is far stronger than the interaction between Li^+ and the anion counterpart.[94] Hence, to some extent, the Li^+ desolvation energy can be reduced when the solvent molecules are replaced with anions in the Li^+ solvation sheath (Fig. 10a). Lithium trifluoroacetate (LiTFA) with strong polar groups (C═O and COO^-) is used by our group to change the structure of the Li^+ solvation sheath.[95] DME is chosen as the main solvated solvent due to its chemical stability with Li anode. LiTFA has two advantages: (1) easy dissociation in aprotic solvents (DME) for its electron-withdrawing group ($–CF_3$); (2) low LUMO energy for the prior reduction to form an SEI with more LiF. Attenuated total reflection Fourier transform infrared spectroscopy (ATR-FTIR) shows that the C═O asymmetric stretching frequency of LiTFA shifts by 19 cm^{-1}, indicating strong interaction between Li^+ and carbonyl oxygen groups in the Li^+ solvation sheath (Fig. 10b). The activation energy of Li^+ desolvation was measured by temperature-dependent electrochemical impedance spectroscopy (EIS) on the basis of Arrhenius equation:

$$k = \frac{T}{R_{\text{ct}}} = A\exp^{\frac{-E_a}{RT}} \quad (9)$$

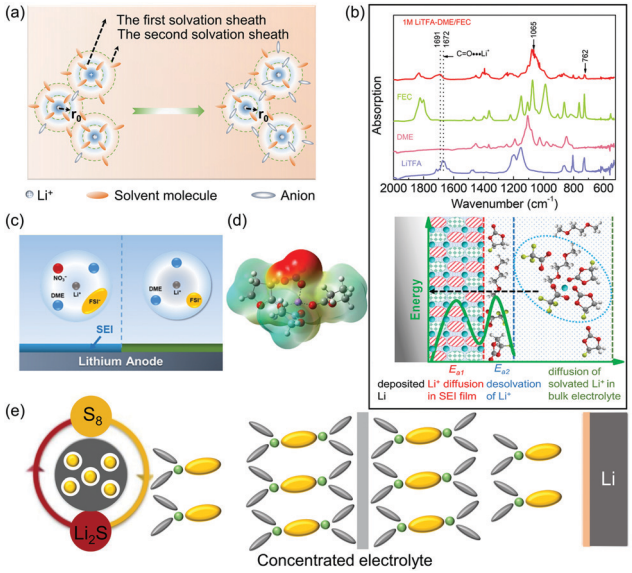

Fig. 10 (a) Scheme of anions in the primary solvation sheath affects the Li^+ desolvation process. (b) ATR-FTIR of LiTFA, DME, FEC, and 1 M LiTFA–DME/FEC and schematic of the Li deposition process in 1 M LiTFA–DME/FEC. LiTFA: lithium trifluoroacetate, DME: 1,2-dimethoxyethane, FEC: fluoroethylene carbonate. Reproduced with permission.[95] Copyright 2020, Wiley-VCH. (c) Schematic of how NO_3^-–FSI^- affects the Li^+ solvation sheath. Reproduced with permission from ref. 96. Copyright 2019, American Chemical Society. (d) Electrostatic potential map based on the electron density of GBL and $LiNO_3$ in the Li^+ solvation sheath. Reproduced with permission from ref. 68. Copyright 2020, Wiley-VCH. (e) Schematic of the sulfur redox chemistry, polysulfide shuttling, and Li dendrite growth for Li–sulfur batteries in concentrated siloxane electrolyte. Reproduced with permission from ref. 97. Copyright 2020, Wiley-VCH.

where k is the rate constant, T is the absolute temperature, R_{ct} is the ion transfer resistance, A is pre-exponential constant, E_a is the energy barrier of Li^+ desolvation from the Li^+ solvation sheath, and R is the gas constant. Compared to Li^+ desolvation energies in $LiPF_6$–EC/DEC (69.14 kJ mol^{-1}) and $LiPF_6$–DME/FEC (64.92 kJ mol^{-1}), LiTFA–DME/FEC (60.02 kJ mol^{-1}) showed a slight decrease. With strong coordination between C=O and Li^+, TFA^- can replace some of the solvent molecules to regulate the environment of the Li^+ solvation sheath and lower the Li^+ desolvation energy.

In addition to fluorinated anions, NO_3^- is another anion used to regulate the Li^+ solvation sheath. It has two advantages for Li anode: (1) it has high reduction potential 1.7 V (*vs.* Li^+/Li), making it more likely to decompose than most components of the electrolyte;[98] and (2) it forms SEI film rich in LiN_xO_y, which has high ionic conductivity for Li^+ transport.[99] The introduction of nitrate anions into the Li^+ solvation sheath was achieved by blending $LiNO_3$ and FEC in DME-based electrolyte.[73] In this electrolyte, FEC and NO_3^- both participate in the primary solvation sheath and form the SEI film with an abundance of LiF and LiN_xO_y, which improves the uniformity of the SEI for homogeneous Li deposition. Two blended anions (NO_3^- and FSI^-) were also added to the Li^+ solvation sheath,[96] and the addition of NO_3^- changes the original solvation structure of FSI^- and promotes its complete decomposition to produce the stable SEI (Fig. 10c). As described in Section 3.1.1, ester-based electrolytes with low donor number have negligible solubility for $LiNO_3$. Recently, $Mg(NO_3)_2$ has been added to ethyl methyl carbonate (EMC)/FEC (3 : 1 volume) electrolyte without other additives, and this produced long cycling stability and high efficiency of Li anode.[100] In this electrolyte, NO_3^- partially replaces solvent molecules in the first Li^+ solvation sheath (Fig. 10d), which is important because Li^+ can be easily desolvated from the new solvation structure. With earlier reduction than the other components in the Li^+ solvation sheath, NO_3^- is easily expelled from the solvation sheath and produces SEI film with high ionic conductivity.

Another key factor for enhancing the participation of anions in the solvation sheath is the salt concentration. With an increase of salt concentration, more solvent molecules and anions are present in the solvation sheath in the form of aggregate solvents and contact ion pairs.[83] For example, super highly concentrated AN electrolyte can produce reversible Li^+ intercalation/deintercalation on the graphite anode.[101] By Raman spectroscopy, it is found that in the dilute electrolyte (1 M), the majority of the $TFSI^-$ exists as free anions with a small number of contact ion pairs and aggregates ($TFSI^-$ coordinating to single Li^+). As the salt concentration increases, the number of free $TFSI^-$ anions decreases and forms more contact ion pairs and aggregates. At 4.2 M concentration, almost all the $TFSI^-$ anions exist as aggregates with strong coulombic interaction with Li^+, which indicates that more anions contribute to the Li^+ solvation sheath. To further increase the coordination of anions with Li^+, the newly concentrated electrolyte composed of 5 M LiTFSI in siloxane is used (Fig. 10e).[97] Through the combination of experimental and computational investigations, it is found that the siloxane effectively regulates the solvation-ion-exchange process in the concentrated electrolyte. As a result, robust SEI film was formed and enabled highly reversible Li plating/stripping. The LiFSI salt concentration could be increased to 10 M when using DMC solvent.[102] The FSI^- principally occupied the Li^+ solvation sheath and induced the anion-dominated SEI with more inorganics, which produced fast ion transport and low Li plating/stripping overpotential.

3.3 Li^+ ion diffusion through the SEI film

Based on the SEI-induced nucleating model, the solid-limited kinetics (Li^+ diffusion through SEI) are important during the dendrite formation. The Li^+ transfer activation energy at the graphite/electrolyte interface has been explored by Ogumi *et al.*[103] The processes of Li^+ breaking up the solvation sheath and diffusing through the SEI film consume about 50–60 and 25 kJ mol^{-1}, respectively. Moreover, the Li^+ desolvation ability for different linear/cyclic carbonate ratios has been studied and it is shown that Li^+ desolvation is the rate-determining step during Li^+ transfer.[88] However, unlike graphite anode with volume expansion of about 10% during lithiation, the relative volumetric change of Li plating is determined by the plating capacity.[104] From practical perspective, the areal capacity of single-sided commercial electrode needs to reach at least

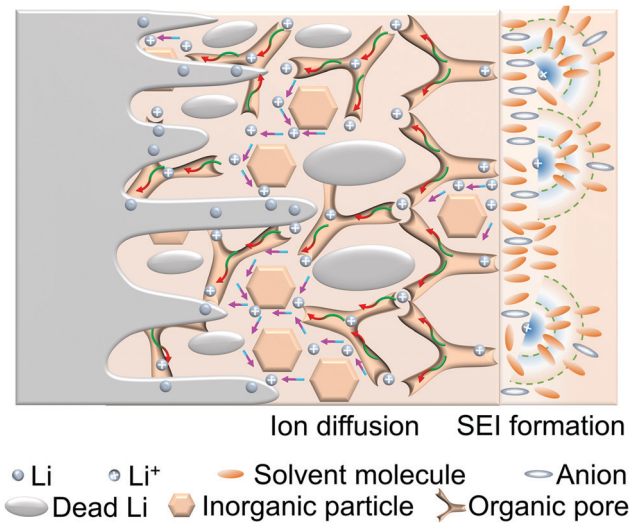

Fig. 11 Scheme of the formation of the SEI and its role in the Li^+ diffusion and dendrite growth suppression. For the sake of simplification, the mechanisms of ion transport through the organic and inorganic species are pore diffusion and grain boundary, respectively.

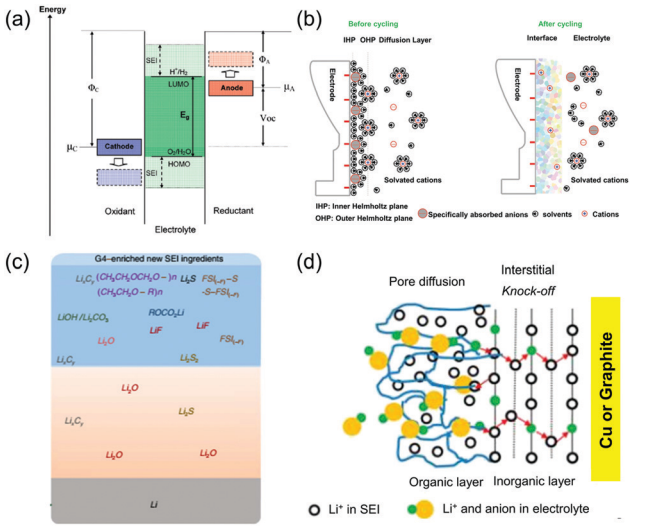

Fig. 12 (a) Schematic of the relationship between SEI formation on the electrodes and the LUMO/HOMO of electrolytes. LUMO: lowest unoccupied molecular orbital, HOMO: highest occupied molecular orbital. Reproduced with permission from ref. 106. Copyright 2010, American Chemical Society. (b) Schematic of interface formation before cycling: ions and solvent molecules first absorb on the inner Helmholtz plane, and during cycling: they are decomposed/oxidized on the inner Helmholtz plane. Reproduced with permission from ref. 107. Copyright 2020, Wiley-VCH. (c) Scheme of the modification of the surface film chemistry of Li. Reproduced with permission from ref. 119. Copyright 2017, Nature Publishing Group. (d) Schematic of pore diffusion in the porous organic layer of an SEI and knock-off diffusion in the dense inorganic layer of SEI. Reproduced with permission from ref. 120. Copyright 2012, American Chemical Society.

4 mA h cm^{-2}, which is equivalent to 20 μm increase in thickness for Li. From the microscopic point of view, needle-like dendrites can induce rupture of the fragile SEI film during Li plating (Fig. 11),[105] and the newly exposed Li surface leads to continuous electrolyte decomposition and increasing irreversible capacity loss. Conversely, the nonuniform stripping current will form "dead" Li in the SEI film during the Li plating process. After continuous cycling, porous Li electrode, thick accumulated SEI film and excessive dead Li are produced, which gives rise to low ion conductivity and high capacity loss of the Li anode. Therefore, compared to graphite anode, Li^+ diffusion through the SEI film is more complicated in Li anode. In this section, the possible formation mechanism and models of the SEI film, followed by two of its key features, its specific adsorption and its solvated coordinate structure, and its ion transport mechanism will be briefly summarized. More attention will be paid to the crucial factors of uniform physical structure, the surface energy and diffusion barrier of the chemical components, and the effect of growth thickness of the SEI film on ion transport.

3.3.1 Formation mechanism and models of SEI. The relationship between SEI formation on the electrodes and the LUMO/HOMO of electrolytes is proposed by Goodenough.[106] As shown in Fig. 12a, the energy separation (E_g) of the LUMO and HOMO of the electrolyte determines the electrochemical working window. Supposed the anode and cathode potentials are μ_A and μ_C, respectively, when μ_A is higher than the LUMO of the electrolyte, the electrons will be transferred from the anode to the electrolyte until the electron-insulating SEI is formed, which increases the cathodic limit. Similarly, redox reactions can contribute to the generation of interphase at the cathode/electrolyte interface, which increases the anodic limit. In fact, because of the extreme negative nature of Li, redox reactions between it and nonaqueous electrolytes cannot always be avoided.

The formation of SEI on the anode surface is strongly related to specific adsorption on the electrode and composition of the Li^+ solvation sheath. The former dominates the initial structure and the chemical composition of the interface. Based on classical electrochemical theory, once the electrode contacts the electrolyte, the electrode tends to lose electrons until equilibrium is established (Fig. 12b).[107] When in contact with nonaqueous electrolyte, Li atoms tend to leave the crystal lattice and enter the electrolyte before equilibrium is established. The Li anode has negative charge due to the loss of Li^+, while there is positive charge in the nearby electrolyte. This interface between the electrolyte and the metal phase where excess opposite charges accumulate is defined as the parallel electric double layer.[108] The layer near the electrode surface contains ions or molecules that have strong interaction with the electrode surface, which can be coulombic forces or chemical interactions.[107] The negatively charged metal electrode adsorbs either cations or anions until reaching dynamic equilibrium. The electric double layer is divided into a compact layer and a diffusion layer.[109] The inner part of the compact layer is called as the inner Helmholtz plane, which contains anions and small neutral molecules and the outer part is called as the outer Helmholtz plane, where solvated molecules are dominant. The concentration of excess ions or molecules continuously decays from the outer Helmholtz plane to the diffusion layer, so that the initial adsorbed species on the electrode surface determine

the initial chemical composition and structure of the SEI film. The initial adsorbed species on the Li anode are explored by first-principles calculations,[110] and it is found that the anions with strong binding energy are absorbed on the inner Helmholtz plane and form strong Li–O/N/F interactions. Notably, NO_3^- has stronger interaction with the Li than FSI^- or F^-, and therefore dominates the inner Helmholtz plane on the Li surface, which is responsible for making the SEI film have high ion conductivity. This result is in accordance with reports that $LiNO_3$ is a beneficial additive for the Li metal anode.[110,111] Recently, the adsorbed monolayer of 1,3-benzenedisulfonyl fluoride is bonded onto Cu substrate to alter the interfacial chemical environment by forming a multilayer SEI, which is composed of LiF-rich inner layer and amorphous outer layer of organic species on Li surface.[112] Consequently, the $LiCoO_2$‖Li cell with a capacity of 2.0 mA h cm^{-2} has 200-cycle life at −15 °C.

The latter (the structure of Li^+ solvation sheath) is functioned as a supplying ship to maintain and repair the interface during cycling. In general, the primary solvation sheath is dominated by the looped solvents and a few anions.[113] As the applied potential decreases, the anions are preferentially reduced to form an inorganic-rich SEI film, which can facilitate fast ion transport and achieve good rate performance.[78] To obtain a uniform SEI film with fast ion transport, it is suggested that an ideal solvation structure can be formed as follows:

(1) Functionalize the solvents in the solvation sheath. Although the conventional carbonates are the choice of all commercial LIBs, decomposition ($ROCO_2Li$ and ROLi) in the SEI film is unstable towards the Li anode.[95] In the past, great efforts have been devoted to investigating fluorinated solvents for the SEI with high LiF content.[114,115] The grain boundaries between LiF nanoparticles favor uniform Li^+ diffusion through the SEI.[116] In addition, fluorinated solvents with low HOMO energy can increase the oxidation potential and enlarge the electrochemical stability wondow.[117]

(2) Design anions with low LUMO energy. Such anions are reduced first, which provides general guidelines for finding novel ingredients to modify the SEI components.[118]

(3) Improve the ratio of anions to solvated solvent molecule in the primary solvation sheath.[102] More anions in the Li^+ solvation sheath enhance the formation of an inorganic-rich SEI film, which improves ion transport.

To sum up, specific adsorption on the electrode surface and the structure of the Li^+ solvation sheath in the electrolytes are not isolated but have close relationship. When the solvent molecules have strong interaction with the electrodes, they dominate the inner Helmholtz plane, which enhances the participation of anions in the Li^+ solvation sheath. Conversely, the anions will preferentially occupy the inner Helmholtz plane, leaving most of the solvent molecules in the Li^+ solvation sheath. Therefore, both these two components in the Li^+ solvation sheath determine the physical structure and chemical composition of the SEI film, as well as the nature of Li^+ diffusion across the interface.

To describe the structure of the SEI film, various models have been proposed, such as the coulombic interaction model,[121] the solid electrolyte interphase model,[122] the compact stratified layer model,[123] the layer model[119] and the mosaic model.[124] Typically, the layer and mosaic models are two main ones to describe the spatial distribution of the SEI components. The layer SEI model indicates that the SEI film is composed of two layers. The inner layer is dominated by inorganic agents (Li_2O, Li_2S) with low oxidation state and the outer layer mainly consists of organic species (ROLi and $ROCO_2Li$) with high oxidation state.[119] In general, anions (PF_6^-, FSI^-) are preferentially reduced to compose the main component of the inner layer, and the solvents are reduced to compose the outer organic-rich layer (ROLi and $ROCO_2Li$). The originally generated unstable organic species in the outer layer are further reduced to form more stable inorganic components near the electrode surface (Fig. 12c). Compared to the layer model, Peled *et al.* believe that the reduction products of electrolytes (organic and inorganic species) are randomly dispersed, and this has been described as mosaic SEI.[124] The nonuniform distribution of components in the SEI produces irregular Li^+ transport paths, and the ions diffuse taking the fastest route. To some extent, this mosaic model accounts for the inhomogeneous Li plating/stripping behavior and the Li dendrite growth process.[125] The two models are not contradictory, because the building blocks in each layer of the layer model spontaneously distribute in mosaic form. Although a model that presents the real behavior of the SEI film is still lacking, to a certain degree, these two models help us understand the structure and electrochemistry of the SEI.

Li^+ needs to shed its solvation sheath before diffusion through the SEI film.[42] Because of the intrinsic complexity and multicomponent nature of the SEI, it is difficult to precisely describe the ion transport process. Several models have been proposed to describe the ion diffusion with different simplified and ideal hypotheses. Experimental evidence has shown that the grain boundaries of inorganic components in the SEI play an important role in Li^+ diffusion.[126] Vacancies and interstitials are also considered two major means of Li^+ transport in the SEI film.[127] As a result of DFT and time-of-flight secondary ion mass spectrometer (TOF-SIMS) tests, two-layer model has been proposed: pore diffusion in the outer layer rich in organic species ($ROCO_2Li$) and knock-off diffusion in the inner layer rich in inorganic species (Li_2CO_3) (Fig. 12d).[120] Therefore, there are mainly four paths for Li^+ diffusion through the SEI: porous regions in the outer layer, grain boundaries between components, interstitials and vacancies in the bulk phase.

3.3.2 Interfacial ion transport kinetics. The interfacial transport kinetics of Li^+ are directly associated with three factors: (1) the physical structure of the SEI film; (2) the surface energy and diffusion barrier produced by the chemical components of the SEI; (3) the growth thickness of the SEI film. No matter whether the SEI film is mosaic, layer or has any other structures, the inhomogeneous distribution of its components is responsible for the nonuniform Li^+ flux and irregular Li dendrite growth. Conventional carbonates or ethers are reduced during Li deposition and form an SEI containing abundant organic species ($ROCO_2Li$ and ROLi). The SEI dominated with organics is chemically unstable to Li anode and not

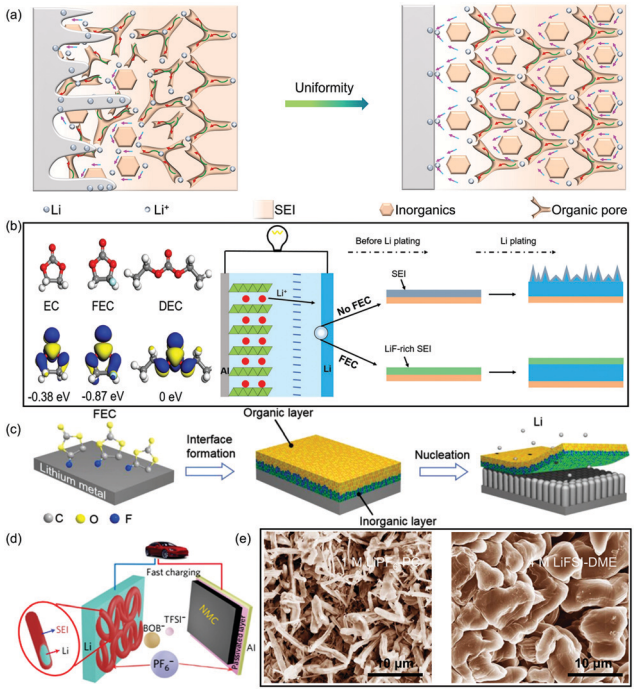

Fig. 13 (a) Scheme of the structural uniformity of SEI for fast Li^+ diffusion. (b) Molecular structure of EC, FEC, DEC, and schematic of the effect of the FEC additive on the Li anode. EC: ethylene carbonate, FEC: fluoroethylene carbonate, DEC: diethyl carbonate. Reproduced with permission from ref. 135. Copyright 2017, Wiley-VCH. (c) Schematic of dual-layer film formation on the Li anode as a result of FEC treatment. Reproduced with permission from ref. 115. Copyright 2018, Wiley-VCH. (d) Schematic of the effect of $LiPF_6$ additive to LiTFSI–LiBOB electrolyte on the Li anode. $LiPF_6$: lithium hexafluorophosphate, LiTFSI: lithium bis(trifluoromethane)sulfonimide, LiBOB: lithium bis(oxalate)borate. Reproduced with permission from ref. 118. Copyright 2017, Nature Publishing Group. (e) Li deposition in 1 M $LiPF_6$–PC and 4 M LiFSI–DME at 1.0 mA cm^{-2} for 1.5 h. PC: propylene carbonate, DME: 1,2-dimethoxyethane. Reproduced with permission from ref. 83. Copyright 2015, Nature Publishing Group.

strong enough to accommodate the rapid volume changes during Li plating (Fig. 13a). Hence, these severe side reactions and rapid Li dendrite growth prevent the practical use of carbonate- and ether-based electrolytes.[12] An anion-derived SEI has proven to be compatible with Li anode because the formed inorganic compounds (LiF, Li_2S, Li_3N) are stable towards Li anode.[128–130] Therefore, the uniform physical structure of the SEI and its inorganic/organic content is important for Li^+ diffusion.[126] The surface energy and diffusion barrier of the chemical components in the SEI layer are also closely related to uneven Li deposition. When the surface energy of the SEI is low, Li dendrites will penetrate the SEI and result in short-circuiting (Fig. 14a). The high interfacial energy of the SEI components improves the mobility of Li^+ along the boundary and suppress the vertical dendritic growth of Li. Low Li^+ diffusion barrier of the SEI can prevent the local accumulation of Li^+ at protuberances and achieve uniform Li^+ flux. In addition, an ideal SEI should not only be thin enough for low diffusion resistance, but act as a sieve to prevent electron tunnelling and allow Li^+ to pass through (Fig. 15a).[131]

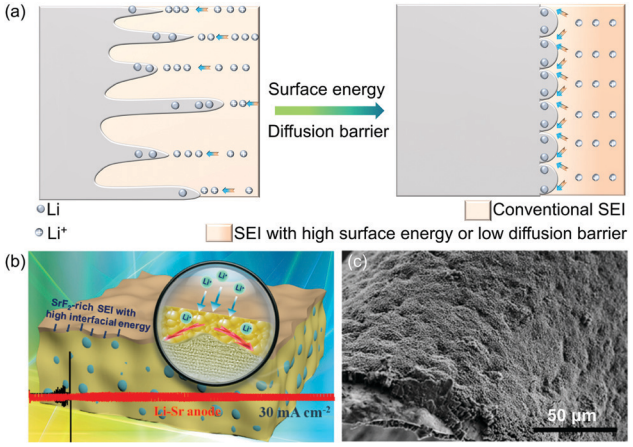

Fig. 14 (a) Scheme of the effect of the nature of SEI (surface energy and diffusion barrier) on Li^+ diffusion. (b) Schematic of a SrF_2-rich SEI with high interfacial energy for uniform Li^+ diffusion. Reproduced with permission from ref. 146. Copyright 2020, American Chemical Society. (c) SEM image of the Li^+ plating morphology with ND (nano-diamond). Reproduced with permission from ref. 147. Copyright 2017, Nature Publishing Group.

Physical structure. Because of their different reactivities and proportions in the Li^+ solvation sheath, the contributions from solvents and anions to the SEI composition are different. For 1 M $LiPF_6$–EC/DMC electrolyte, the Li^+ primary solvation sheath was found to contain 3–6 EC solvent molecules per Li^+ but a

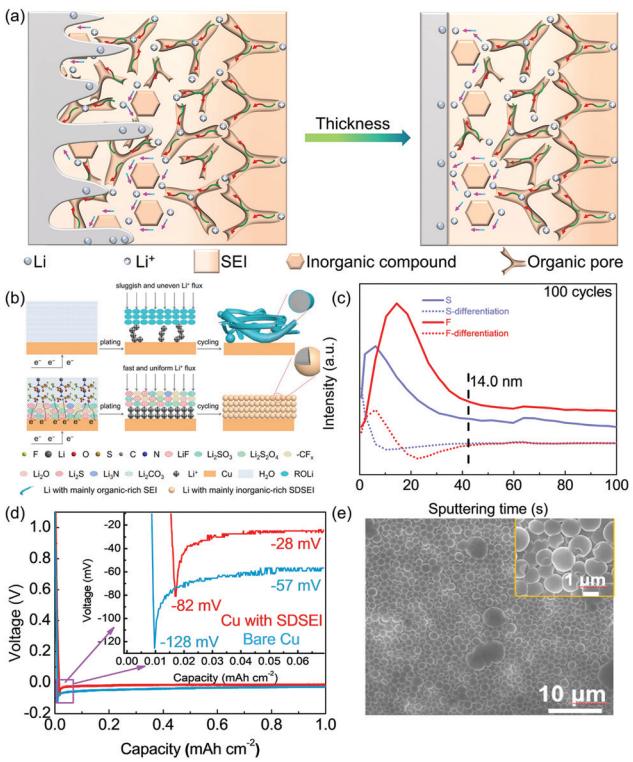

Fig. 15 (a) Scheme of the effect of SEI thickness on fast Li^+ diffusion. (b) Schematic of Li plating behavior on different substrates. (c) TOF-SIMS depth profiles of the SEI film. (d) Voltage–time curves after the 1st Li nucleation. (e) SEM images of Li nuclei on Cu substrate with a protective SEI film. Reproduced with permission from ref. 134. Copyright 2019, Elsevier.

negligible number of anions.[88,94,132,133] The composition of the Li^+ solvation sheath is closely related to the ratio of solvent molecules to anions, which in this electrolyte is about 11 : 1.[95] The reduction species in the SEI are principally determined by the reactivity and proportion of the components (solvent and anions) in the Li^+ solvation sheath. Such high proportion of solvent molecules to anions results in SEI mainly composed of solvent-derived organic species (ROLi, RCOOLi and $ROCO_2Li$), accompanied by a few inorganic species (LiF, Li_2S and Li_2O) derived from anions (Fig. 13a). This solvent-derived SEI has high ion resistivity which causes sluggish ion transport and an inhomogeneous charge distribution of Li^+, which boosts Li dendrite growth.[134] It is therefore important to have more inorganics in the SEI to produce uniform Li deposition.

LiF has been identified as the major component of a fluorinated SEI, which plays a great role in controlling uniform Li^+ diffusion and deposition.[50] The types and relative numbers of fluorinated solvent molecules and anions in the Li^+ solvation sheath determine the structure of the SEI. FEC, with smaller LUMO energy than EC, is a representative fluorinated solvent among various fluorinated cyclic and acyclic carbonates to construct fluorinated SEI (Fig. 13b).[135] In 1 M $LiPF_6$–EC/DEC + 5% FEC electrolyte, high LiF content of 48.2% is produced to greatly regulate the uniform Li deposition. In order to modulate the structure of the SEI, the Li plate is immersed in FEC to form dual-layer SEI film (Fig. 13c). Such SEI gives rise to low polarization and high Li^+ conductivity, as well as uniform and smooth surface without dendrites. In order to increase the amount of LiF in the SEI, the fluorinated solvent with two methyl substituents is used, which donates more LiF than FEC solvent to produce LiF-rich SEI film.[136] Recently, all-fluorinated electrolyte consisting of 1 M $LiPF_6$–FEC/FEMC/HFE (2 : 6 : 2 by volume) has been used with 5 V-class cathode.[56] The high degree of fluorine substitution in the solvent produces superhigh LiF content (90%), which greatly improves the uniformity of the SEI and benefits fast Li^+ diffusion. In addition, fluorinated anions with low LUMO energy are also explored in the hope of achieving excellent SEI stability. LiFSI,[77,137] lithium bis(oxalate)borate (LiBOB),[138,139] lithium difluoro(oxalato)borate (LiDFOB)[140,141] and lithium 1,1,2,2,3,3-hexafluoropropane-1,3-disulfonimide (LiHFDF)[142] are promising Li salt candidates for tuning the SEI chemistry. For example, robust and highly ion-conductive SEI film is formed by the addition of both LiTFSI and LiBOB to carbonate-based electrolytes (Fig. 13d).[118] In Li metal battery using $LiNi_{0.4}Mn_{0.4}Co_{0.2}O_2$ cathode with moderate loading of 1.75 mA h cm^{-2}, the cyclability of 97.1% capacity retention at 1.75 mA cm^{-2} after 500 cycles is obtained. The fast charging and stable cycling performances are ascribed to the generation of robust and conductive SEI at the Li surface. In addition to fluorinated anions, $LiNO_3$ is another indispensable additive in Li–sulfur batteries.[72] Because of its strong interaction with the Li electrode, specific adsorption in the inner Helmholtz plane generates initial SEI film with the abundance of Li_2O and LiN_xO_y, which produces high-efficiency passivation layer.[110] Moreover, sulfurized[126] and implantable SEIs[143] have been proposed to improve the uniformity of the SEI film.

Beyond the novel formulations of dilute electrolytes, the salt concentration also modulates the Li^+ solvation structure and the interface structure. In detail, when the salt concentration increases, the molar ratio of coordinated solvent/anion decreases. When there are not enough solvent molecules to participate in the formation of primary solvation sheath, anions will tightly coordinate with Li^+ to form contact ion pairs and be preferentially reduced to produce inorganic-rich SEI film. For example, the highly concentrated electrolyte (4 M LiFSI in DME) was designed to produce a polymeric SEI enriched with LiF.[83] As a result, nodule-like Li without dendrites was obtained at 1.0 mA cm^{-2}, in contrast to the needle-like dendrite morphology in 1 M $LiPF_6$–PC electrolyte (Fig. 13e). Furthermore, super-concentrated fluorinated electrolytes, such as 7 M LiFSI in FEC,[76] 10 M LiFSI in DMC[102] and high-concentrated nitrates, such as 1 M LiTFSI + 0.8 M $LiNO_3$ in DOL/DME,[144] have also been proposed to improve the uniformity of SEI for fast Li^+ transport.

Chemical composition. The chemical components of the SEI film are related to the uneven Li deposition. Many studies have stimulated strong interest in the effect of physical nature of the SEI components on dendrite growth.[50,145] To date, it is widely accepted that two important factors play a role in determining the process of Li^+ diffusion in the interphase and suppressing Li penetration into SEI along the vertical direction: its surface energy and diffusion barrier (Fig. 14a).[51] Among inorganic compounds, including layer (LiOH), multivalent (Li_2CO_3, Li_2O) and halide (LiF, LiCl, LiI, LiBr) compounds, Li halides have higher surface energies and lower surface diffusion barriers. Measured battery lifetimes indicate clear linear trend that Li halides have higher Li dendrite suppression than Li_2CO_3 in the SEI film. The surface energy and diffusion barriers of the SEI components are two vital factors that can boost Li^+ migration and suppress dendrite growth.

LiF with a high surface energy has been widely investigated as SEI component.[130,148] The concept of ''critical length'' has been proposed, which represents the minimum Li dendrite length before it becomes stable and begins to grow.[51]

$$L = \frac{2\gamma E}{\pi\sigma^2} \tag{10}$$

where L is the critical Li dendrite length for further growth, γ the interfacial energy when a new SEI/Li interface is formed, σ is the stress at the tip of a crack or grain boundary, which is determined by the external current, and E is the bulk modulus. Based on this equation, at a constant applied current density, the critical length increases with the Li/SEI interfacial energy γ and the bulk modulus E of the SEI film. The surface energy and bulk modulus of different SEI components (LiF, Li_2O, Li_2CO_3, Li_2S, LiCl and Li_3PS_4) have been calculated (Table 3).[51] Among them, LiF has the highest interfacial energy of 73.28 meV $Å^{-2}$, indicating the highest Li dendrite suppression ability. Moreover, LiF also has high bulk modulus (70 GPa) and the highest value of γE (5129 eV $Å^{-2}$ MPa). In this regard, LiF has the strongest ability to suppress Li dendrite growth. Later, after

Table 3 Comparison of interfacial energy γ, Young's modulus E and Li dendrite suppression ability γE of different interphase components[51,146]

Compounds	γ (meV Å^{-2})	E (GPa)	γE (eV Å^{-2} MPa^{-1})
SrF_2	71.24	89.91	6405
LiF	73.28	70	5129
Li_2O	38.70	78	3018
Li_2S	19.01	40	760
Li_2CO_3	59.22	63	3731
Li_3PS_4	−88.92	22	−1956
LiCl	37.55	32	1202

screening the metal fluorides by DFT, it is discovered that SrF_2 has a higher γE value (6405 eV Å^{-2} MPa^{-1}) than LiF (Table 3).[146] Although the interfacial energy of SrF_2 (71.24 meV Å^{-2}) is slightly lower than LiF (73.28 meV Å^{-2}), its larger Young's modulus 89.97 GPa *vs.* 70 GPa results in higher γE value (6405 eV Å^{-2} MPa^{-1}), and experiment confirmed that for SEI rich in SrF_2, the deposited Li was smooth with no obvious dendrite growth on the Li–Sr surface (Fig. 14b).

In addition to the surface energy of the SEI, the barrier to Li^+ diffusion is another crucial factor for accelerating Li atom diffusion. Although LiF can effectively facilitate Li^+ diffusion due to its superhigh surface energy, it has larger Li^+ diffusion barrier than other Li halides. According to DFT, LiCl-rich SEI film is designed, which has low Li^+ diffusion barrier (LiCl: 0.078 eV, LiF: 0.16 eV) at the Li/SEI interface and can be used to produce symmetric Li cells that are stable over 2200 h at 1 mA cm^{-2}.[149] On the basis of first-principles calculations, it is found that nano-diamond has lower diffusion energy barrier (0.05 eV) than Li halides,[147] and experiment shows that during the deposition process, Li^+ tightly adheres to the nano-diamond and reduces local aggregation, contributing to dendrite-free morphology (Fig. 14c).

Growth thickness. The SEI grows as a result of side reactions at the Li/electrolyte interface and stops when its thickness is large enough to block electron tunnelling. Experiments show that its practical thickness on Li anode ranges from a few to several hundreds of nanometers.[50] The thickness can be roughly estimated follows:

$$T(\mathrm{nm}) = \frac{\varepsilon S}{\pi C(3.6 \times 10^{12})} \quad (11)$$

where ε is the dielectric constant, C the capacitance, S the effective surface area and T the estimated thickness of the SEI.

The accurate SEI thickness is difficult to predict because its composition is highly dependent on the electrolyte components and its formation conditions. The critical SEI thickness has been investigated by theoretical simulations,[150] and it is found that only a few nanometers thickness is enough to prevent electron transport when the SEI is perfect crystal (no matter whether Li_2CO_3, Li_3PO_4 or LiF) without pinholes. In practice the SEI thickness does not increase forever because the cell fails when the Li^+ cannot diffuse through it. The diffusion resistance increases with increasing SEI film thickness based on the law of resistance (Fig. 15a):

$$R = \rho\frac{l}{S} \quad (12)$$

where R is the SEI resistance, ρ the electrical resistivity, l the thickness of the SEI film, and S the surface area. LiF has recently gained much popularity for improving the Li cyclability as its protection on Li anode.[65,151] To study its thickness on Li metal, the controlled LiF layer on Li surface was synthesized by the chemical reaction: $2NF_3 + 6Li = 6LiF + N_2$.[152] It is found that the thickness limit of LiF on Li surface is $\approx$50 nm regardless of the reaction time or external temperature. However, the higher overpotential in symmetrical Li cells proved that this 50 nm-thick SEI has larger Li^+ diffusion resistance than the native SEI on Li surface. To simulate the effect of the SEI film on Li deposition, a simple approach is used to produce an implantable SEI whose average thickness is about 14 nm.[143] The implantable SEI is produced by general electroplating method involving pre-cycling in LiTFSI–DOL/DME + 5% $LiNO_3$ electrolyte, and which is mainly composed of organic species ($ROCO_2Li$) and inorganic compounds (Li_3N, $Li_2N_xO_y$, LiF, Li_2S_x and $Li_2S_xO_y$). The dense inorganic layer with appropriate proportions effectively prevents electron transfer and promotes Li^+ diffusion. As shown in Section 3.3.2, anions generate the inorganic-rich SEI film that facilitates Li^+ diffusion. We produce a SEI by the electroreduction of highly concentrated water-in-salt electrolyte (21 M LiTFSI in 1 kg water) (Fig. 15b).[134] By pre-cycling the Cu substrate in this electrolyte, the inorganic-rich SEI with an average thickness of 14 nm is formed (Fig. 15c). Quite distinct from the resistive layer principally composed of solvent-derived organic species, this salt-derived SEI with more LiF and $Li_2S_xO_y$ effectively reduces the overpotential and facilitates uniform Li deposition (Fig. 15d and e). Recently, by incorporating fluorinated 1,4-dimethoxylbutane with 1 M LiFSI, the unique Li–F interaction and high anion content is obtained in the Li^+ solvation sheath.[153] This coordination structure resulted in thin SEI layer (about 6 nm), along with low overpotential and densely-packed Li morphology. Control of the growth thickness of the SEI film is critical for achieving fast Li^+ diffusion.

3.3.3 Solid-state electrolyte. Compared with SEI, solid-state electrolyte plays a similar role in transporting Li^+, but with thicker layer. Current solid-state electrolyte can be divided into two categories: solid inorganic electrolyte and solid polymer electrolyte. Compared with liquid electrolyte with high ionic electrolyte (about 1–10 mS cm^{-1}), solid inorganic electrolyte usually has low ionic conductivity, such as garnet-structured $Li_6BaLa_2Ta_2O_{12}$: 4×10^{-2} mS cm^{-1}, Li phosphorus oxynitride (LiPON): 2×10^{-3} mS cm^{-1}, $Li_{10}GeP_2S_{12}$: 12 mS cm^{-1} at room temperature, for Li^+ transport.[154] In general, solid inorganic electrolyte has a periodic structure with coordinated polyhedrons. The interstices, vacancies and grain boundary principally contribute to ion transport. In addition, the bravais lattice of the crystal framework also determines the ion transport barrier. Compared with face-centered cubic or hexagonal close-packed lattice, body-centered cubic packing of the anion affords a lower energy barrier for ion transport.[155] For the present, the most promising Li^+ conducting oxide is stoichiometric $Li_7La_3Zr_2O_{12}$, owing to its high Young's modulus >140 GPa, high ionic conductivity $>10^{-1}$ mS cm^{-1}, strong oxidation stability >6 V and chemical stability against Li metal.[156] Dopant is one of the most effective strategies to increase ionic conductivity. For example,

with addition of Ta^{5+} to $Li_7La_3Zr_2O_{12}$, $Li_{6.5}La_3Zr_{1.5}Ta_{0.5}O_{12}$ obtains high Li^+ conductivity close to 1 mS cm^{-1} at room temperature.[157] However, it is found that dendrite still forms in the bulk of $Li_7La_3Zr_2O_{12}$ electrolyte. This behavior contradicts the conventional understanding that the dendrite can be remitted when the Li^+ transference number close to 1 or the shear modulus beyond twice of Li. By monitoring the dynamic evolution of Li concentration profile in the cell of $LiCoO_2$‖LiPON‖Cu, Li‖$Li_7La_3Zr_2O_{12}$‖Cu and Li‖Li_3PS_4‖Pt, it is found that dendrite can form inside $Li_7La_3Zr_2O_{12}$ and Li_3PS_4 electrolyte, rather than in LiPON.[158] The different electronic conductivities of three electrolytes can explain this behavior. Compared to the low electronic conductivity of LiPON (10^{-9}–10^{-12} mS cm^{-1}), $Li_7La_3Zr_2O_{12}$ (10^{-4}–10^{-5} mS cm^{-1}) and Li_3PS_4 (10^{-5}–10^{-6} mS cm^{-1}) exhibit much larger electronic conductivity, which allow Li^+ to get electrons and form dendrite inside the electrolyte. This growth model is different from the conventional interface-controlled dendrite growth that dendrite grows from anode to cathode. Therefore, lowering the electronic conductivity is critical for the application of $Li_7La_3Zr_2O_{12}$ electrolyte in Li metal batteries. Besides, the high interfacial resistance provides a serious challenge for $Li_7La_3Zr_2O_{12}$. There are many strategies to address this issue by depositing wettable lithiophilic layer between Li and $Li_7La_3Zr_2O_{12}$. For example, Si-modified $Li_7La_3Zr_2O_{12}$ can achieve a 7-fold decrease in the interfacial impedance compared to $Li_7La_3Zr_2O_{12}$.[159] $Li_{10}GeP_2S_{12}$ has been considered ultrafast Li^+ conductor with ultrahigh ionic conductivity of 12 mS cm^{-1}.[160] In addition, the high Young's modulus (37 GPa)[161] and high oxidation stability of 4 V make it promising for Li metal batteries. Nevertheless, its sensitive fresh Li produces unstable interface between the electrode and $Li_{10}GeP_2S_{12}$. In an ideal case, the formed interfacial layer presents high Li^+ conductivity and low electronic conductivity for facile Li^+ transport and minimizing the continuous reduction of solid inorganic electrolyte. For $Li_{10}GeP_2S_{12}$, the interfacial layer is electronically conductive. This behavior gives rise to electron transport at the interface and induces continuous degradation of solid inorganic electrolyte with high resistance. To address this issue, nanocomposite of organic and inorganic Li salts are used to stabilize the interface.[162] Such nanocomposite has two merits: (1) the interface contains stable inorganic products (LiF and Li_2O) for the enhancement of electrochemical and chemical stability towards Li reduction; (2) the *in situ* formed interface has better affinity between Li and electrolyte, resulting in low interfacial resistance. The use of this nanocomposite interface enables stable Li plating/stripping cycling over 3000 h.

Solid polymer electrolyte is prepared by dissolving Li salts into the polymer matrix. Compared with solid inorganic electrolyte, solid polymer electrolyte has higher flexibility and elasticity to accommodate the volume expansion, better processability, better compatibility with Li and lower interfacial resistance. PEO-based electrolyte has been widely studied for stable interfacial stability and good thermal properties. However, critical problem of PEO-based electrolyte is the low Li^+ conductivity (10^{-3}–10^{-5} mS cm^{-1}) at room temperature.[163] Different from solid inorganic electrolyte, solid polymer electrolyte conducts Li^+ through the segmental relaxation of the polymer chains. The low Li^+ conductivity in solid polymer electrolyte has long been considered the contribution of amorphous phase above the glass transition temperature T_g, rather than the crystalline phase.[164,165] The dynamic and disordered motion of polymer chain promote ion transport. Nevertheless, another viewpoint points out that conductivity depends more on crystalline domains.[166] For the present, the consensus has been reached that reducing crystallinity is key to increase Li^+ conductivity in polymer electrolytes. Notably, most polymers possess low dielectric constants (dielectric constant <5) and it is difficult to dissociate the ion-pair of salt for efficient cation transport.[154] To improve the ionic conductivity, the rational combination of solid inorganic electrolyte and solid polymer electrolyte is pathway to balance the disadvantage of the high interfacial resistance in solid inorganic electrolyte and low Li^+ conductivity in solid polymer electrolyte. Such hybrid inorganic/polymer electrolyte can not only improve the mechanical stability, but also regulate the interfacial compatibility with Li anode. In general, the hybrid inorganic/polymer electrolyte consists of polymeric/Li salt host and dispersed inorganic fillers. According to Chazalviel model, Li dendrite can be remitted by anions immobilization.[167] To immobilize anions in solid polymer electrolyte, an effective strategy is to blend inorganic fillers. The inorganic fillers have two merits: (1) enhance the mechanical strength to block the dendrite volume expansion; (2) reduce the crystallinity of polymer for high ionic conductivity. For example, the anion-immobilized solid-state electrolyte composed of garnet-type $Li_{6.75}La_3Zr_{1.75}Ta_{0.25}O_{12}$ ceramic particles in PEO–LiTFSI is designed to protect Li anode.[168] $TFSI^-$ in the electrolyte is tethered by polymer matrix and inorganic fillers, which induces high Li^+ transference number 0.58 and high Li^+ conductivity 1.12×10^{-2} mS cm^{-1}, in contrast to PEO electrolyte (Li^+ transference number: 0.37, Li^+ conductivity: 10^{-3}–10^{-5} mS cm^{-1}). Such anion-immobilized inorganic–polymer electrolyte induces uniform Li^+ distribution and produces dendrite-free morphology. Li polysulfide is a fast ionic conductor due to its high polarizability of sulfide ions that weaken the interaction between anions and Li^+.[169] By *in situ* polymerization of Li polysulfides into the PEO chains, fast Li^+ transport is enabled through the intermolecular interactions.[170] In contrast to PEO electrolyte, the polysulfide-modified PEO exhibits higher Li^+ transference number 0.61. Such high Li^+ transference number prolongs the Sand's time and achieves smooth Li deposition without dendrite formation.

Solid-state electrolytes (inorganic, polymer or hybrid) with high ionic conductivity, strong mechanical strength, low interfacial resistance, stable interfacial stability and low electronic conductivity are desired. Importantly, the thickness of the solid-state electrolyte should be controlled to enable high-energy-density output.

3.4 Li atom migration in the bulk base

During Li deposition, dendrites grow easily in present electrolyte systems, which contrasts with the dendrite-free morphology for Mg^{2+} deposition on an electrode surface.[171,172] DFT calculations show that Mg–Mg has higher bond strength than Li–Li, indicating that Mg has higher free energy difference between high-dimensional and low-dimensional phases.[173] This difference in

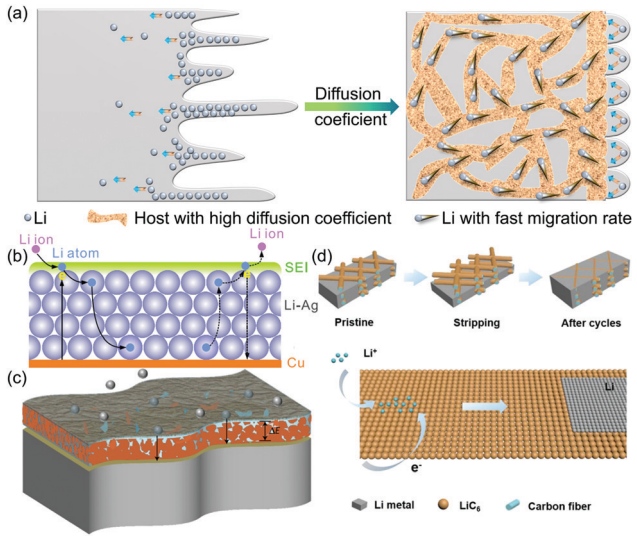

Fig. 16 (a) Scheme of host with high diffusion coefficient provides more paths to facilitate fast Li atom migration. (b) Schematic of Li–Ag alloy structure on facilitating fast Li atom diffusion. Reproduced with permission from ref. 176. Copyright 2020, American Chemical Society. (c) Schematic depicting the function of the alloy-protected Li anode. Reproduced with permission from ref. 177. Copyright 2018, Nature Publishing Group. (d) Schematic for the process of adsorption of Li^+ and charge transfer on LiC_6 layer to form uniform Li deposits. Reproduced with permission from ref. 178. Copyright 2019, Wiley-VCH.

bond strength causes Mg to deposit with high-dimensional structures rather than one-dimensional dendritic whiskers. As a result of in-depth research on Li, Na and Mg metal anodes, it is found that surface diffusion on Mg electrode is rapid compared to that on Li and Na electrodes, which indicates that Mg^{2+} has higher tendency to deposit on nearby sites rather than on lumped area to form dendrites.[30] The diffusion coefficient of Mg atom in bulk Mg metal is around 10^{-8}–10^{-9} cm^2 s^{-1}, which is faster than that of Li atom in bulk Li metal (5.7×10^{-11} cm^2 s^{-1}).[31,32]

Owing to the low self-diffusion coefficient of Li atoms, Li dendrites grow quickly at protuberances (Fig. 16a).[174,175] A highly effective strategy to boost the Li atom migration can be realized by host materials with high Li atom diffusion coefficient. For example, Li–Ag alloy has high Li diffusion coefficient (around 10^{-8} cm^2 s^{-1}), which facilitates freshly generated Li atoms moving from the highly electron-conductive surface to the inside of the alloy foil (Fig. 16b).[176] The homogeneously distributed Ag particles not only reduce the nucleation overpotential, but produce uniform Li deposition morphology. To improve the Li atom diffusion coefficient, a surface film comprised of Li-based compounds ($Li_{13}In_3$, 10^{-8}–10^{-6} cm^2 s^{-1}, LiZn, 4.7×10^{-8} cm^2 s^{-1} and Li_3Bi, 3×10^{-6} cm^2 s^{-1}) is synthesized by reduction of metal chlorides with Li at room temperature (Fig. 16c).[177] This unique protection layer promotes fast Li atom migration and give an extended cycling life of 1, 400 h in symmetric cells at 2 mA cm^{-2}. In addition to Li-alloy substrate, carbon materials with high electron conductivity, high surface area, low relative molecular mass and good lithiophilic nature have been exploited as a stable scaffold for the Li anode. On the basis of transition state theory, the diffusion coefficient of LiC_6 scaffold is in the range of 10^{-7}–10^{-12} cm^2 s^{-1}.[174] A LiC_6 layer with strong lithiophilicity and fast Li atom diffusion gives uniform Li deposition, along with good cycling stability during repeated Li plating/stripping processes (Fig. 16d).[178] Layered reduced graphene oxide (rGO) has been reported as a stable host for Li anode.[179] In addition to fast Li atom diffusion 7×10^{-5} cm^2 s^{-1},[180] it provides layer structure, which provides stable scaffold with high surface area that reduces the volume changes during Li plating/stripping, and excellent lithiophilicity, which guarantees uniform Li atom diffusion for homogeneous Li deposition morphology. Other carbon materials, such as nanotubes and amorphous carbon, have also been widely studied for use in the Li anodes.[104,181]

4. Dense growth

Whether the deposition morphology is mossy or dendritic, low CE and large volume expansion are two detrimental factors during the Li growth. On account of the lowest electronegative nature, Li metal can react with all polar-aprotic electrolytes to form the SEI layer (Fig. 17). When the dendrite grows as the increased deposition capacity, the fragile SEI is easily ruptured by the volume change, exposing fresh Li to the electrolytes and forming newer SEI on the dendrite surface. As a result, the SEI film experiences repeated cracking and reconstruction, which irreversibly consumes the Li and electrolyte for low CE and induces dead Li. In addition, Li metal is hostless material, which suffers from large volume change as the increased deposition capacity. After repeated plating/stripping processes, porous Li deposits form and further exacerbate the volume expansion. Such volume fluctuation can fracture the SEI, crack the battery configuration and finally short-circuiting the battery. Therefore, the low CE and large volume expansion are two issues to be firstly addressed for dense Li growth.

4.1 Anode CE

The stability of SEI principally determines the anode CE. It is reasonable that great efforts are devoted to constructing *in situ* or *ex situ* SEI with negligible electronic conductivity, high Li^+ conductivity, electrochemical stability and favorable mechanical strength. *In situ* formation of protection layer on Li anode is generally obtained by tailoring the electrolyte components, such as solvent, salt and additive. *Ex situ* formation of artificial SEI coating on Li anode, usually provides controllable thickness, mechanical strength and flexibility. In this section, the electrolyte-derived (*in situ*) and artificial SEI coatings (*ex situ*) on the effect of CE are summarized (Fig. 18).

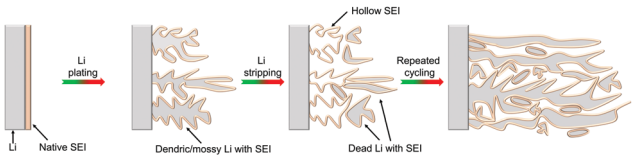

Fig. 17 Schematic of the Li growth process during the repeated cycling.

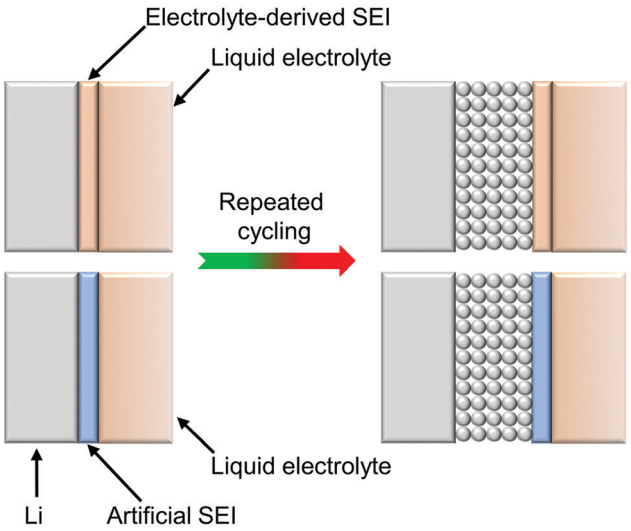

Fig. 18 Schematic of the uniform Li deposition with the protection of electrolyte-derived or artificial SEI. The building blocks of electrolyte-derived SEI are derived from the chemical or electrochemical decompositions of solvent, anion and additive in the electrolyte. Therefore, the electrolyte composition plays a critical role in determining the physicochemical properties of SEI.

4.1.1 Electrolyte-derived SEI. The electrolyte-derived SEI are principally derived from the chemical or electrochemical decomposition of solvent, anion and additive in the electrolyte. In this section, the common and emerging solvent, anion and additive on the effect of *in situ* SEI formation are summarized.

Solvent. Although ester electrolytes are widely used in state-of-the-art LIBs, they typically give rise to poor electrochemical performance of Li metal batteries. In dilute ester electrolyte (<1.2 M), the deposition morphology in alkyl carbonates (EC, PC, DMC, DEC) exhibits dendritic structure.[99] Such dendritic morphology is inclined to grow along the vertical direction, which not only fractures the SEI and results in low CE (<90%), but also pierces through the separator and induces safety issues. The growth of dendrite in ester electrolyte is generally ascribed to non-uniform SEI. For 1 M $LiPF_6$ EC/DEC, the ratio of $Li^+ : PF_6^- :$ solvent = 1 : 1 : 11.6.[95] During SEI formation, such a high proportion of solvent molecules produces solvent-dominated SEI with more organic species (ROLi, RCO_2Li and $ROCO_2Li$), along with a few inorganic species (Li_2O, Li_2CO_3 and LiF). Owing to the most electronegative nature of Li, the organic species of SEI are chemically unstable towards Li and tended to be reduced to form stable inorganic species. Therefore, the organic species principally distribute in the outer layer of SEI and inorganic species mainly in the inner layer. The non-uniform SEI induces notorious dendrite growth along the direction that has the lowest ion resistance, which cracks the SEI film and results in low CE. The substitution of conventional ester with novel ester is an effective strategy to manipulate the SEI for high CE. Cyclic ester vinylene carbonate (VC), with double bond and high reduction potential, proves the validity of this strategy.[182] In 1 M $LiPF_6$–VC, the deposition morphology is uniform and round, and no dendrites are observed. Such distinct morphology is ascribed to the polymerization of VC on Li anode and enhances the stability of SEI, resulting in stable CE of 97%.[183] The rational fluorination of present ester solvent emerges as an effective strategy to regulate the SEI formation and Li deposition. FEC is a representative fluorinated ester that generates LiF-rich SEI for uniform Li deposition and high CE.[73] LiF has been thought a key component of the SEI for its excellent electron-insulating ability.[184,185] It is also proved that LiF benefits Li^+ conductivity at the Li_2CO_3/LiF interface.[186,187] For 1 M $LiPF_6$–FEC, the average CE of 98% is obtained.[183] An all-fluorinated electrolyte composed of 1 M $LiPF_6$–FEC/FEMC/HFE is designed and enables high CE of 99.2% (Fig. 19a).[56] When coupled with $LiNi_{0.8}Co_{0.1}Mn_{0.1}O_2$ (NCM811) cathode, 90% retention of initial discharge capacity is obtained after 450 cycles.

Ether with good wettability and low viscosity is another class of frequently used solvent in Li metal batteries. In ether electrolytes, high CE, such as 1 M $LiAsF_6$–DOL (98%)[188] and 1 M $LiAsF_6$ 2-methyltetrahydrofuran (97%),[189] 1 M LiFSI–DME (97%)[110] and round Li deposition morphology can be achieved. The deposition behavior and high CE are explored by both experiment and calculation.[190] It is found that cyclic DOL and acyclic DME perform different mechanisms. The SEI in DOL-based

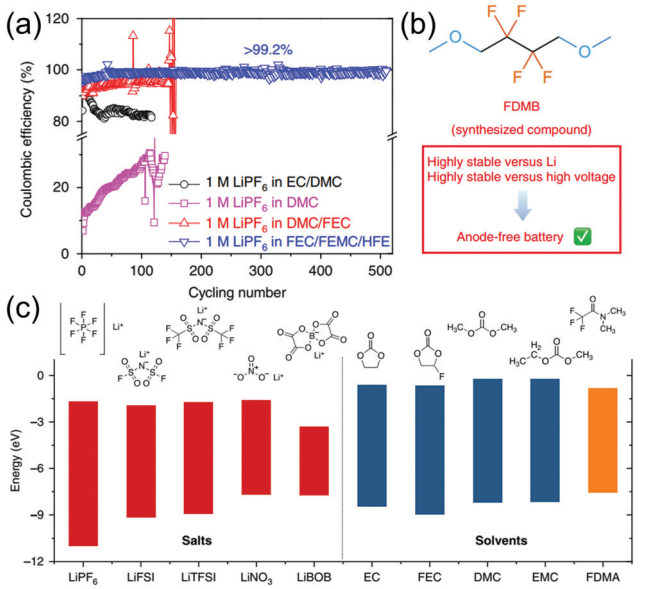

Fig. 19 (a) Li plating/stripping CE in different electrolytes at 0.2 mA cm^{-2} with capacity of 1 mA h cm^{-2}. EC: ethylene carbonate; DMC: dimethyl carbonate; $LiPF_6$: lithium hexafluorophosphate; FEC: fluoroethylene carbonate; FEMC: 3,3,3-fluoroethylmethyl carbonate; HFE: 1,1,2,2-tetrafluoroethyl-2′,2′,2′-trifluoroethyl ether. Reproduced with permission from ref. 56. Copyright 2018, Nature Publishing Group. (b) Design scheme of the molecular structure of FDMB. FDMB: fluorinated 1,4-dimethoxylbutane. Reproduced with permission from ref. 153. Copyright 2020, Nature Publishing Group. (c) Comparison of the HOMO–LUMO energy levels for the used Li salts and solvents. LiFSI: lithium bis(fluorosulfonyl)imide; LiTFSI: lithium bistrifluoromethanesulfonimide; LiBOB: lithium bis(oxalate)borate; EMC: ethyl methyl carbonate; FDMA: 2,2,2-trifluoro-*N*,*N*-dimethylacetamide. Reproduced with permission from ref. 194. Copyright 2020, Nature Publishing Group.

electrolyte is layer-structured, with outer organic/polymeric layer consisting of lithium oligoethoxides with C–C–O or O–C–O linkages and inner layer of inorganic oxides Li_2O. Such SEI minimizes the side reactions between Li and electrolyte for high CE. On the other hand, despite the preferential solvation by Li^+, the acyclic DME remains very stable against reduction even at the potential of Li^+ plating.

1,4-Dioxane, homologue of DOL, is employed as cosolvent for its high oxidation tolerance.[191] In this electrolyte, more inorganic dense SEI forms and thus enables high CE of 98%. Although the common ethers can achieve high CE and less-dendritic morphology, the low oxidation stability (<4 V) greatly hinders their application in high-voltage Li metal batteries. Crown ether (15-crown-15) with high oxidation ability, is induced to 1 M $LiPF_6$–EC/DMC. Benefitting from the strong complex effect between Li^+ and crown, the Li^+/crown complexes isolate the carbonate molecules and are preferentially reduced to form dense SEI layer, as well as uniform Li deposition.[243] The obviously enhanced cycling performance over 200 cycles in $LiNi_{0.6}Co_{0.2}Mn_{0.2}O_2$ (NCM622)‖Li cells is also achieved. Introduction of fluorine groups to the common ether DME is another strategy to enlarge the oxidation window and maintain good compatibility with Li metal. By incorporation of $-CF_2-$ units to DME, fluorinated 1,4-dimethoxylbutane is synthesized (Fig. 19b).[153] When paired with 1 M LiFSI, this electrolyte not only endows Li metal with thin SEI (about 6 nm) and high CE of 99.52%, but also enables high oxidation stability over 6 V. Industrial anode-free pouch cells delivered about 325 W h kg^{-1} single-cell energy density and 80% capacity retention after 100 cycles.

Amide compounds, such as dimethylacetamide (DMA) and *N*,*N*-dimethylformamide (DMF), are similar to esters except the functional groups that the substitution of $-OR_2$ ester group with $-NR_2$ amide group. Due to the strong oxidation tolerance against high voltage, amides are considered the candidate for Li–O_2 batteries.[192] However, the serious instability of Li anode in DMA-based or DMF-based electrolytes continuously consumes the electrolyte and active Li, accelerating the failure of the cell. To revive the DMA-based electrolyte in Li metal batteries, regulation of the SEI film with high concentration of $LiNO_3$ is favorable. $LiNO_3$ has high solubility in the amide electrolytes and it can produce a stable SEI to prevent the side reactions between Li and amide solvent. With the optimized electrolyte formulation 2 M LiTFSI + 1 M $LiNO_3$–DMA, this electrolyte stabilizes the Li anode by forming a SEI with abundance of LiF/LiN_xO_y, along with fast mass transfer kinetics.[193] In consideration of the instability of amide compound, 2,2,2-trifluoro-*N*,*N*-dimethylacetamide (FDMA), substitution of $-CH_3$ with $-CF_3$ group, can not only improve the LUMO levels to participate in SEI formation at high reduction potential, but also induce repulsive force towards the C═O dipole for strong oxidation stability (Fig. 19c).[194] In the electrolyte of 1 M LiTFSI–FDMA/FEC (1 : 1 by volume), favourable SEI with high ionic conductivity and high stability is produced. With high loading of NCM811 (3.5 mA h cm^{-2}), such SEI enables an average CE of 99.3% and outstanding capacity retention.

In view of the highly flammable nature of ester, ether and amide, organic phosphate is a good option for safe Li metal batteries because of the flame-retarding ability and low cost.[41] Nevertheless, poor compatibility with the Li anode restricts the practical application. To address this issue, high salt/solvent electrolytes are used. In the concentrated electrolyte, solvent molecules principally participate in the Li^+ solvation sheath, which effectively suppresses the reactivity of phosphate towards Li anode. In high ratio of 1 : 2 LiFSI to TEP (about 2.2 M), non-dendritic Li deposition morphology with high CE over 99% is achieved in Li‖Cu cells.[195] With the optimization of the salt/solvent ratio, it is found that LiFSI : TEP = 1 : 1.5 exhibits the best performance with extremely high CE of 99.3% over 350 cycles. Considering the high viscosity of high-concentrated electrolyte, bis(2,2,2-trifluoroethyl)ether with low viscosity dilutes the high-concentrated electrolyte (3.2 M LiFSI–TEP) and forms close to 1 M salt concentration, without sacrificing the CE ($>99\%$).[196] Except the strategy of high-concentrated electrolyte, the nitriding interface through manipulation of $LiNO_3$ with organic phosphate is used to ameliorate the incompatibility.[197] With the addition of $LiNO_3$, the Li growth behavior changes from nanosized dendritic morphology to nitriding interface dominated dendrite-free shape, along with an average CE of 97.3%. Moreover, 94.7% capacity retention is achieved after 200 cycles when paired with NCM622 cathode.

In addition, sulphate,[59] sulfone,[86,198] nitrile[199] and ionic liquids[200] are widely explored to improve the CE and suppress dendrite formation. As discussed above, it should be noted that state-of-the-art electrolytes are far from the requirement CE ($>99.9\%$) for practical application of Li anode. Future efforts are needed to exploit novel nonaqueous electrolytes with high CE and long lifespan.

Salt. Apart from the solvent, Li salt is another indispensable component in the liquid electrolyte and serves as the main source of inorganic species during SEI formation. Nine frequently-used Li salts, including $LiPF_6$, LiTFSI, $LiBF_4$, $LiClO_4$, $LiAsF_6$, LiI, $LiCF_3SO_3$, LiBOB and LiDFOB, are systematically investigated with 1 M salt concentration in PC.[183] It is found that the component and size of salt anion produce different SEI structures and Li deposition morphologies. Notably, the electrolyte containing LiBOB exhibits high CE > 90%, which is ascribed to the high reduction potential of LiBOB that forms B-containing SEI.[139] To improve the inorganic contents in the formed SEI, Li salts with high reduction potential are studied. Based on DFT calculations, it is found that LiTFA possesses higher LUMO energy than the conventional solvents and salts (LiTFA > $LiPF_6$ > FEC > EC > DEC > DME), indicating that LiTFA has a higher tendency to be reduced during SEI formation.[95] When 1 M LiTFA is added to the DME/FEC (7 : 3 by volume) electrolyte, TFA^- is preferentially reduced to produce stable SEI with uniform distribution of LiF and Li_2O. Such SEI contributes to fast ion transfer kinetics and uniform Li deposition morphology with a high CE of 98.8%. Fluorinated sulfimides, such as $TFSI^-$ and FSI^-, are another class of anions that possess high solubility, low viscosity and fast ion conduction. Especially, compared with the strong binding energy C–F in $TFSI^-$,

S–F bond in FSI^- has a high tendency to break and form LiF-rich SEI. Such LiF-rich SEI achieves excellent CE and greatly suppresses the dendrite formation.[110] Following, LiHFDF with fluorination and unsaturation in its structure, is introduced into DOL/DME (1 : 1 by volume) electrolyte for Li–S battery (Fig. 20).[142] Such salt forms highly fluorinated interphase at both anode and cathode surfaces, which effectively suppresses formation of Li dendrite and dissolution/shuttling of polysulfides. Furthermore, the suitable combination of two types of Li salts has also proved to improve the anode CE.[201,202]

In general, the concentration of Li salt is smaller than 1.2 M to balance the electrolyte viscosity, ionic conductivity and cost. Concentrated ester electrolyte (>3 M), which possesses the advantages of high oxidation stability, Al anticorrosion, high Li transference number and low volatility, has become the most promising solution for Li metal batteries. In concentrated electrolyte, more anions participate in the Li^+ solvation sheath and shift the LUMO energy level from solvents to anions. During the SEI formation, the coordinated anions are preferentially reduced to form the inorganic-rich SEI. 4 M LiFSI–DME,[83] 1–7 M LiTFSI–DOL/DME[78] and 10 M LiFSI–EC/DMC[102] exhibit outstanding performance by forming LiF-rich SEI on Li anode. For 10 M LiFSI–EC/DMC (1 : 1 by volume), a round-shaped morphology with dense and uniform structure is obtained, rather than needle-like Li in 1 M LiFSI–EC/DMC. Such morphology with low specific surface areas reduces the side reactions and produces high CE about 99.2% at 0.2 mA cm^{-2}. Despite the appealing performance of high-concentration electrolyte, poor wettability and high viscosity hinder industrial applications. To address this issue, localized high-concentration electrolyte is developed to dilute the high-concentration electrolyte 5.5 M LiFSI–DMC to 1.2 M.[203] This dilute electrolyte enables dendrite-free deposition morphology with high CE of 99.5% and delivers >80% capacity retention after 700 cycles in $LiNi_{1/3}Co_{1/3}Mn_{1/3}O_2$ (NCM111)‖Li cells.

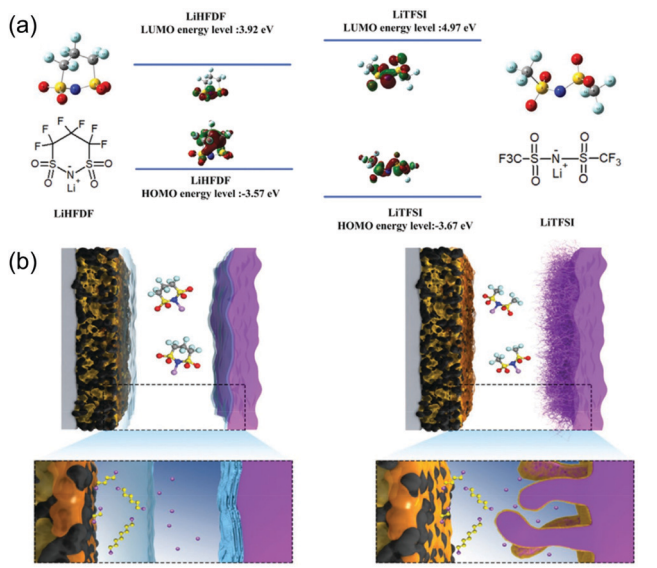

Fig. 20 (a) Molecular structure, molecular model, and HOMO and LUMO energies of LiTFSI and LiHFDF. (b) Schematic of the Li dendrite suppression by LiTFSI and LiHFDF. LiTFSI: lithium bistrifluoromethanesulfonimide; LiHFDF: 1,1,2,2,3,3-hexafluoropropane-1,3-disulfonimide. Reproduced with permission from ref. 142. Copyright 2020, Wiley-VCH.

Additives. Apart from the solvent and salt, additives have been considered the vital component of the electrolyte to enhance the uniformity and stability of pristine SEI. In general, the content of electrolyte additives is less than 5–10% either by volume or weight percentage to balance the performance and cost. During SEI formation, additives with high reduction potential or specific adsorption in the inner Helmholtz layer are preferentially reduced than solvent and salt to form dense SEI with favourable components. Such dense SEI plays a great role in the Li deposition morphology and suppression of side reactions between Li and electrolyte. In this section, the recent progress of solvent and salt additives is summarized.

(1) Solvent analogues: FEC and VC are analogues similar to the structure of EC. VC can form a polycarbonate-based SEI film through reductive polymerization.[204] When addition of VC as additive in highly corrosive AN-based electrolyte, high CE of 99.2% is achieved at current density of 0.2 mA cm^{-2}.[199] Benefitting from this SEI, NCM622‖Li cell with high cathode loading of 4 mA h cm^{-2} keeps stable cycling over 200 cycles at 2 mA cm^{-2}. FEC, by substitution one hydrogen with fluorine, is another beneficial additive for robust SEI formation on Li anode. First-principles calculations show that FEC has lower LUMO energy (−0.87 eV) than EC (−0.38 eV) and DEC (0 eV), indicating that FEC decomposes and forms the SEI prior to routine solvents.[135] During the SEI formation, the C–F bond in FEC is first broken around 340 fs and forms LiF due to the strong electrostatic attraction between positive Li^+ and negative F^-. The presence of nanostructured LiF particles produce compact and stable SEI, and thus renders significantly improved CE of 98% in Li‖Cu cells and uniform Li deposition morphology. When high-loading $LiNi_{0.5}Co_{0.2}Mn_{0.3}O_2$ (NCM523) cathode is used, this electrolyte delivers high initial capacity of 154 mA h g^{-1} at 180 mA g^{-1}. Besides FEC additive, F-containing organic solvent, such as tris(2,2,2-trifluoroethyl)borate[205] and 2-fluoropyridine,[206] are introduced to electrolyte to improve the performance of Li anode.

(2) Li salts: Li salt is considered an effective additive for regulating the inorganic components in the SEI film. $LiNO_3$ is a widely used salt additive in ether-based Li–S batteries to prevent the shutting effect of polysulfide intermediates and protect Li anode from the parasitic reactions. Due to its high reduction potential (1.7 V), $LiNO_3$ is firstly reduced into insoluble Li_3N and LiN_xO_y on Li surface. Importantly, the Li deposition morphology can be changed to spherical shape with the addition of $LiNO_3$. However, $LiNO_3$ has extremely low solubility in ester electrolyte, which limits its application in high-voltage batteries. To increase the solubility, an effective solvation strategy is developed.[207] With adding of trace amounts of CuF_2 as the dissolution promoter, Cu^{2+} in CuF_2 tends to coordinate with NO^{3-} to form Cu^{2+}–NO^{3-} complex (Fig. 21a). Such complex can improve the solubility of $LiNO_3$ in EC/DEC electrolyte and produces conductive SEI with decomposition

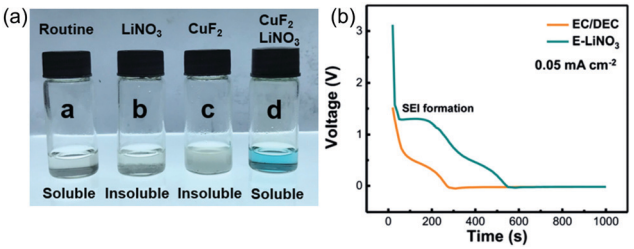

Fig. 21 (a) Optical images of electrolytes with different components. Here, 0.2 wt% CuF_2 enables solubility of 1 wt% $LiNO_3$ in ester-based electrolyte. Routine: 1 M $LiPF_6$–EC/DEC. (b) Galvanostatic voltage profiles of Li depositing onto the Cu substrate in the 1 M $LiPF_6$ EC/DEC and 1 M $LiPF_6$ EC/DEC + 1 wt% $LiNO_3$ + 0.2 wt% CuF_2. Reproduced with permission from ref. 207. Copyright 2018, Wiley-VCH.

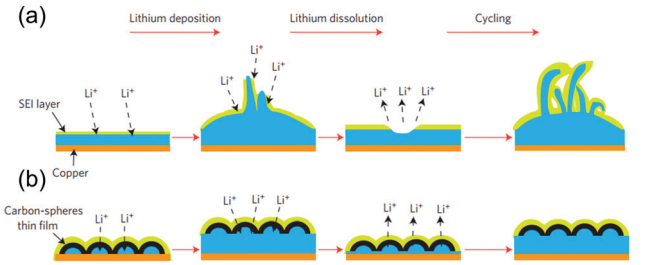

Fig. 22 (a) Schematic of the Li deposition on bare Cu substrate. (b) Schematic of the Li deposition on modified Cu with the hollow carbon nanospheres. Reproduced with permission from ref. 104. Copyright 2014, Nature Publishing Group.

potential about 1.4 V (Fig. 21b). In contrast to the dendritic Li in EC/DEC electrolyte, the $LiNO_3$-based electrolyte induces uniform Li deposition with high CE, low interface resistance and long cycling lifespan. Introduction of cosolvent that has high $LiNO_3$ solubility to ester electrolyte is another effective strategy. In general, solvent with high donor number has good solubility with $LiNO_3$. GBL, with high donor number of 18 kcal mol^{-1}, is added to 1 M LiFSI–FEC (GBL : FEC = 2 : 1 by volume) electrolyte and enables the solubility of $LiNO_3$ over 0.5 M.[74] Remarkably, the electrolyte with high concentration of $LiNO_3$ presents average CE of 98.8%. In view of sulfide species that have high ionic conductivity (about 0.1 mS cm^{-1}), lithium polysulfide (Li_2S_x) was introduced 1 M LiTFSI–DOL/DME electrolyte.[126] Compared with the routine SEI, almost one magnitude higher ionic conductivity is obtained when forming sulfurized SEI. With the protection of such SEI, Li anode exhibits a high CE of 98% over 200 cycles at 1 mA cm^{-2}. B-Containing additive, such as LiBOB[208] and LiDFOB,[209] is another class of attractive salt because its lower LUMO energy than $LiPF_6$, EC and EMC, leading to preferential decomposition to form protective layer on Li anode.

4.1.2 Artificial SEI coating. In consideration of fragile SEI formed in organic electrolytes, the SEI usually fractures as a result of volume expansion during Li deposition, exposing fresh Li to electrolytes for further side reactions. Artificial SEI coating with strong mechanical strength is proposed to avoid the disadvantages of the electrolyte-derived SEI. For the present, carbon material, polymer and inorganic layer are the general choices of artificial SEI coating.

Carbon materials. Owing to the excellent chemical stability, strong mechanical strength, low relative molecular weight and tunable nanostructure, carbon material is an ideal choice as artificial SEI coating. To protect the Li anode, a flexible, interconnected and hollow amorphous carbon nanosphere coating is designed (Fig. 22).[104] This artificial SEI coating has three advantages: (1) it is chemically and electrochemically stable against Li metal; (2) this thin amorphous carbon has a thickness of 20 nm, but high Young's modulus is about 200 GPa for suppressing dendrite growth; (3) the top surface of amorphous carbon is highly insulating but the bulk has high ionic conductivity 7.5 mS cm^{-1}, resulting in direct Li deposition onto the inner cavity. When Li deposits on the surface of the current collector, the amorphous carbon nanosphere is elevated and functions as the SEI film for protecting Li anode. In contrast to rapid growth of metal filaments and dendrites on bare Cu substrate, the modified Cu with hollow carbon nanospheres effectively accommodates the volume expansion and prevents the direct contact between Li and electrolyte (Fig. 22a and b). As a result, high CE of 99.5% at 0.25 mA cm^{-2} over 150 cycles is obtained. Similar to the amorphous carbon nanospheres, GO can also lead to superior cycling stability and high CE. With electrically insulating, high ionic conductivity about 10^{-2} S cm^{-1}, excellent mechanical strength (Young's modulus varies from 380 to 470 GPa) and superior flexibility, GO is considered good artificial SEI coating for Li anode.[210] Benefitting from the GO-coated artificial SEI, uniform Li deposition with an average CE of 98% is achieved.

Polymer. Polymer, with high flexibility, diversity, cross-linked networks and tunable chemical reactivity, is another class of choice for artificial SEI coating on Li metal. It is worth noting that polymers usually have extremely low Li^+ conductivity and cannot conduct Li^+ ions. For example, poly(dimethylsiloxane) (PDMS) is widely used in microfluidic field for strong chemical inertness. However, it cannot directly be used as the protective layer because it is not Li^+ conductor.[211] To provide pathways for Li^+ transport, acid treatment by HF is employed and nanopores with controllable size are obtained. The nanopores of PDMS allow efficient Li^+ transport and achieve high CE of 94.5% in corrosive ester electrolyte. To enable fast ion conductor, inorganic salt $LiNO_3$ is added to the polymer precursor of ethyl α-cyanoacrylate.[212] The poly(ethyl α-cyanoacrylate) with excellent mechanical strength (>25 GPa) serves as the outer layer to prevent the contact between Li and electrolyte. The inner layer contacting Li is directly reduced and forms a homogeneous interface layer, facilitating fast Li^+ conduction. With the protection of this artificial SEI coating, high capacity retention of 93% is obtained at 2C rate. Despite the common polymeric protective layers enhancing the anode performance, most of them only sustain a few hundred cycles and fail due to the volume expansion. To address the dynamic volume change during Li plating/stripping process, self-adapting artificial SEI is designed by Li

polyacrylic acid (LiPAA) with high stretchability (582% strain to its initial strength).[213] This flexible artificial SEI coating with high-binding ability can inhibit the side reaction between Li and air, and thus realize stable Li plating/stripping over 700 h. To achieve stable cycling at high current density with long lifespan, the self-healable supramolecular copolymer comprising of pendant poly(ethylene oxide) segments and ureido-pyrimidinone quadruple-hydrogen-bonding moieties, is designed as a robust artificial SEI layer.[214] This protective layer provides fast and homogeneous Li^+ transport pathways, achieves stable Li plating/stripping at high current density of 20 mA cm^{-2} over 4000 cycles.

Inorganic materials. Inorganic artificial SEI coatings are usually with strong mechanical strength. The artificial Li_3PO_4 SEI layer, through the *in situ* reaction of polyphosphoric acid with Li metal, exhibits promising potential to suppress Li dendrites for its high mechanical strength (10–11 GPa).[215] LiF has been regarded as an efficient component in facilitating ion diffusion and contributing to uniform Li deposition.[184] Through simple pre-treatment in aqueous $LiPF_6$ solution, LiF-protected artificial SEI coating is constructed onto Cu current collector.[52] This LiF-rich SEI guides the deposited Li into an ordered and aligned columnar structure, along with high CE and long lifespan in both ester and ether electrolytes. In general, the thickness of designed artificial SEI coatings exceeds 10 μm, which can induce large ion transfer resistance. With the development of atomic layer deposition, thin layer of Al_2O_3 layer (2–3 nm) can be controlled and deposited onto Li metal.[216] Al_2O_3 has two advantages as an artificial SEI layer: (1) Al_2O_3 can react with Li to form a thermodynamically stable Li^+ conducting layer $LiAlO_x$; (2) the processed Al_2O_3 can be performed at low temperature to avoid the melting of Li. This ultrathin Al_2O_3 layer protects the Li anode and achieves stable cycling for 1259 cycles before failing. The application of chemical vapor deposition provides another effective method to address the interfacial issues of Li anode. Two-dimensional (2D) boron nitride (BN) with strong in-plane Young's modulus (1 TPa) is synthesized by chemical vapor deposition to serve as artificial SEI coating.[130] To increase the Li diffusion rate, nanosized LiF is an ideal candidate to be deposited onto the prepared BN. Rather than dendritic morphology on pristine Cu, dense Li deposition with film pattern is achieved. This hybrid LiF/BN film exhibits stable cycling more than 300 cycles with high CE of 95% in additive-free ester electrolyte. Despite the strong mechanical strength of inorganic materials, the brittleness requests complex material processing to avoid fracture. Therefore, the rational combination of inorganic/polymer and inorganic/organic materials becomes an important choice to construct flexible and rigid artificial SEI coating. For example, LiCl containing inorganic–organic layer on Li surface not only enables high Li^+ conductivity, but also regulates the uniform Li deposition and inhibits Li dendrite growth.[217] 2.5 μm-thick lithiated Nafion/LiCl hybrid artificial SEI regulates fast ionic transport pathway and strong mechanical modulus for suppression of interface fluctuation and dendrite growth.[218] In addition, SiO_2 decorated polyacrylonitrile,[219] g-C_3N_4 derived organic/inorganic composite,[220] LiF incorporated with poly(vinylidene-*co*-hexafluoropropylene)[221] and Cu_3N joined styrene butadiene rubber[222] are also investigated for protecting Li anode.

To conclude, the electrolyte-derived and artificial SEI are two major approaches to build protective interface on Li anode. However, both methods have merits and disadvantages as discussed above. For the future, functionalizing protective layer with high Li^+ conductivity, strong mechanical strength, high flexibility, suitable thickness and simple preparation are basic requirements needed to be explored.

4.2 Volume expansion

In view of the hostless nature of Li deposition, a large volume expansion occurs during the Li plating process. Such large volume changes fracture the fragile SEI and expose fresh Li to electrolyte. Similar to graphite and Si anodes with host, it is necessary to design a proper 3D matrix to host Li and control the volume change (Fig. 23). For the common Li-based cell, 2D planar Cu foil is used as the current collector. Due to the rough surface with microstructure bumps, uneven Li^+ charge distribution leads to fast Li deposition on the tips of the Cu foil. The wild Li growth with uncontrollable volume expansion exposes fresh Li to the electrolyte, causing the formation of more dendritic structures and low CE. Regulation of the Li deposition morphology from 2D to 3D has two merits: (1) the stable 3D host with porous structure can accommodate the uncontrollable volume expansion; (2) the 3D interconnected architecture provides large specific surface areas for reducing the local current density and suppressing dendrite formation. In this section, the progress of metal-based and carbon-based hosts is summarized.

4.2.1 Metal-based host. Compared with the 2D planar Cu current collector, the conductive 3D Cu framework with large pore volume, pore size and surface area, provides more Li^+ electrodeposition sites and results in faster charge transfer kinetics. During Li deposition, Li is inclined to firstly form small Li dendrites at the nucleation site of 2D planar current collector and subsequently accelerates the growth rate at the sharp tips within the electric field (Fig. 24a).[223] After depositing 2 mA h cm^{-2} of Li, a large area of mossy Li is observed on the planar Cu foil with vertical direction. Such dendrites can pierce through the separators and give rise to safety concerns. For the 3D Cu foil, numerous protuberant tips serve as the nucleation

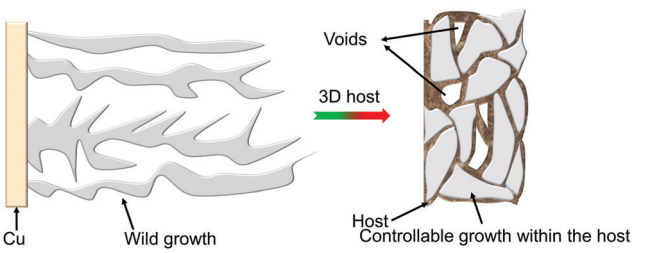

Fig. 23 Schematics of the Li growth on bare Cu (left) and 3D host (right).

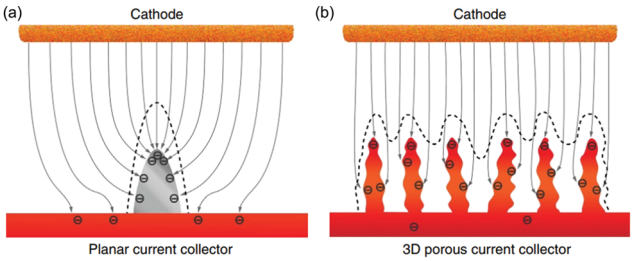

Fig. 24 (a) Schematic of Li deposition on bare 2D planar Cu current collector. (b) Schematic of Li deposition on 3D porous Cu current collector. Reproduced with permission from ref. 223. Copyright 2015, Nature Publishing Group.

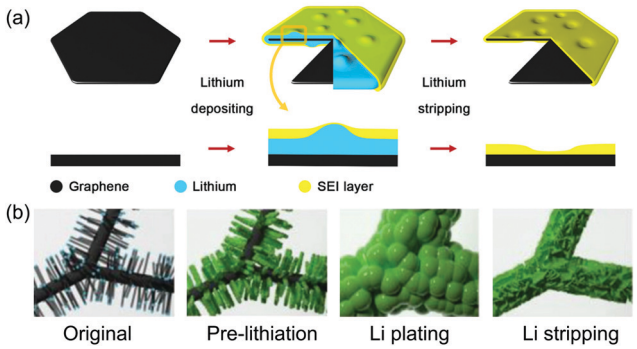

Fig. 25 (a) Schematic of Li depositing/stripping process on the graphene flake and its corresponding sectional view. Reproduced with permission from ref. 231. Copyright 2016, Wiley-VCH. (b) Schematic of the morphological changes on the carbon nanotubes-melamine derived carbon in Li plating/stripping. Reproduced with permission from ref. 233. Copyright 2019, Wiley-VCH.

sites and induce uniform electric field along the Cu skeleton (Fig. 24b). A relatively flat Li surface is obtained and no raised dendrites appear. As a result, the Li anode holds high areal capacity and achieves a high CE of 98.5%. In addition to the submicron-structured 3D Cu foil, other advanced porous architectures, such as the 3D Cu foam,[224] 3D Ni foam,[225] 3D Cu mesh,[226] 3D Cu nanoporous/macroporous structure,[227] 3D Cu vertical aligned microchannel,[228] N-doped-C/ZnO modified 3D Cu foam[229] and 3D Cu/Zn current collector[230] are also promising candidates for suppressing the uncontrollable dendrite growth.

4.2.2 Carbon-based host. Despite homogeneous nucleation and growth are achieved in 3D metal-based structure, the utilization of metal current collectors can decrease the energy density and increase the packing cost. Carbon-based materials, with low density, high electronic conductivity, high mechanical strength, low cost and stable electrochemistry, are considered the ideal host candidates for constructing advanced Li composite. For most carbon materials, the weak binding energy with Li and low specific surface area usually lead to poor lithiophilicity and inhomogeneous Li deposition. Based on Sand's equation, small effective electrode current density (J) can lengthen the Sand's time and suppress the dendrite formation. To ensure a carbon host with high specific surface area, the unstacked graphene with high specific surface areas (1666 $m^2 g^{-1}$), pore volume (1.65 $cm^3 g^{-1}$), superior electronic conductivity (435 S cm^{-1}) and good lithiophilicity is synthesized.[231] Such high specific area induces ultralow local current density and forms a sandwich-like core–shell structure. On one hand, this sandwich-like structure inhibits the dendrite formation with an ultralow local current density (Fig. 25a). On the other hand, high CE is achieved by blocking the electrolyte out of the structure. After depositing 2 mA h cm^{-2} into the graphene-based host, a small Li bump with size of 50–100 nm forms without dendrite. Due to the large surface area of 1666 $m^2 g^{-1}$, the local current density of Li depositing sites on graphene-based host is about 4×10^{-5} mA cm^{-2}, which is no more than ten thousandth of routine Cu-based anode. After Li stripping from the graphene-based host, the core–shell structure with SEI covering graphene flakes is observed with thickness about 30 nm. When operated at high deposition capacity of 5 mA h cm^{-2} and high current density of 2 mA cm^{-2}, high CE of 93% is achieved, along with stable Li plating morphology over 800 cycles. To further regulate the Li deposition direction, carbonized wood is taken as the carbon-based host for storing Li.[232] This conductive framework with well-aligned channels guides uniform Li deposition. The high porosity effectively confines the volume expansion and achieves high anode loading. Despite the success mentioned above, the loading capacity is limited and usually less than 5 mA h cm^{-2}. To improve the loading capacity over 10 mA h cm^{-2} or more, carbon nanotube-decorated carbon sponge by heating melamine sponge loaded with nickel particles is designed.[233] The melamine with N-containing and O-containing functional groups provides more nucleation sites for Li deposition (Fig. 25b). The carbon nanotubes grown on the graphitic scaffold greatly improve the mechanical strength. Impressively, the anode is cyclable at 15 mA cm^{-2} with a loading capacity of 15 mA h cm^{-2}.

Despite the 3D host relieves the volume expansion, the vertical non-uniform Li^+ concentration still affects the Li deposition. High Li^+ flux at the host surface but low diffusion rate in the bulk leads to overlying deposit of Li out of the host. To address this issue, Li nucleation seeds have proved to be an effective strategy for guiding Li deposition. 11 elemental substrates are studied for the difference of nucleation barriers, including Au, Ag, Zn, Mg, Al, Pt, Si, Sn, C, Cu and Ni.[234] Compared with bare Cu, the Li nucleation overpotential on lithiated Au is nearly zero (Fig. 26a). Thereafter, a nanocapsule structure composed of hollow carbon spheres with Au nanoparticle seeded inside is designed. Rather than dendritic morphology outside the carbon shells, Li predominantly nucleates and grows inside the hollow carbon spheres due to the decorated Au nanoparticles (Fig. 26b). Such controllable Li deposition eliminates the dendrite formation and achieves high CE of 98% even in corrosive ester electrolyte. Other nucleation seeds, such as CoN_x sites,[235] ZnO seeds[236] and N-containing functional groups,[175] have also proved to be effective in guiding uniform Li deposition. In general, Li is commonly pre-deposited into the 3D host through the electrodeposition method, and disassembled from the half cells as the anode to pair with cathode. In view of the complexity of pre-depositing technique for scalable manufacturing and inhomogeneity

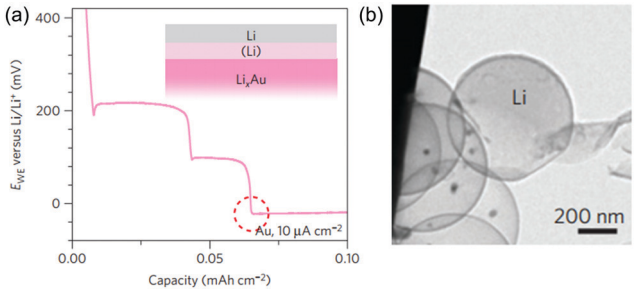

Fig. 26 (a) Voltage profiles of galvanostatic Li deposition on Au substrate at 10 μA cm^{-2}. (b) TEM snapshots of the Li deposition process inside carbon shells with Au nanoparticles. Reproduced with permission from ref. 234. Copyright 2016, Nature Publishing Group.

of deposition, this strategy faces great inconvenience in practical application. On account of this, thermal infusion strategy is proposed to infuse molten Li to carbon-based host. Compared with the unstacked graphene, rGO has better lithiophilicity for guiding uniform Li nucleation and low plating overpotential. To produce large interspace for molten Li, the graphene oxide (GO) is first put into contact with the molten Li and produces a porous structure.[179] This porous structure is ascribed to the removal of superheated residual water and surface functional groups of GO. This spark reaction not only produces a large number of nanogaps for Li deposition, but selectively removes the reactive surface functional groups. As the molten Li contacts the rGO, less than 1 min is achieved for silvery Li to spread across the whole rGO film. Such fast Li intake is ascribed to the synergetic effect of the lithiophilic nature by the residual functional groups and the capillary force by the nanogaps. Based on the first-principles calculations, carbonyl (3.080 eV) and alkoxy (2.974 eV) groups exhibit stronger binding energy to Li than the bare graphene (1.983 eV), which increases the Li intake rate. In addition, the nanogap on the top layer of rGO serves as an artificial interface for preventing Li from direct contact with electrolyte. Benefitting from these merits, stable cycling performance with low overpotential of 40 mV is achieved at 3 mA cm^{-2}.

5. Conclusions and outlook

Li metal has been dubbed the Holy Grail of anode materials for high-energy-density energy storage systems due to its lowest electrochemical potential and highest theoretical specific capacity. Nevertheless, uncontrolled dendrite formation, poor reversible Li CE and large volume expansion have long hindered its practical application. The current understanding of Li growth instability is largely based on the simple case of aqueous Cu^{2+} electrodeposition, in which dendritic fractal patterns are produced and their structure is determined by the long-range diffusion-limited growth. When the depletion rate of metal cations becomes greater than the diffusion limitation during electroreduction, the cation concentration at the electrode surface drops to zero at the Sand's time, leading to dendritic formation. However, the Li dendrite appears far ahead of Sand's time. Considering the high surface area of the dendritic Li, the true areal current density is even lower than the applied one, and may never lead to dendritic Li deposition. This puzzled phenomenon indicates that undiscovered cause is neglected except the diffusion-limited influencing factor. Compared with Cu metal electrode without SEI film during deposition, it can be inferred that the interfacial chemistry of Li is key for the dendrite formation. After SEI formation, the Li deposition process is triggered, accompanying with a limited short-range solid-state transport through the SEI film, rather than long-range liquid-state diffusion. Notably, the volume expansion always accompanies the increased deposition time or capacity. Owing to the fragile and brittle features, the SEI film is not chemically stable or mechanically strong enough to prevent the Li dendrite growth. During the dendrite growth as the increased deposition capacity, the large volume expansion easily fractures the SEI and exposes fresh Li to the electrolyte. This process happens over and over again during the dendrite growth, and induces non-uniform SEI film for dendrite formation in advance of Sand's time. Furthermore, the slow Li atom migration in bulk base also affects the dendrite formation. Therefore, the sluggish Li deposition kinetics are generally considered the reason for Li dendrite formation, which has been given much attention. During the dendrite formation, low CE and large volume expansion are also detrimental to the Li anode. In this review, taking the dynamic dendrite evolution (from dendrite formation to growth) as the main line, the Li deposition chemistry are summarized. For the dendrite formation, the emphasis is placed on the Li^+ solvation sheath, and first considers the dynamic evolution of Li^+ solvation sheath (from solvated Li^+ to Li atom) as the main line to comprehensively summarize the current understanding and progress during the Li deposition process. The dielectric constant, donor number, viscosity and salt concentration play key roles in determining whether there are enough fast-moving cations in the electrolyte. Non-polar solvents that dilute the interaction between Li^+ and the solvated solvent, and these together with anions in the primary solvation sheath are believed to reduce the Li^+ desolvation energy at SEI/electrolyte interface. The formation mechanism and models of the SEI film, together with its specific adsorption, solvated coordination structure, and strategies to modulate the ion diffusion through it by tuning its structural uniformity, surface energy and diffusion barrier produced by its chemical components, and its growth thickness have been discussed. The effect of host materials with different diffusion coefficients on the rate of Li atom migration in Li bulk base is also summarized. For the dendrite growth, the attention is focused on reducing the side reactions by manipulation of the structural stability of electrolyte-derived and artificial SEI, and minimizing the volume expansion by 3D host with controllable volume.

In spite of the advances mentioned above, there are still underlying mysteries in the Li deposition process. In Fig. 27, the six sectors correspond to the four rate-determining steps (Li^+ solvation sheath moving from the electrolyte to the SEI/electrolyte interface; Li^+ shedding their solvation sheath at SEI/electrolyte interface; Li^+ diffusing through the SEI film; Li atoms migrating in bulk base) in the dendrite formation

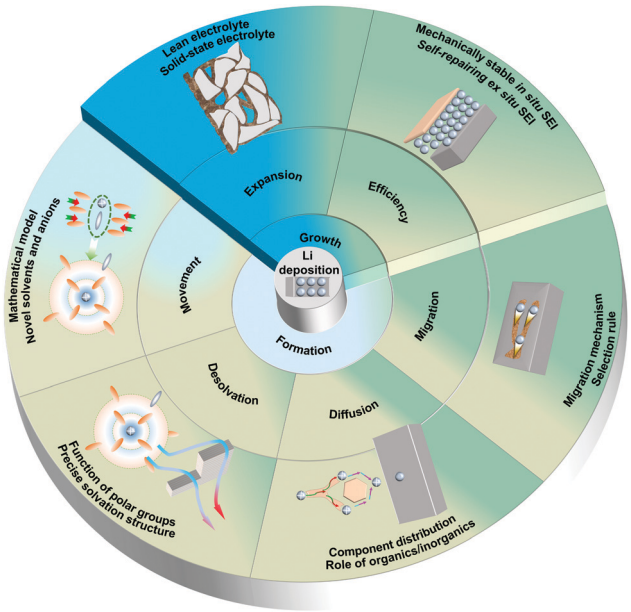

Fig. 27 Possible research directions for regulating the deposition process to obtain uniform Li deposition.

process, and the CE and volume expansion in the dendrite growth process. The six steps need to make joint efforts to support uniform Li deposition in the center of sectors. Corresponding to the current issues mentioned above, the following research topics deserve particular attention:

(1) The establishment of an accurate mathematical correlation between ion conductivity, salt concentration, current density and Li dendrite growth rate, and the use of novel salts and solvents. To some extent, the proposed diffusion–reaction competition mechanism has not completely clearly described the dendrite formation. The critical reaction rate ($Li^+ + e^- = Li$), the precise Li^+ diffusion rate in the SEI layer, the Sand's time, Li nucleation radius, Li nucleation overpotential, the space charge distribution near the electrode surface, and the dendrite growth rate at different current densities are vague. More quantitative investigations are required to disclose details affecting these parameters. In addition, almost all the current electrolytes matched with Li anode are based on fluorinated solvents or highly concentrated fluorinated anions.[102] Although the fluorinated molecules or anions produce LiF-rich SEI film which improves the Li^+ transport behavior, fluorine atoms with high electronegativity also reduce the donor number of the solvent, which causes low salt solubility along with low ionic conductivity.[56] It is urgent to exploit new types of fluorinated solvents with moderate polar groups (C═O, C–O, S═O, C≡N, *etc.*) to improve both the ionic conductivity and the properties of the SEI. Large anions, with strong electron-withdrawing groups, such as per-fluorinated groups ($-(CF_2)_nCF_3$), sulfimide groups ($-SO_2N-$) and mesylate-based groups ($-SO_3$), will lower the dissociation constants and favor high ionic conductivity. Designing new salt anions based on these two key aspects would be interesting to investigate.

(2) Determining precise knowledge of the structure of Li^+ solvation sheath and the function of polar groups (anions and solvents). The structure of the Li^+ solvation sheath has currently been investigated by *ab initio* molecular simulation, which depends on a simple hypothesis for which there is no direct evidence. The Li^+ solvation sheath has been studied by a range of techniques, including Raman spectroscopy, FTIR and NMR. However, the effects of the number of solvated molecules or anions in the primary and secondary solvation sheaths, the bond strength between Li^+ and the solvated molecules or anions, the distances between Li^+ and different solvated molecules or anions, the interaction between Li^+ and the bonding groups of the solvents or anions, and solvent/anion ratio are still relatively unclear. In addition, the polarity and valence electron distribution of different functional groups (C═O, S═O, NO_3^-, $-NSO_2CF_3$, *etc.*) on the Li^+ desolvation activation energy need to be investigated.

(3) The detailed SEI formation process, component distribution and role of inorganics/organics in the SEI film. Based on the present understanding, the SEI components are mainly derived from the decomposed adsorbed free solvents/anions in the electrochemical double layer or the coordinated solvents/anions in the Li^+ solvation sheath. But the dynamic SEI formation process, especially the exact decomposition process, the nature of the decomposed products, and chemical distribution (organic or inorganic species), are unclear. Therefore, it is necessary to clarify the detailed evolution of the dynamic interface for controlling the component, structure, and thickness of SEI film. Furthermore, existing characterization techniques are limited to identifying the chemical components. Electron beam irradiation by X-ray photoelectron spectroscopy (XPS) or TEM may chemically reduce the unstable organic species and generate inaccurate components. It is difficult to identify the organic species from the XPS C 1s spectrum or O 1s spectrum, and hard to determine the exact chemical formula of most organic species with bonds like C–C, C–O, C═O, C–F, CF_2, CF_3 and O–C═O. Although Raman and FTIR spectroscopy do not do much damage to the SEI components, many components cannot be detected because of the poor signal-to-noise ratios caused by their relatively low concentrations in the SEI film.[134] Advanced *in situ* or *operando* characterizations with high space and time resolution, such as the emerging dynamic nuclear polarization enhanced NMR, surface-enhanced Raman spectroscopy, cryo-transmission electron microscopy, synchrotron X-ray analytical techniques, and combined SEM-XPS techniques, are greatly needed to shed fresh light on the SEI components. Because of their different ion diffusion mechanisms (organics: pore diffusion, inorganics: knock-off diffusion, grain boundary, interstitials and vacancies), the contributions from inorganics and organics to the ion transport kinetics are distinctly different. Most research has focused on increasing the inorganic content (LiF, Li_3N, Li_2S, Li_2O, *etc.*) in the SEI to improve the performance of Li anode.[53,237–239] However, the exact ratio of inorganics/organics for the best performance remains a mystery. Furthermore, ion transport contributions from the abundant organic ingredients are almost completely ignored. The clear role of the inorganic/organic ratio in the SEI is the foundation for future interfacial design.

(4) The selection rule for new materials with high Li atom migration rate and the migration mechanism. Most studies have

focused on Li-metal alloys (LiAg, LiZn, Li_3Bi)[176,177] and nanostructured high-surface-area carbon scaffolds (LiC_6, rGO),[174,179] with only a few on metallic compounds (metal oxide, metal carbides, metal sulfides), organic polymers (chain polymers, porous polymers) and inorganic nanomaterials (Li_3N, Li_2S, Li_3P). Key features need to be identified by both theoretical and experimental investigation, which should suggest how to exploit new materials with high Li atom diffusion coefficient. In addition, the diffusion coefficients on different lattice planes can be quite different. Synthesis of materials with a specific lattice plane oriented parallel to the SEI surface is beneficial for promoting the migration of Li atoms. Moreover, the migration mechanism of the Li atom in the bulk base is still unclear. Recently, cryo-electron microscopy has improved our understanding of the evolution of SEI during cycling.[240] With the continued improvement in characterization techniques, such as cryogenics combined with *in situ* four-dimensional scanning transmission electron microscopy, and cryogenic combined with *in situ* monochromated electron energy-loss spectroscopy, the underlying mechanism needs to be investigated at the nano and atomic scales.

(5) Rational design of mechanically stable *in situ* (electrolyte-derived) SEI and self-repairing *ex situ* (artificial) SEI for high CE. For an ideal protective layer, it should possess high Li^+ conductivity, low electron conductivity, proper thickness, strong mechanical strength, fast formation rate, dense physical structure, low solubility in the electrolyte, chemically and electrochemically stable towards Li anode. For the present, whether the electrolyte-derived SEI or artificial SEI is far from to satisfy these basic requirements. In general, electrolyte-derived SEI can achieve high Li^+ conductivity and low electron conductivity with a fast formation rate, but not strong enough to prevent the pull-out during the dendrite growth. Artificial SEI possesses strong mechanical strength to prevent the direct contact between Li and electrolyte; however, the thickness, ion conductivity and self-repairing ability are insufficient. For the electrolyte-derived SEI, most sacrificial agents are decomposed by the electrochemical reaction with Li at some certain potential. Designing the sacrificial agent with direct chemical reaction with Li is easily controllable to the SEI with desired component, structure and thickness. In addition, single additive has made important strides for improving the CE, but efficiency is not enough. The collaboration of multicomponent additives should be paid more attention. Nonreactive solvents may also self-assemble onto Li surface and protect the Li anode to prevent the contact between Li and reactive electrolyte. Moreover, the interactions between Li deposition morphology, growth particle size, growth particle density and the formed SEI is unclear. For the artificial SEI, the low Li^+ conductivity needs to be addressed first, which can induce some inorganic conductive species, such as Li_3N, Li_2S, *etc.* On account of the shortage of self-repairing, an artificial SEI with a self-healing structure, such as self-healing polymer layer, is beneficial for minimizing the side reactions. Furthermore, most of the artificial SEI coatings are single-layer, single-component with a single desired property, such as high modulus or ionic conductivity, a stable interface with multi-layer structures is eager. Importantly, the thickness of artificial SEI coating should be thin enough for reducing the transport resistance.

(6) Lean electrolyte in 3D host and solid-state electrolyte. Large variation as the increased deposition capacity leads to high mechanical stress on the existing SEI layers and may cause the breakdown of cells. Rather than wild volume change in 2D planar current collector, structuring the deposited Li into an inert 3D host (metal-based or carbon-based) can effectively relieve the volume expansion and achieve high areal capacity. 3D host with high surface area and electronic conductivity also renders low and uniform local current density for regulating dendrite-free morphology. However, the high specific surface area increases the contact area between Li and electrolyte. Thus, a great number of SEI layer form and cover the surface area, inducing a considerable consumption of Li and electrolyte in the initial cycles. Such low initial anode CE is very lethal for the practical application when using 3D host. To replenish the electrolyte consumption, more electrolytes will be added in the cells. When the Li–S battery is loaded with 40 μL mA h^{-1} (electrolyte to cathode capacity ratio) electrolyte, its energy density will decrease to about 150 W h kg^{-1}.[241,242] Such energy density is not competitive even with present LIBs. When the electrolyte reaches 6 μL mA h^{-1}, about 300 W h kg^{-1} can be delivered by the Li–S battery. Therefore, electrolyte usage affects the cycling efficiency and energy density of Li metal batteries. When developing strategies to improve the Li anode, the cell with cathode loading (>4 mA h cm^{-2}), applied current density (>1 mA cm^{-2}), limited Li anode (<50 μm in thickness) and lean electrolyte (<3 g mA h^{-1}) is suggested. Combining the 3D host with an artificial stable SEI layer is an effective strategy for improving the low efficiency. In addition, the host, especially the metal-based skeleton, will increase the extra weight of the battery and lower the energy density of whole battery. New forms of well-designed 3D carbon-based host with tunable structure, stable interlamellar spacing and large porosity is highly desired. Furthermore, compared with liquid electrolyte, solid-state electrolyte with high Young's modulus has been considered one of the most remarkable solutions to suppress the volume expansion against 3D host. It is acknowledged that the dendrite can be suppressed when the shear modulus of the electrolyte exceeds twice that of Li anode (about 1 GPa).[12] In addition, the solid-state electrolyte can also avoid the issues of unstable SEI in nonaqueous electrolyte and improve the utilization of Li anode.

To solve the above issues associated with the Li deposition kinetics, joint innovations are required from many disciplines to improve the electrode materials and the electrolyte chemistry and to gain in-depth insight to the process based on both theory and experiment. It is believed that with persistent cooperation and dedication, a significant breakthrough on fast Li deposition kinetics can be achieved, which may also shed light on the development of similar electrochemical reaction processes in other liquid solution systems (nonaqueous, aqueous, ionic, and the flow redox battery).

Conflicts of interest

There are no conflicts to declare.

Acknowledgements

The authors acknowledge financial support from National Natural Science Foundation of China (No. 51525206, 51927803, 51972313, 52020105010, 52072378, and 51902316), National Key R&D Program of China (2016YFA0200102 and 2016YFB0100100), the Strategic Priority Research Program of the Chinese Academy of Sciences (XDA22010602), Liaoning Revitalization Talents Program (No. XLYC1908015), Youth Innovation Promotion Association of the Chinese Academy of Sciences (No. Y201942), the Special Projects of the Central Government in Guidance of Local Science and Technology Development (No. 2020JH6/10500024), the Key Research Program of the Chinese Academy of Sciences (Grant No. KGZD-EW-T06). The Bureau of Industry and Information Technology of Shenzhen for the "2017 Graphene Manufacturing Innovation Center Project" (No. 201901171523).

Notes and references

1 J. M. Tarascon and M. Armand, *Nature*, 2001, **414**, 359–367.
2 Y.-S. Hu and Y. Lu, *ACS Energy Lett.*, 2019, **4**, 2689–2690.
3 J. B. Goodenough, *Energy Storage Mater.*, 2015, **1**, 158–161.
4 K. Chen, Z. Sun, R. Fang, F. Li and H.-M. Cheng, *Acta Phys.-Chim. Sin.*, 2018, **4**, 377–390.
5 D. L. Wood III, J. Li and C. Daniel, *J. Power Sources*, 2015, **275**, 234–242.
6 Y. Abe and S. Kumagai, *J. Energy Storage*, 2018, **19**, 96–102.
7 Y. V. Mikhaylik, I. Kovalev, R. Schock, K. Kumaresan, J. Xu and J. Affinito, *ECS Trans.*, 2010, **25**, 23.
8 H. Yang, J. Li, Z. Sun, R. Fang, D.-W. Wang, K. He, H.-M. Cheng and F. Li, *Energy Storage Mater.*, 2020, **30**, 113–129.
9 R. Xu, X.-B. Cheng, C. Yan, X.-Q. Zhang, Y. Xiao, C.-Z. Zhao, J.-Q. Huang and Q. Zhang, *Matter*, 2019, **1**, 317–344.
10 J. Lu, L. Li, J.-B. Park, Y.-K. Sun, F. Wu and K. Amine, *Chem. Rev.*, 2014, **114**, 5611–5640.
11 J. Besenhard and G. Eichinger, *J. Electroanal. Chem. Interfacial Electrochem.*, 1976, **68**, 1–18.
12 W. Xu, J. Wang, F. Ding, X. Chen, E. Nasybulin, Y. Zhang and J.-G. Zhang, *Energy Environ. Sci.*, 2014, **7**, 513–537.
13 D. J. Pereira, J. W. Weidner and T. R. Garrick, *J. Electrochem. Soc.*, 2019, **166**, A1251–A1256.
14 F. Shi, A. Pei, A. Vailionis, J. Xie, B. Liu, J. Zhao, Y. Gong and Y. Cui, *Proc. Natl. Acad. Sci. U. S. A.*, 2017, **114**, 12138–12143.
15 A. Pei, G. Zheng, F. Shi, Y. Li and Y. Cui, *Nano Lett.*, 2017, **17**, 1132–1139.
16 A. Jana and R. E. Garcia, *Nano Energy*, 2017, **41**, 552–565.
17 H. Yang, L. Yin, H. Shi, K. He, H.-M. Cheng and F. Li, *Chem. Commun.*, 2019, **55**, 13211–13214.
18 D. T. Boyle, X. Kong, A. Pei, P. E. Rudnicki, F. Shi, W. Huang, Z. Bao, J. Qin and Y. Cui, *ACS Energy Lett.*, 2020, **5**, 701–709.
19 J. Xiao, *Science*, 2019, **366**, 426–427.
20 J.-N. Chazalviel, *Phys. Rev. A: At., Mol., Opt. Phys.*, 1990, **42**, 7355–7367.
21 H. J. Sand, *Proc. R. Soc. London*, 1899, **17**, 496.
22 C. Brissot, M. Rosso and J. N. Chazalviel, *J. Power Sources*, 1999, **81–82**, 925–929.
23 I. W. Seong, C. H. Hong, B. K. Kim and W. Y. Yoon, *J. Power Sources*, 2008, **178**, 769–773.
24 R. L. Sacci, N. J. Dudney, K. L. More, L. R. Parent, I. Arslan, N. D. Browning and R. R. Unocic, *Chem. Commun.*, 2014, **50**, 2104–2107.
25 P. Bai, J. Li, F. R. Brushett and M. Z. Bazant, *Energy Environ. Sci.*, 2016, **9**, 3221–3229.
26 J. Steiger, D. Kramer and R. Mönig, *Electrochim. Acta*, 2014, **136**, 529–536.
27 Y. He, X. Ren, Y. Xu, M. H. Engelhard, X. Li, J. Xiao, J. Liu, J.-G. Zhang, W. Xu and C. Wang, *Nat. Nanotechnol.*, 2019, **14**, 1042–1047.
28 Y. Li, Y. Li, A. Pei, K. Yan, Y. Sun, C.-L. Wu, L.-M. Joubert, R. Chin, A. L. Koh, Y. Yu, J. Perrino, B. Butz, S. Chu and Y. Cui, *Science*, 2017, **358**, 506.
29 X. Wang, G. Pawar, Y. Li, X. Ren, M. Zhang, B. Lu, A. Banerjee, P. Liu, E. J. Dufek, J.-G. Zhang, J. Xiao, J. Liu, Y. S. Meng and B. Liaw, *Nat. Mater.*, 2020, **19**, 1339–1345.
30 M. Jäckle and A. Groß, *J. Chem. Phys.*, 2014, **141**, 174710.
31 E. Dologlou, *Glass Phys. Chem.*, 2010, **36**, 570–574.
32 P. Shewmon, *JOM*, 1956, **8**, 918–922.
33 E. A. Brener, *J. Cryst. Growth*, 1990, **99**, 165–170.
34 Y. Shi, J. Wan, G.-X. Liu, T.-T. Zuo, Y.-X. Song, B. Liu, Y.-G. Guo, R. Wen and L.-J. Wan, *Angew. Chem., Int. Ed.*, 2020, **59**, 18120–18125.
35 T. Nishida, K. Nishikawa, M. Rosso and Y. Fukunaka, *Electrochim. Acta*, 2013, **100**, 333–341.
36 L. Li, S. Basu, Y. P. Wang, Z. Z. Chen, P. Hundekar, B. W. Wang, J. Shi, Y. F. Shi, S. Narayanan and N. Koratkar, *Science*, 2018, **359**, 1513–1516.
37 C.-C. Su, M. He, J. Shi, R. Amine, J. Zhang and K. Amine, *Angew. Chem., Int. Ed.*, 2020, **59**, 18229–18233.
38 K. M. Diederichsen, E. J. McShane and B. D. McCloskey, *ACS Energy Lett.*, 2017, **2**, 2563–2575.
39 L. Li, S. Li and Y. Lu, *Chem. Commun.*, 2018, **54**, 6648–6661.
40 J. T. Edward, *J. Chem. Educ.*, 1970, **47**, 261.
41 K. Xu, *Chem. Rev.*, 2004, **104**, 4303–4418.
42 K. Xu, Y. Lam, S. S. Zhang, T. R. Jow and T. B. Curtis, *J. Phys. Chem. C*, 2007, **111**, 7411–7421.
43 V. Koch and J. Young, *J. Electrochem. Soc.*, 1978, **125**, 1371–1377.
44 P. Dan, E. Mengeritski, Y. Geronov, D. Aurbach and I. Weisman, *J. Power Sources*, 1995, **54**, 143–145.
45 Y. Matsuda, M. Morita, K. Yamada and K. Hirai, *J. Electrochem. Soc.*, 1985, **132**, 2538–2543.
46 M. Morita, Y. Okada and Y. Matsuda, *J. Electrochem. Soc.*, 1987, **134**, 2665.
47 J. Feng, X. Ai, Y. Cao and H. Yang, *J. Power Sources*, 2008, **177**, 194–198.
48 R. Mogi, M. Inaba, S.-K. Jeong, Y. Iriyama, T. Abe and Z. Ogumi, *J. Electrochem. Soc.*, 2002, **149**, A1578–A1583.
49 E. Markevich, G. Salitra and D. Aurbach, *ACS Energy Lett.*, 2017, **2**, 1337–1345.

50 X.-B. Cheng, R. Zhang, C.-Z. Zhao and Q. Zhang, *Chem. Rev.*, 2017, **117**, 10403–10473.
51 X. Fan, X. Ji, F. Han, J. Yue, J. Chen, L. Chen, T. Deng, J. Jiang and C. Wang, *Sci. Adv.*, 2018, **4**, eaau9245.
52 X.-Q. Zhang, X. Chen, R. Xu, X.-B. Cheng, H.-J. Peng, R. Zhang, J.-Q. Huang and Q. Zhang, *Angew. Chem., Int. Ed.*, 2017, **56**, 14207–14211.
53 S. Choudhury and L. A. Archer, *Adv. Electron. Mater.*, 2016, **2**, 1500246.
54 A. Ramasubramanian, V. Yurkiv, T. Foroozan, M. Ragone, R. Shahbazian-Yassar and F. Mashayek, *J. Phys. Chem. C*, 2019, **123**, 10237–10245.
55 Y. Ozhabes, D. Gunceler and T. Arias, 2015, arXiv preprint, arXiv:1504.05799.
56 X. Fan, L. Chen, O. Borodin, X. Ji, J. Chen, S. Hou, T. Deng, J. Zheng, C. Yang, S.-C. Liou, K. Amine, K. Xu and C. Wang, *Nat. Nanotechnol.*, 2018, **13**, 715–722.
57 S.-J. Park, K.-S. Cho and S.-H. Kim, *J. Colloid Interface Sci.*, 2004, **272**, 384–390.
58 C.-C. Su, M. He, R. Amine, T. Rojas, L. Cheng, A. T. Ngo and K. Amine, *Energy Environ. Sci.*, 2019, **12**, 1249–1254.
59 Y. Zhang, Y. Zhong, Z. Wu, B. Wang, S. Liang and H. Wang, *Angew. Chem., Int. Ed.*, 2020, **59**, 7797–7802.
60 V. Gutmann, G. Resch and W. Linert, *Coord. Chem. Rev.*, 1982, **43**, 133–164.
61 K. Ueno, J. Murai, K. Ikeda, S. Tsuzuki, M. Tsuchiya, R. Tatara, T. Mandai, Y. Umebayashi, K. Dokko and M. Watanabe, *J. Phys. Chem. C*, 2016, **120**, 15792–15802.
62 N. Nambu, R. Takahashi, M. Takehara, M. Ue and Y. Sasaki, *Electrochemistry*, 2013, **81**, 817–819.
63 S.-K. Jeong, M. Inaba, Y. Iriyama, T. Abe and Z. Ogumi, *Electrochim. Acta*, 2002, **47**, 1975–1982.
64 R. Younesi, G. M. Veith, P. Johansson, K. Edström and T. Vegge, *Energy Environ. Sci.*, 2015, **8**, 1905–1922.
65 N. von Aspern, G. V. Röschenthaler, M. Winter and I. Cekic-Laskovic, *Angew. Chem., Int. Ed.*, 2019, **58**, 15978–16000.
66 X. Wang, Z. Shang, A. Yang, Q. Zhang, F. Cheng, D. Jia and J. Chen, *Chem.*, 2019, **5**, 364–375.
67 P. G. Sears and W. C. O'Brien, *J. Chem. Eng. Data*, 1968, **13**, 112–115.
68 Y. Jie, X. Liu, Z. Lei, S. Wang, Y. Chen, F. Huang, R. Cao, G. Zhang and S. Jiao, *Angew. Chem., Int. Ed.*, 2020, **132**, 3533–3538.
69 W. Zhang, Q. Wu, J. Huang, L. Fan, Z. Shen, Y. He, Q. Feng, G. Zhu and Y. Lu, *Adv. Mater.*, 2020, **32**, 2001740.
70 P. Shi, H. Zheng, X. Liang, Y. Sun, S. Cheng, C. Chen and H. Xiang, *Chem. Commun.*, 2018, **54**, 4453–4456.
71 Y. Liu, D. Lin, Y. Li, G. Chen, A. Pei, O. Nix, Y. Li and Y. Cui, *Nat. Commun.*, 2018, **9**, 3656.
72 S. S. Zhang, *Electrochim. Acta*, 2012, **70**, 344–348.
73 X. Q. Zhang, X. Chen, X. B. Cheng, B. Q. Li, X. Shen, C. Yan, J. Q. Huang and Q. Zhang, *Angew. Chem., Int. Ed.*, 2018, **57**, 5301–5305.
74 Y. Jie, X. Liu, Z. Lei, S. Wang, Y. Chen, F. Huang, R. Cao, G. Zhang and S. Jiao, *Angew. Chem., Int. Ed.*, 2020, **59**, 3505–3510.
75 Z. L. Brown, S. Heiskanen and B. L. Lucht, *J. Electrochem. Soc.*, 2019, **166**, A2523–A2527.
76 L. Suo, W. Xue, M. Gobet, S. G. Greenbaum, C. Wang, Y. Chen, W. Yang, Y. Li and J. Li, *Proc. Natl. Acad. Sci. U. S. A.*, 2018, **115**, 1156–1161.
77 Q. Ma, Z. Fang, P. Liu, J. Ma, X. Qi, W. Feng, J. Nie, Y. S. Hu, H. Li and X. Huang, *ChemElectroChem*, 2016, **3**, 531–536.
78 L. Suo, Y.-S. Hu, H. Li, M. Armand and L. Chen, *Nat. Commun.*, 2013, **4**, 1481.
79 M. S. Park, S. B. Ma, D. J. Lee, D. Im, S.-G. Doo and O. Yamamoto, *Sci. Rep.*, 2014, **4**, 3815.
80 C. S. Rustomji, Y. Yang, T. K. Kim, J. Mac, Y. J. Kim, E. Caldwell, H. Chung and Y. S. Meng, *Science*, 2017, **356**, eaal4263.
81 Y. Yang, D. M. Davies, Y. Yin, O. Borodin, J. Z. Lee, C. Fang, M. Olguin, Y. Zhang, E. S. Sablina and X. Wang, *Joule*, 2019, **3**, 1986–2000.
82 Y. Yang, Y. Yin, D. M. Davies, M. Zhang, M. Mayer, Y. Zhang, E. S. Sablina, S. Wang, J. Z. Lee and O. A. Borodin, *Energy Environ. Sci.*, 2020, **13**, 2209–2219.
83 J. Qian, W. A. Henderson, W. Xu, P. Bhattacharya, M. Engelhard, O. Borodin and J.-G. Zhang, *Nat. Commun.*, 2015, **6**, 6362.
84 N. Shao, X.-G. Sun, S. Dai and D.-E. Jiang, *J. Phys. Chem. B*, 2011, **115**, 12120–12125.
85 H. Zheng, H. Xiang, F. Jiang, Y. Liu, Y. Sun, X. Liang, Y. Feng and Y. Yu, *Adv. Energy Mater.*, 2020, **10**, 2001440.
86 X. Ren, S. Chen, H. Lee, D. Mei, M. H. Engelhard, S. D. Burton, W. Zhao, J. Zheng, Q. Li, M. S. Ding, M. Schroeder, J. Alvarado, K. Xu, Y. S. Meng, J. Liu, J.-G. Zhang and W. Xu, *Chem.*, 2018, **4**, 1877–1892.
87 D. J. Yoo, S. Yang, K. J. Kim and J. W. Choi, *Angew. Chem., Int. Ed.*, 2020, **59**, 14869–14876.
88 K. Xu, *J. Electrochem. Soc.*, 2007, **154**, A162–A167.
89 K. Xu, A. von Cresce and U. Lee, *Langmuir*, 2010, **26**, 11538–11543.
90 X. Chen, X. Q. Zhang, H. R. Li and Q. Zhang, *Batteries Supercaps*, 2019, **2**, 128–131.
91 B. Klassen, R. Aroca, M. Nazri and G. Nazri, *J. Phys. Chem. B*, 1998, **102**, 4795–4801.
92 C. V. Amanchukwu, X. Kong, J. Qin, Y. Cui and Z. Bao, *Adv. Energy Mater.*, 2019, **9**, 1902116.
93 X. Fan, X. Ji, L. Chen, J. Chen, T. Deng, F. Han, J. Yue, N. Piao, R. Wang and X. Zhou, *Nat. Energy*, 2019, **4**, 882–890.
94 X. Bogle, R. Vazquez, S. Greenbaum, A. von Wald Cresce and K. Xu, *J. Phys. Chem. Lett.*, 2013, **4**, 1664–1668.
95 Z. Wang, F. Qi, L. Yin, Y. Shi, C. Sun, B. An, H. M. Cheng and F. Li, *Adv. Energy Mater.*, 2020, **10**, 1903843.
96 X.-Q. Zhang, X. Chen, L.-P. Hou, B.-Q. Li, X.-B. Cheng, J.-Q. Huang and Q. Zhang, *ACS Energy Lett.*, 2019, **4**, 411–416.
97 R. Amine, J. Liu, I. Acznik, T. Sheng, K. Lota, H. Sun, C. J. Sun, K. Fic, X. Zuo and Y. Ren, *Adv. Energy Mater.*, 2020, **10**, 2000901.
98 S. S. Zhang, *J. Electrochem. Soc.*, 2012, **159**, A920.
99 Y. He, W. Fan, Y. Zhang, Z. Wang, X. Li, Z. Liu and Z. Lü, *ACS Appl. Mater. Interfaces*, 2020, **12**, 22268–22277.

100 S. H. Lee, J. Y. Hwang, J. Ming, Z. Cao, H. A. Nguyen, H. G. Jung, J. Kim and Y. K. Sun, *Adv. Energy Mater.*, 2020, **10**, 2000567.
101 Y. Yamada, K. Furukawa, K. Sodeyama, K. Kikuchi, M. Yaegashi, Y. Tateyama and A. Yamada, *J. Am. Chem. Soc.*, 2014, **136**, 5039–5046.
102 X. Fan, L. Chen, X. Ji, T. Deng, S. Hou, J. Chen, J. Zheng, F. Wang, J. Jiang, K. Xu and C. Wang, *Chem.*, 2018, **4**, 174–185.
103 T. Abe, H. Fukuda, Y. Iriyama and Z. Ogumi, *J. Electrochem. Soc.*, 2004, **151**, A1120–A1123.
104 G. Zheng, S. W. Lee, Z. Liang, H.-W. Lee, K. Yan, H. Yao, H. Wang, W. Li, S. Chu and Y. Cui, *Nat. Nanotechnol.*, 2014, **9**, 618–623.
105 D. Lin, Y. Liu and Y. Cui, *Nat. Nanotechnol.*, 2017, **12**, 194.
106 J. B. Goodenough and Y. Kim, *Chem. Mater.*, 2010, **22**, 587–603.
107 C. Yan, R. Xu, Y. Xiao, J. F. Ding, L. Xu, B. Q. Li and J. Q. Huang, *Adv. Funct. Mater.*, 2020, **30**, 1909887.
108 D. Qu, *J. Power Sources*, 2002, **109**, 403–411.
109 D. Henderson and D. Boda, *Phys. Chem. Chem. Phys.*, 2009, **11**, 3822–3830.
110 C. Yan, H.-R. Li, X. Chen, X.-Q. Zhang, X.-B. Cheng, R. Xu, J.-Q. Huang and Q. Zhang, *J. Am. Chem. Soc.*, 2019, **141**, 9422–9429.
111 X. Liang, Z. Wen, Y. Liu, M. Wu, J. Jin, H. Zhang and X. Wu, *J. Power Sources*, 2011, **196**, 9839–9843.
112 Y. Gao, T. Rojas, K. Wang, S. Liu, D. Wang, T. Chen, H. Wang, A. T. Ngo and D. Wang, *Nat. Energy*, 2020, **5**, 534–542.
113 A. M. Smith, A. A. Lee and S. Perkin, *J. Phys. Chem. Lett.*, 2016, **7**, 2157–2163.
114 Y. Yuan, F. Wu, G. Chen, Y. Bai and C. Wu, *J. Energy Chem.*, 2019, **37**, 197–203.
115 C. Yan, X. B. Cheng, Y. Tian, X. Chen, X. Q. Zhang, W. J. Li, J. Q. Huang and Q. Zhang, *Adv. Mater.*, 2018, **30**, 1707629.
116 B. Liu, J.-G. Zhang and W. Xu, *Joule*, 2018, **2**, 833–845.
117 J. Holoubek, M. Yu, S. Yu, M. Li, Z. Wu, D. Xia, P. Bhaladhare, M. S. Gonzalez, T. A. Pascal and P. Liu, *ACS Energy Lett.*, 2020, **5**, 1438–1447.
118 J. Zheng, M. H. Engelhard, D. Mei, S. Jiao, B. J. Polzin, J.-G. Zhang and W. Xu, *Nat. Energy*, 2017, **2**, 17012.
119 H. Wang, M. Matsui, H. Kuwata, H. Sonoki, Y. Matsuda, X. Shang, Y. Takeda, O. Yamamoto and N. Imanishi, *Nat. Commun.*, 2017, **8**, 15106.
120 S. Shi, P. Lu, Z. Liu, Y. Qi, L. G. Hector Jr, H. Li and S. J. Harris, *J. Am. Chem. Soc.*, 2012, **134**, 15476–15487.
121 S.-P. Kim, A. C. Van Duin and V. B. Shenoy, *J. Power Sources*, 2011, **196**, 8590–8597.
122 E. Peled, *J. Electrochem. Soc.*, 1979, **126**, 2047.
123 J. Thevenin and R. Muller, *J. Electrochem. Soc.*, 1987, **134**, 273.
124 E. Peled, D. Golodnitsky and G. Ardel, *J. Electrochem. Soc.*, 1997, **144**, L208–L210.
125 M. Gauthier, T. J. Carney, A. Grimaud, L. Giordano, N. Pour, H.-H. Chang, D. P. Fenning, S. F. Lux, O. Paschos and C. Bauer, *J. Phys. Chem. Lett.*, 2015, **6**, 4653–4672.
126 X.-B. Cheng, C. Yan, H.-J. Peng, J.-Q. Huang, S.-T. Yang and Q. Zhang, *Energy Storage Mater.*, 2018, **10**, 199–205.
127 J. Christensen and J. Newman, *J. Electrochem. Soc.*, 2004, **151**, A1977–A1988.
128 Y. Zhu, X. He and Y. Mo, *Adv. Sci.*, 2017, **4**, 1600517.
129 K. Zhang, G. H. Lee, M. Park, W. Li and Y. M. Kang, *Adv. Energy Mater.*, 2016, **6**, 1600811.
130 J. Xie, L. Liao, Y. J. Gong, Y. B. Li, F. F. Shi, A. Pei, J. Sun, R. F. Zhang, B. Kong, R. Subbaraman, J. Christensen and Y. Cui, *Sci. Adv.*, 2017, **3**, eaao3170.
131 J. Zheng, M. S. Kim, Z. Tu, S. Choudhury, T. Tang and L. A. Archer, *Chem. Soc. Rev.*, 2020, **49**, 2701–2750.
132 K. Xu and A. von Wald Cresce, *J. Mater. Res.*, 2012, **27**, 2327–2341.
133 K. Xu and A. von Cresce, *J. Mater. Chem.*, 2011, **21**, 9849–9864.
134 Z. Wang, C. Sun, Y. Shi, F. Qi, Q. Wei, X. Li, Z. Sun, B. An and F. Li, *J. Power Sources*, 2019, **439**, 227073.
135 X. Q. Zhang, X. B. Cheng, X. Chen, C. Yan and Q. Zhang, *Adv. Funct. Mater.*, 2017, **27**, 1605989.
136 C.-C. Su, M. He, R. Amine, Z. Chen, R. Sahore, N. D. Rago and K. Amine, *Energy Storage Mater.*, 2019, **17**, 284–292.
137 M. Wang, L. Huai, G. Hu, S. Yang, F. Ren, S. Wang, Z. Zhang, Z. Chen, Z. Peng and C. Shen, *J. Phys. Chem. C*, 2018, **122**, 9825–9834.
138 W. Zhao, L. Zou, J. Zheng, H. Jia, J. Song, M. H. Engelhard, C. Wang, W. Xu, Y. Yang and J. G. Zhang, *ChemSusChem*, 2018, **11**, 2211–2220.
139 H. Xiang, P. Shi, P. Bhattacharya, X. Chen, D. Mei, M. E. Bowden, J. Zheng, J.-G. Zhang and W. Xu, *J. Power Sources*, 2016, **318**, 170–177.
140 T. Schedlbauer, U. Rodehorst, C. Schreiner, H. Gores and M. Winter, *Electrochim. Acta*, 2013, **107**, 26–32.
141 T. Schedlbauer, S. Krüger, R. Schmitz, R. Schmitz, C. Schreiner, H. Gores, S. Passerini and M. Winter, *Electrochim. Acta*, 2013, **92**, 102–107.
142 Y. Xiao, B. Han, Y. Zeng, S.-S. Chi, X. Zeng, Z. Zheng, K. Xu and Y. Deng, *Adv. Energy Mater.*, 2020, **10**, 1903937.
143 X.-B. Cheng, C. Yan, X. Chen, C. Guan, J.-Q. Huang, H.-J. Peng, R. Zhang, S.-T. Yang and Q. Zhang, *Chem.*, 2017, **2**, 258–270.
144 X. R. Chen, Y. X. Yao, C. Yan, R. Zhang, X. B. Cheng and Q. Zhang, *Angew. Chem., Int. Ed.*, 2020, **59**, 7743.
145 D. Wang, W. Zhang, W. Zheng, X. Cui, T. Rojo and Q. Zhang, *Adv. Sci.*, 2017, **4**, 1600168.
146 S. Liu, X. Ji, J. Yue, S. Hou, P. Wang, C. Cui, J. Chen, B. Shao, J. Li, F. Han, J. Tu and C. Wang, *J. Am. Chem. Soc.*, 2020, **142**, 2438–2447.
147 X.-B. Cheng, M.-Q. Zhao, C. Chen, A. Pentecost, K. Maleski, T. Mathis, X.-Q. Zhang, Q. Zhang, J. Jiang and Y. Gogotsi, *Nat. Commun.*, 2017, **8**, 336.
148 J. Lang, Y. Long, J. Qu, X. Luo, H. Wei, K. Huang, H. Zhang, L. Qi, Q. Zhang and Z. Li, *Energy Storage Mater.*, 2019, **16**, 85–90.

149 G. Hou, C. Ci, D. Salpekar, Q. Ai, Q. Chen, H. Guo, L. Chen, X. Zhang, J. Cheng and K. Kato, *J. Power Sources*, 2020, **448**, 227547.
150 Y.-X. Lin, Z. Liu, K. Leung, L.-Q. Chen, P. Lu and Y. Qi, *J. Power Sources*, 2016, **309**, 221–230.
151 T. Li, X.-Q. Zhang, P. Shi and Q. Zhang, *Joule*, 2019, **3**, 2647–2661.
152 M. He, R. Guo, G. M. Hobold, H. Gao and B. M. Gallant, *Proc. Natl. Acad. Sci. U. S. A.*, 2020, **117**, 73–79.
153 Z. Yu, H. Wang, X. Kong, W. Huang, Y. Tsao, D. G. Mackanic, K. Wang, X. Wang, W. Huang, S. Choudhury, Y. Zheng, C. V. Amanchukwu, S. T. Hung, Y. Ma, E. G. Lomeli, J. Qin, Y. Cui and Z. Bao, *Nat. Energy*, 2020, **5**, 526–533.
154 Q. Zhao, S. Stalin, C.-Z. Zhao and L. A. Archer, *Nat. Rev. Mater.*, 2020, **5**, 229–252.
155 Y. Wang, W. D. Richards, S. P. Ong, L. J. Miara, J. C. Kim, Y. Mo and G. Ceder, *Nat. Mater.*, 2015, **14**, 1026–1031.
156 S. Yu, R. D. Schmidt, R. Garcia-Mendez, E. Herbert, N. J. Dudney, J. B. Wolfenstine, J. Sakamoto and D. J. Siegel, *Chem. Mater.*, 2016, **28**, 197–206.
157 T. Thompson, A. Sharafi, M. D. Johannes, A. Huq, J. L. Allen, J. Wolfenstine and J. Sakamoto, *Adv. Energy Mater.*, 2015, **5**, 1500096.
158 F. Han, A. S. Westover, J. Yue, X. Fan, F. Wang, M. Chi, D. N. Leonard, N. J. Dudney, H. Wang and C. Wang, *Nat. Energy*, 2019, **4**, 187–196.
159 W. Luo, Y. Gong, Y. Zhu, K. K. Fu, J. Dai, S. D. Lacey, C. Wang, B. Liu, X. Han, Y. Mo, E. D. Wachsman and L. Hu, *J. Am. Chem. Soc.*, 2016, **138**, 12258–12262.
160 N. Kamaya, K. Homma, Y. Yamakawa, M. Hirayama, R. Kanno, M. Yonemura, T. Kamiyama, Y. Kato, S. Hama, K. Kawamoto and A. Mitsui, *Nat. Mater.*, 2011, **10**, 682–686.
161 Z. Wang, M. Wu, G. Liu, X. Lei, B. Xu and C. Ouyang, *Int. J. Electrochem. Sci.*, 2014, **9**, 562–568.
162 Y. Gao, D. Wang, Y. C. Li, Z. Yu, T. E. Mallouk and D. Wang, *Angew. Chem., Int. Ed.*, 2018, **57**, 13608–13612.
163 X. Zhang, Y. Yang and Z. Zhou, *Chem. Soc. Rev.*, 2020, **49**, 3040–3071.
164 W. A. Henderson and S. Passerini, *Electrochem. Commun.*, 2003, **5**, 575–578.
165 S. Xue, Y. Liu, Y. Li, D. Teeters, D. W. Crunkleton and S. Wang, *Electrochim. Acta*, 2017, **235**, 122–128.
166 Z. Gadjourova, Y. G. Andreev, D. P. Tunstall and P. G. Bruce, *Nature*, 2001, **412**, 520–523.
167 C. Brissot, M. Rosso, J. N. Chazalviel, P. Baudry and S. Lascaud, *Electrochim. Acta*, 1998, **43**, 1569–1574.
168 C.-Z. Zhao, X.-Q. Zhang, X.-B. Cheng, R. Zhang, R. Xu, P.-Y. Chen, H.-J. Peng, J.-Q. Huang and Q. Zhang, *Proc. Natl. Acad. Sci. U. S. A.*, 2017, **114**, 11069.
169 F. Y. Fan, M. S. Pan, K. C. Lau, R. S. Assary, W. H. Woodford, L. A. Curtiss, W. C. Carter and Y.-M. Chiang, *J. Electrochem. Soc.*, 2016, **163**, A3111–A3116.
170 C. Sun, Z. Wang, L. Yin, S. Xu, Z. A. Ghazi, Y. Shi, B. An, Z. Sun, H.-M. Cheng and F. Li, *Nano Energy*, 2020, **75**, 104976.
171 T. Liu, Y. Shao, G. Li, M. Gu, J. Hu, S. Xu, Z. Nie, X. Chen, C. Wang and J. Liu, *J. Mater. Chem. A*, 2014, **2**, 3430–3438.
172 K. Nishikawa, T. Mori, T. Nishida, Y. Fukunaka and M. Rosso, *J. Electroanal. Chem.*, 2011, **661**, 84–89.
173 C. Ling, D. Banerjee and M. Matsui, *Electrochim. Acta*, 2012, **76**, 270–274.
174 K. Toyoura, Y. Koyama, A. Kuwabara and I. Tanaka, *J. Phys. Chem. C*, 2010, **114**, 2375–2379.
175 R. Zhang, X. R. Chen, X. Chen, X. B. Cheng, X. Q. Zhang, C. Yan and Q. Zhang, *Angew. Chem., Int. Ed.*, 2017, **56**, 7764–7768.
176 S. Jin, Y. Ye, Y. Niu, Y. Xu, H. Jin, J. Wang, Z. Sun, A. Cao, X. Wu and Y. Luo, *J. Am. Chem. Soc.*, 2020, **142**, 8818–8826.
177 X. Liang, Q. Pang, I. R. Kochetkov, M. S. Sempere, H. Huang, X. Sun and L. F. Nazar, *Nat. Energy*, 2017, **2**, 17119.
178 P. Shi, T. Li, R. Zhang, X. Shen, X. B. Cheng, R. Xu, J. Q. Huang, X. R. Chen, H. Liu and Q. Zhang, *Adv. Mater.*, 2019, **31**, 1807131.
179 D. Lin, Y. Liu, Z. Liang, H.-W. Lee, J. Sun, H. Wang, K. Yan, J. Xie and Y. Cui, *Nat. Nanotechnol.*, 2016, **11**, 626–632.
180 M. Kühne, F. Paolucci, J. Popovic, P. M. Ostrovsky, J. Maier and J. H. Smet, *Nat. Nanotechnol.*, 2017, **12**, 895–900.
181 Z. Sun, S. Jin, H. Jin, Z. Du, Y. Zhu, A. Cao, H. Ji and L. J. Wan, *Adv. Mater.*, 2018, **30**, 1800884.
182 H. Ota, K. Shima, M. Ue and J. I. Yamaki, *Electrochim. Acta*, 2004, **49**, 565–572.
183 F. Ding, W. Xu, X. Chen, J. Zhang, M. H. Engelhard, Y. Zhang, B. R. Johnson, J. V. Crum, T. A. Blake and X. Liu, *J. Electrochem. Soc.*, 2013, **160**, A1894–A1901.
184 Y. Lu, Z. Tu and L. A. Archer, *Nat. Mater.*, 2014, **13**, 961–969.
185 D. Lin, Y. Liu, W. Chen, G. Zhou, K. Liu, B. Dunn and Y. Cui, *Nano Lett.*, 2017, **17**, 3731–3737.
186 Q. Zhang, J. Pan, P. Lu, Z. Liu, M. W. Verbrugge, B. W. Sheldon, Y. T. Cheng, Y. Qi and X. Xiao, *Nano Lett.*, 2016, **16**, 2011–2016.
187 J. Pan, Q. Zhang, X. Xiao, Y.-T. Cheng and Y. Qi, *ACS Appl. Mater. Interfaces*, 2016, **8**, 5687–5693.
188 Y. Gofer, M. Ben-Zion and D. Aurbach, *J. Power Sources*, 1992, **39**, 163–178.
189 V. R. Koch and J. H. Young, *Science*, 1979, **204**, 499–501.
190 Q. Liu, A. Cresce, M. Schroeder, K. Xu, D. Mu, B. Wu, L. Shi and F. Wu, *Energy Storage Mater.*, 2019, **17**, 366–373.
191 R. Miao, J. Yang, Z. Xu, J. Wang, Y. Nuli and L. Sun, *Sci. Rep.*, 2016, **6**, 21771.
192 D. W. Kim, S. M. Ahn, J. Kang, J. Suk, H. K. Kim and Y. Kang, *J. Mater. Chem. A*, 2016, **4**, 6332–6341.
193 Y. Yu, G. Huang, J.-Y. Du, J.-Z. Wang, Y. Wang, Z.-J. Wu and X.-B. Zhang, *Energy Environ. Sci.*, 2020, **13**, 3075–3081.
194 Q. Wang, Z. Yao, C. Zhao, T. Verhallen, D. P. Tabor, M. Liu, F. Ooms, F. Kang, A. Aspuru-Guzik, Y.-S. Hu, M. Wagemaker and B. Li, *Nat. Commun.*, 2020, **11**, 4188.
195 Z. Zeng, V. Murugesan, K. S. Han, X. Jiang, Y. Cao, L. Xiao, X. Ai, H. Yang, J.-G. Zhang, M. L. Sushko and J. Liu, *Nat. Energy*, 2018, **3**, 674–681.
196 S. Chen, J. Zheng, L. Yu, X. Ren, M. H. Engelhard, C. Niu, H. Lee, W. Xu, J. Xiao, J. Liu and J.-G. Zhang, *Joule*, 2018, **2**, 1548–1558.
197 S.-J. Tan, J. Yue, X.-C. Hu, Z.-Z. Shen, W.-P. Wang, J.-Y. Li, T.-T. Zuo, H. Duan, Y. Xiao, Y.-X. Yin, R. Wen and Y.-G. Guo, *Angew. Chem., Int. Ed.*, 2019, **58**, 7802–7807.

198 J. Fu, X. Ji, J. Chen, L. Chen, X. Fan, D. Mu and C. Wang, *Angew. Chem., Int. Ed.*, 2020, **59**, 22194–22201.
199 Z. Peng, X. Cao, P. Gao, H. Jia, X. Ren, S. Roy, Z. Li, Y. Zhu, W. Xie, D. Liu, Q. Li, D. Wang, W. Xu and J.-G. Zhang, *Adv. Funct. Mater.*, 2020, **30**, 2001285.
200 Y. Lu, S. K. Das, S. S. Moganty and L. A. Archer, *Adv. Mater.*, 2012, **24**, 4430–4435.
201 R. Miao, J. Yang, X. Feng, H. Jia, J. Wang and Y. Nuli, *J. Power Sources*, 2014, **271**, 291–297.
202 S. Liu, Q. Zhang, X. Wang, M. Xu, W. Li and B. L. Lucht, *ACS Appl. Mater. Interfaces*, 2020, **12**, 33719–33728.
203 S. Chen, J. Zheng, D. Mei, K. S. Han, M. H. Engelhard, W. Zhao, W. Xu, J. Liu and J.-G. Zhang, *Adv. Mater.*, 2018, **30**, 1706102.
204 H. Ota, Y. Sakata, Y. Otake, K. Shima, M. Ue and J. I. Yamaki, *J. Electrochem. Soc.*, 2004, **151**, A1778.
205 Y. Ma, Z. Zhou, C. Li, L. Wang, Y. Wang, X. Cheng, P. Zuo, C. Du, H. Huo, Y. Gao and G. Yin, *Energy Storage Mater.*, 2018, **11**, 197–204.
206 Z. Xie, Z. Wu, X. An, X. Yue, A. Yoshida, X. Du, X. Hao, A. Abudula and G. Guan, *Chem. Eng. J.*, 2020, **393**, 124789.
207 C. Yan, Y.-X. Yao, X. Chen, X.-B. Cheng, X.-Q. Zhang, J.-Q. Huang and Q. Zhang, *Angew. Chem., Int. Ed.*, 2018, **57**, 14055–14059.
208 Q. Zhang, K. Wang, X. Wang, Y. Zhong, M. Liu, X. Liu, K. Xu, W. Fan, L. Yu and W. Li, *ACS Appl. Mater. Interfaces*, 2019, **11**, 20854–20863.
209 L. Yu, S. Chen, H. Lee, L. Zhang, M. H. Engelhard, Q. Li, S. Jiao, J. Liu, W. Xu and J.-G. Zhang, *ACS Energy Lett.*, 2018, **3**, 2059–2067.
210 Z. T. Wondimkun, T. T. Beyene, M. A. Weret, N. A. Sahalie, C.-J. Huang, B. Thirumalraj, B. A. Jote, D. Wang, W.-N. Su, C.-H. Wang, G. Brunklaus, M. Winter and B.-J. Hwang, *J. Power Sources*, 2020, **450**, 227589.
211 B. Zhu, Y. Jin, X. Hu, Q. Zheng, S. Zhang, Q. Wang and J. Zhu, *Adv. Mater.*, 2017, **29**, 1603755.
212 Z. Hu, S. Zhang, S. Dong, W. Li, H. Li, G. Cui and L. Chen, *Chem. Mater.*, 2017, **29**, 4682–4689.
213 N.-W. Li, Y. Shi, Y.-X. Yin, X.-X. Zeng, J.-Y. Li, C.-J. Li, L.-J. Wan, R. Wen and Y.-G. Guo, *Angew. Chem., Int. Ed.*, 2018, **57**, 1505–1509.
214 G. Wang, C. Chen, Y. Chen, X. Kang, C. Yang, F. Wang, Y. Liu and X. Xiong, *Angew. Chem., Int. Ed.*, 2020, **59**, 2055–2060.
215 N.-W. Li, Y.-X. Yin, C.-P. Yang and Y.-G. Guo, *Adv. Mater.*, 2016, **28**, 1853–1858.
216 E. Kazyak, K. N. Wood and N. P. Dasgupta, *Chem. Mater.*, 2015, **27**, 6457–6462.
217 J. Yang, C. Hu, Y. Jia, Y. Pang, L. Wang, W. Liu and X. Sun, *ACS Appl. Mater. Interfaces*, 2019, **11**, 8717–8724.
218 S. Li, L. Fan and Y. Lu, *Energy Storage Mater.*, 2019, **18**, 205–212.
219 J. Shi, M. Ma, R. Wang, J. Bao and Z. Tao, *ACS Appl. Energy Mater.*, 2020, **3**, 7257–7264.
220 S. Ye, L. Wang, F. Liu, P. Shi, H. Wang, X. Wu and Y. Yu, *Adv. Energy Mater.*, 2020, **10**, 2002647.
221 R. Xu, X.-Q. Zhang, X.-B. Cheng, H.-J. Peng, C.-Z. Zhao, C. Yan and J.-Q. Huang, *Adv. Funct. Mater.*, 2018, **28**, 1705838.
222 Y. Liu, D. Lin, P. Y. Yuen, K. Liu, J. Xie, R. H. Dauskardt and Y. Cui, *Adv. Mater.*, 2017, **29**, 1605531.
223 C.-P. Yang, Y.-X. Yin, S.-F. Zhang, N.-W. Li and Y.-G. Guo, *Nat. Commun.*, 2015, **6**, 8058.
224 X.-Y. Yue, W.-W. Wang, Q.-C. Wang, J.-K. Meng, X.-X. Wang, Y. Song, Z.-W. Fu, X.-J. Wu and Y.-N. Zhou, *Energy Storage Mater.*, 2019, **21**, 180–189.
225 S.-S. Chi, Y. Liu, W.-L. Song, L.-Z. Fan and Q. Zhang, *Adv. Funct. Mater.*, 2017, **27**, 1700348.
226 Q. Li, S. Zhu and Y. Lu, *Adv. Funct. Mater.*, 2017, **27**, 1606422.
227 H. Liu, E. Wang, Q. Zhang, Y. Ren, X. Guo, L. Wang, G. Li and H. Yu, *Energy Storage Mater.*, 2019, **17**, 253–259.
228 S.-H. Wang, Y.-X. Yin, T.-T. Zuo, W. Dong, J.-Y. Li, J.-L. Shi, C.-H. Zhang, N.-W. Li, C.-J. Li and Y.-G. Guo, *Adv. Mater.*, 2017, **29**, 1703729.
229 Y. Zhou, K. Zhao, Y. Han, Z. Sun, H. Zhang, L. Xu, Y. Ma and Y. Chen, *J. Mater. Chem. A*, 2019, **7**, 5712–5718.
230 D. Zhang, A. Dai, B. Fan, Y. Li, K. Shen, T. Xiao, G. Hou, H. Cao, X. Tao and Y. Tang, *ACS Appl. Mater. Interfaces*, 2020, **12**, 31542–31551.
231 R. Zhang, X.-B. Cheng, C.-Z. Zhao, H.-J. Peng, J.-L. Shi, J.-Q. Huang, J. Wang, F. Wei and Q. Zhang, *Adv. Mater.*, 2016, **28**, 2155–2162.
232 Y. Zhang, W. Luo, C. Wang, Y. Li, C. Chen, J. Song, J. Dai, E. M. Hitz, S. Xu, C. Yang, Y. Wang and L. Hu, *Proc. Natl. Acad. Sci. U. S. A.*, 2017, **114**, 3584.
233 J. Xie, J. Ye, F. Pan, X. Sun, K. Ni, H. Yuan, X. Wang, N. Shu, C. Chen and Y. Zhu, *Adv. Mater.*, 2019, **31**, 1805654.
234 K. Yan, Z. Lu, H.-W. Lee, F. Xiong, P.-C. Hsu, Y. Li, J. Zhao, S. Chu and Y. Cui, *Nat. Energy*, 2016, **1**, 16010.
235 H. Liu, X. Chen, X.-B. Cheng, B.-Q. Li, R. Zhang, B. Wang, X. Chen and Q. Zhang, *Small Methods*, 2019, **3**, 1800354.
236 C. Jin, O. Sheng, J. Luo, H. Yuan, C. Fang, W. Zhang, H. Huang, Y. Gan, Y. Xia, C. Liang, J. Zhang and X. Tao, *Nano Energy*, 2017, **37**, 177–186.
237 K. Park and J. B. Goodenough, *Adv. Energy Mater.*, 2017, **7**, 1700732.
238 C. Yan, X.-B. Cheng, C.-Z. Zhao, J.-Q. Huang, S.-T. Yang and Q. Zhang, *J. Power Sources*, 2016, **327**, 212–220.
239 P. Zou, S.-W. Chiang, J. Li, Y. Wang, X. Wang, D. Wu, A. Nairan, F. Kang and C. Yang, *Energy Storage Mater.*, 2019, **18**, 155–164.
240 W. Huang, P. M. Attia, H. Wang, S. E. Renfrew, N. Jin, S. Das, Z. Zhang, D. T. Boyle, Y. Li and M. Z. Bazant, *Nano Lett.*, 2019, **19**, 5140–5148.
241 D. Eroglu, K. R. Zavadil and K. G. Gallagher, *J. Electrochem. Soc.*, 2015, **162**, A982–A990.
242 N. B. Emerce and D. Eroglu, *J. Electrochem. Soc.*, 2019, **166**, A1490–A1500.
243 H.-P. Wang, J. He, J.-D. Liu, S.-H. Qi, M.-G. Wu, J. Wen, Y.-N. Chen, Y.-Z. Feng and J.-M. Ma, *Adv. Funct. Mater.*, 2021, **31**, 2002578.

